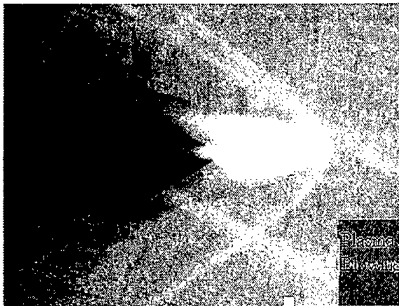


REPORT DOCUMENTATION PAGE			Form Approved OMB No. 0704-0188	
Public reporting burden for this collection of information is estimated to average 1 hour per response, including the time for reviewing instructions, searching existing data sources, gathering and maintaining the data needed, and completing and reviewing the collection of information. Send comments regarding this burden estimate or any other aspect of this collection of information, including suggestions for reducing this burden to Washington Headquarters Services, Directorate for Information Operations and Reports, 1215 Jefferson Davis Highway, Suite 1204, Arlington, VA 22202-4302, and to the Office of Management and Budget, Paperwork Reduction Project (0704-0188), Washington, DC 20503.				
1. AGENCY USE ONLY (Leave blank)	2. REPORT DATE September-2000	3. REPORT TYPE AND DATES COVERED Final Report		
4. TITLE AND SUBTITLE Plasma Influence on Characteristics of Aerodynamic Friction and Separation Lines Location		5. FUNDING NUMBERS F61775-99-WE106		
6. AUTHOR(S) Dr. Serguei Leonov				
7. PERFORMING ORGANIZATION NAME(S) AND ADDRESS(ES) Moscow Technical Company-Institute of High Temperature RAS MTC-IVTAN, Izhorskaya str., 13/19 Moscow 127412 Russia		8. PERFORMING ORGANIZATION REPORT NUMBER N/A		
9. SPONSORING/MONITORING AGENCY NAME(S) AND ADDRESS(ES) EOARD PSC 802 BOX 14 FPO 09499-0200		10. SPONSORING/MONITORING AGENCY REPORT NUMBER SPC 99-4106		
11. SUPPLEMENTARY NOTES Electronic Submission				
12a. DISTRIBUTION/AVAILABILITY STATEMENT Approved for public release; distribution is unlimited.			12b. DISTRIBUTION CODE A	
13. ABSTRACT (Maximum 200 words) This report results from a contract tasking Moscow Technical Company-Institute of High Temperature RAS as follows: The contractor will analyze experimental plasma data already obtained on different aerodynamic shapes and produce an experiment at plate model. Three types of surface discharges will be tested in this work: HF multi-streamer discharge, micro hollow cathode discharge and glide surface discharge. The project objectives are 1) analysis of data from previous experiments; 2) preparation of experiment on a surface discharge-plasma influence; 3) modification of test equipment; test-runs in short operation wind tunnel; 4) report on analysis of experimental data. The technical parameters of the experiment are the following: Mach number- 0.1-0.4, 2.0; static pressure- 50-240 Torr and 15 Torr; typical size of AD models- 40-200 mm; kind of discharges, pulsed HF discharge; Micro hollow cathode; glide surface discharge. Operation mode of discharges pulse repetition and quasi-continuous. Repetition rate up to 10kHz. Mean input power of discharges 0.1-1kW. Operation time >10ms. The following parameters will be measured: gas temperature, Tg; surface temperature, Ts, ; static and stagnation pressure on a surface, Po, Pst, plasma energetic parameters; drag and lift forces. These parameters will be measured by means of the following diagnostic methods: electrical probes, Schlieren method, pressure transducers, optical spectrometer, tenso-balances, and high speed photo camera.				
14. SUBJECT TERMS EOARD, Plasma Aerodynamic		15. NUMBER OF PAGES 104		
		16. PRICE CODE N/A		
17. SECURITY CLASSIFICATION OF REPORT UNCLASSIFIED	18. SECURITY CLASSIFICATION OF THIS PAGE UNCLASSIFIED	19. SECURITY CLASSIFICATION OF ABSTRACT UNCLASSIFIED	20. LIMITATION OF ABSTRACT UL	

20001127 054



Moscow Technical Company

MTC-IVTAN

Izhorskaya street, 13/19, of. 231

Moscow, 127412, Russia

Contract EOARD-MTC

No. F61775-99-WE106

Ref.: SPC 99-4106

Delivery 3.

**Plasma Influence on Characteristics of
Aerodynamic Friction and Separation Lines Location.**

Final Report.

Written by:

Dr. S.Leonov

Prof. A.Yuriev

Dr. A.Bocharov

Dr. V.Gromov

Mr. A.Mityagin

Mr. A.Okunev

Dr. N.Savishenko

Mr. K.Savelkin

MOSCOW- 2000

Contents

1. Introduction.
2. Background.
 - 2.1. Brief Review. Analysis of some Experimental and Theoretical Works.
 - 2.2. Navier-Stokes Analysis of Previous Experiment on Drag Reduction.
 - 2.3. Interim Conclusion.
3. Description of Experimental Installation.
 - 3.1. Transonic Wind Tunnel ST-1.
 - 3.2. Plasma Generator of Surface Type.
 - 3.3. Measurement System and Synchronization.
4. Experimental Results.
 - 4.1. Description of the Runs.
 - 4.2. Balances Measurements.
 - 4.3. Visualization of the Interaction.
 - 4.4. Measurements of Input Power.
 - 4.5. Surface Temperature.
5. Simulations and Analysis.
 - 5.1. Simulation in frames of laminar boundary layer model.
 - 5.2. Simulation in frames of turbulent boundary layer model.
 - 5.3. Analysis of data.
6. Conclusion.
7. Program of further activity.
8. References.
9. Acknowledgment.
10. Applications.

1. Introduction.

The main objective of the latest works in the field of Advanced Flow Control (AFC) is to increase efficiency of vehicles and maintain or disturb stability and controllability at atmospheric flight by means of plasma object applications. Plasma formation can effect aircraft's elements by changing their aerodynamic characteristics. It is well known that drag of bodies in airflow consists of three main parts: pressure drag, base drag and friction. In some important cases viscous friction takes the most part. On the other hand the phenomena of flow separation limits wing lift at non-zero angle of attack. Instability of separation line position leads to problems in flight control. A shock induced flow separation is an important problem for bodies of a complex shape. We suggest that plasma technology could solve some of the problems in this field.

AFC technique includes changing of thermodynamic properties of medium by energy deposition in required areas of airflow and addition of ponderomotive forces, especially in case of magnetic field application. Both methods can transform boundary layer structure, which leads to drag decrease (wave drag and skin friction) and lift/drag ratio enhancement. Such possibilities could be realized by means of plasma influence on approach airflow and by means of surface plasma formation.

Traditional methods of viscous friction reduction are based on directed mechanical influence on airflow near body surface, actually, it is a control of laminar and turbulent boundary layer. Such control can occur by means of two ways: change of velocity vector of an external airflow or/and properties and temperature of the surface. An energetic method of boundary layer control (volume energy release to gas near surface by means of electrical discharge, for instance) leads to non-trivial response. This work analyses and discusses results of experimental work on influence of energy release from special organized electrical discharge on characteristics of boundary layer near plain plate and profiled plate.

At present there are lots of theoretical and only some experimental works showing that energy release to airflow near/fore streamlined bodies can reduce total drag of those bodies. It occurs at high level of energetic efficiency (sometimes, much more than 1) [1-5]. In a general case drag force at zero lift is represented as a sum of three components: friction drag, wave drag and base drag. The contributions of each of the components to

the total drag on subsonic, transonic and supersonic flight modes differ. In supersonic and hypersonic modes the wave drag is 60% and more of the total value. For modern long-distance airplanes at Mach numbers $M = 0.7-0.9$ friction drag value is approximately 60% of the total drag. Nevertheless, in most cases the attention was fixed on pressure and wave shares of the total drag. Only some works related to plasma effect on L/D ratio and separation zone location [6-9]. Each experiment was made in the unique conditions and with models of different shapes.

The aim of this experimental work is to continue study of the fundamental plasma technology in plasma-airflow interaction area, in particular, to change an aerodynamic friction and separation zones location by means of surface plasma formation on simple models in airflow. In this project, on-board surface plasma generators have been used as a modeling agent.

Another side of the research was comparison of the experimental results with mathematical simulation data and adjustment of the CFD codes in accordance with experimental picture.

The solution of the problem described above is most important in the case of high speed subsonic and transonic airflow for vehicles with vast surface. So, our experiments have been provided in airflow at Mach number from 0.4 up to 0.99 and static pressure from 400Torr to 650Torr, which are typical for airplane flight.

We have experimented with the simplest model shape: plain plate and circular profiled plate. Electrode surface discharge with individual excitation of each electrode has been tested in the work. The main criteria of plasma influence were tangential force change and structure change of airflow near the surface.

Thus, the objective of the project is study of surface plasma influence on viscous friction and position of separation areas on simple models in transonic and subsonic airflow.

The experiments have been made in transonic wind tunnel ST-1 (Mach number 0.4-1.05) which has been equipped with tensometric balances and Schlieren device. Electro-physical measurements have been provided as well as the surface temperature control.

A significant plasma influence on the parameters of airflow near the surface has been found. CFD simulations and analysis of the experimental data have allowed us to show peculiarities of such interaction. A program of further study has been formulated.

2. Background.

2.1. Brief Review. Analysis of some Experimental and Theoretical Works.

2.1.1. Aerodynamic drag

In general case a drag force at zero lift is represented as a sum of three components: friction drag, wave drag and base drag. The contributions of each of the components to the total drag on subsonic, transonic and supersonic flight modes differ. Thus for modern long-distance airplanes at Mach numbers $M = 0.7-0.8$ friction drag value is approximately 60% of the total drag value (fuselage is 30%, and wing friction drag is 20-25%), on transonic modes the contribution of base and wave drag is prevailing, and on supersonic and hypersonic modes the wave drag is 60 % of the total value.

The friction drag is a result of a velocity shift inside a boundary layer close directly to the FV surface. Friction coefficient value, as known, depends on a set of factors, the basic (of them) are Reynolds number (Re), Mach number (M), Prandtl number (Pr), Schmidt number (Sc) which describe the processes of energy dissipation, heat exchange, diffusion, as well as wall temperature value, turbulence level value and surface roughness level value, FV geometry, etc. An influence of each of the factors mentioned has its physical nature. Thus Reynolds number characterizing a ratio between inertial and viscous properties of a boundary layer determines a flow mode in it. In case of a laminar mode the friction drag coefficient can be ten times less than the one in case of a turbulent mode. At the same time Reynolds number increase results in friction coefficient reduction at any flow mode, until the surface roughness influence begins exhibiting in case of a turbulent mode. When Mach number, being a parameter of a similarity on a compression, increases, the friction coefficient also decreases as a result of a boundary layer thickness increase caused by its heating due to dissipation processes. The typical friction coefficient dependence on these parameters and on roughness level is presented in Fig.2.1.1 [10].

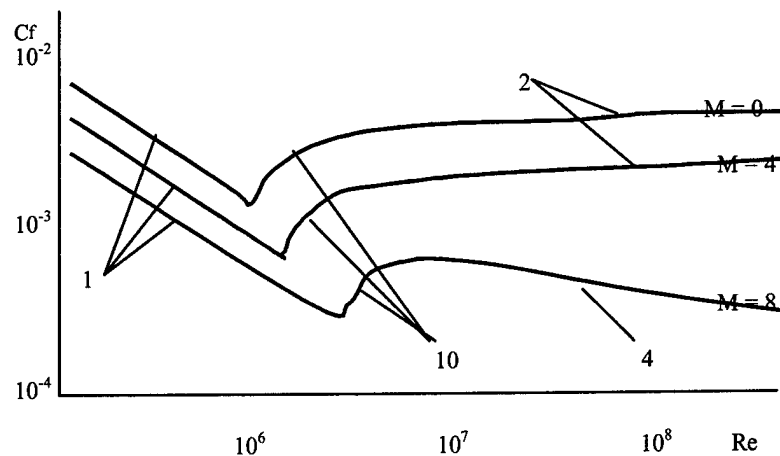


Fig. 2.1.1. Typical dependence of friction drag on Re and M.

1 – laminar mode; 2 – influence of roughness; 10 – transitional mode; 4 – turbulent mode.

The base drag, determined by the value of the base pressure behind the bodies of different shapes (rockets, fuselages with a flat base shear, wing profiles with a thick trailing edge or with a flat shear etc.), at subsonic and supersonic velocities mainly depends on a body lengthening, on a spacing between a fin and a base shear, on a tail part shape, on Mach number and Reynolds number etc. Without dwelling on the known basis of the factors mentioned influence, we'll mark only that at subsonic and moderate supersonic velocities the base drag value for a specific shape body strongly depends on Reynolds number, i.e. on a boundary layer state in front of a base shear. It can be seen from Fig.2.1.2 [11], showing that higher base drag values correspond to small values of friction coefficient. The same dependence takes place for the rotation body as well. In that case boundary layer state (i.e. the Reynolds number influence) is taken into account through the friction coefficient.

The wave drag is conditioned by stagnation pressure losses in bow shock and local shocks, arising in front of different "superstructures" on FV surface (control tools, intakes etc.) under transonic and supersonic velocities. Moreover, as a result of local shock and boundary layer interaction either premature turbolization or separation can take place. In the first case we'll have drag friction increase, in the second — redistribution of pressure forces, which, as a rule, results in undesirable consequences: drag increase, lift reduction, non-stationary loads, control tools efficiency reduction etc. The wave drag

value is defined by shock-wave structure depending on FV geometry and flight Mach number.

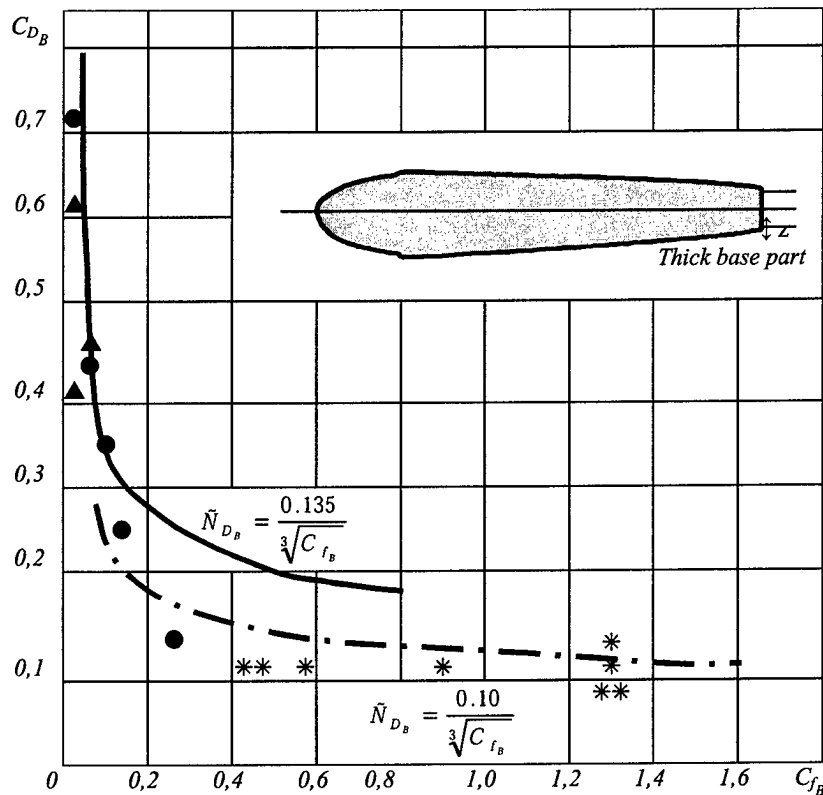


Fig.2.1.2. Drag, occurred due to thick edge or blunt base part of a body.

There is a strong correlation between the factors, influencing the aerodynamic drag components that can be seen from the brief enumeration of these factors. Therefore an attempt of changing of one component results in changing of others and this change can have both identical and opposite signs. For example, friction coefficient reduction in front of the base shear results in base rarefaction increase and, as a consequence, in base drag increase (see Fig.2.1.2).

As the other example the case of wave drag reduction under creation of the upstream separation zones in front of the elliptical nose part with a lengthening 1.67 and a bluntness radius 0.15 with the help of a needle, a needle with a disk attached, a needle with a fan-shaped jet ejection and heat release of a laser radiation in a non-disturbed flow can be done (Table 2.1.1.) [12].

Table 2.1.1.

M		Body	Body with spike	Spike with disk	Spike with jet	Local energy addition
4.15	C_D^w	0.295	0.219	0.178	0.145	0.130
	C_f	0.014	0.005	0.005	0.004	0.005
	C_D	0.309	0.224	0.183	0.149	0.135
	ΔC_D		0.085	0.126	0.160	0.174
17	C_D^w	0.2878	0.0983	0.0921	0.735	0.0650
	C_f	0.0448	0.0261	0.204	0.196	0.0209
	C_D	0.3327	0.1244	0.1125	0.0931	0.0859
	ΔC_D		0.2083	0.2202	0.2396	0.2468

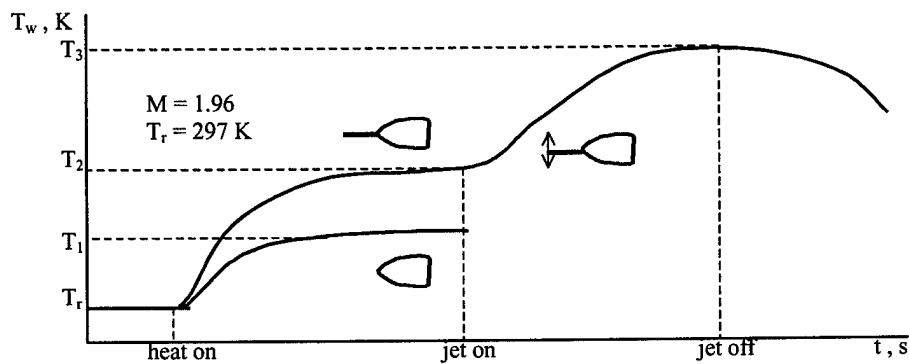


Fig. 2.1.3.[13]

The evaluations of the friction coefficient have been done for the cases mentioned above with the method of "determining" temperature and in all the cases the friction coefficient is found to be two-three times less than the one of the initial body. These data have received experimental confirmation for the case of a fan-shaped jet ejection from a needle tip (see Fig.2.1.3) [13]. Model surface researched point temperature versus time under thin laser beam heating of the surface is presented at this figure. The highest temperature value T_3 for the case of a body with a needle and a fan-shaped jet is evidence of the maximum heat exchange coefficient reduction, what in one's turn basing on the Reynolds analogy allows to make a conclusion about the maximum reduction of the local friction coefficient.

Taking into account the strong contribution of the friction drag component to the total drag under certain flight modes and its strong correlation with other components the ways of friction drag reduction will be considered below.

2.1.2. The Ways for a Friction Drag Reduction.

The existing ways of friction drag reduction are based on a directed influence upon airflow near the FV surface and in fact are the ways of control laminar and turbulent boundary layers.

Under the flow laminar mode the friction drag is ten times less than the one under the turbulent mode. Therefore preservation of a gas flow laminar mode in a boundary layer permitting in separate cases make the drag friction 90% less underlies a way called "laminarization of a boundary layer". As is well known, the laminarization can be reached by means of a surface shape selection, by the suction of small gas portions through the permeable skin, by utilization of elastic-damping coverings and influence of magnetohydrodynamic effect on transition from a laminar flow mode to a turbulent one.

The pressure profile along the external boundary of a boundary layer considerably depends upon the shape of a streamlined surface. Essential influence of a longitudinal gradient of pressure upon the transition had been detected experimentally in 40th already, underlay the elaboration of laminarized profiles. Thus for planes wings for Reynolds numbers $5 \times 10^6 - 4 \times 10^7$ creation of a laminar segment in a boundary layer for the space of (along the) 50-70% of a chord and friction drag reduction more than three times were a success only due to the choice of geometric shape and ensuring of surface smoothness [14]. However it is possible to keep up a laminar flow over major parts of a surface by artificial way only, for example, by the suction of small air portions from a boundary layer through the very thin slots in the FV covering. Systems ensuring a suction, have passed testing of principle under operational conditions at the experimental planes F-94 and X-21 (USA) and HP-113 (England) in 60-th already.

Moreover steady reduction by 40-60% (taking into account an output required for the boundary layer suction) of the planes aerodynamic drag was obtained. Suction is also an effective method for different boundary layer instability suppression. Thus in [15] suction influence on Taylor-Goertler instability accelerating the growth of Tollmien-Schlichting

waves and, consequently, accelerating the laminar-turbulent transition process is investigated theoretically. It is shown that the suction results in flow stabilization as well as in case of Tollmien-Schlichting waves. For the flow stabilization in a boundary layer one can use suction through a porous surface, uniform for a surface part or for the whole surface and suction concentrated in one or in several surface points, defined by the flow character as well. The combination of a periodic injection-suction [16] is also applied. The essential friction reduction can be also achieved by damping of velocity fluctuation in a boundary layer with the use of elastic damping covering of the skin that promotes a laminar mode preservation. The deformation of a surface should be enough for the wall to carry out the work under fluid i.e. to return energy to a boundary layer. In case of wall deformation realized in anti-phase to the unstable Tollmien-Schlichting wave the successful damping of this wave is possible.

Thus in [17] the outcomes of theoretical research of damping capability of already developed waves with the help of vibrator with specially selected parameters are presented. It is also shown in [17] that such devices allow to suppress disturbances in a laminar boundary layer and to delay its transition into turbulent mode.

The fact that at high velocities a gas becomes conductive, makes possible using electrical and magnetic fields generated on FV board for boundary layer parameters control. Thus, for example, magnetic field directed perpendicular to a surface, laminarizes a boundary layer [18] but acceptable efficiency of such influence can be reached only if the gas in a boundary layer is highly conductive.

The friction drag reduction in case of a flow turbulent mode can be achieved, as a rule, with the help of gas injection either through the skin slots or through a porous surface or by using ablative injection. The injection can be either perpendicular to a body surface or tangential, and the last one is more effective [19]. However significant drag reduction can be reached and by means of injection through a porous wall as well (see Fig.2.1.4) [10], and injection effect can be strengthened by using the other kind of gas.

The other possible way of friction drag reduction is the application of fine-ribbed (-edged) surfaces with the edges directed along the flow. The outcomes of experimental researches [20, 21] have shown, that with appropriate edges geometry drag of a plane plate in a subsonic flow ($V = 5-100$ m/s) can be reduced by 8-10%.

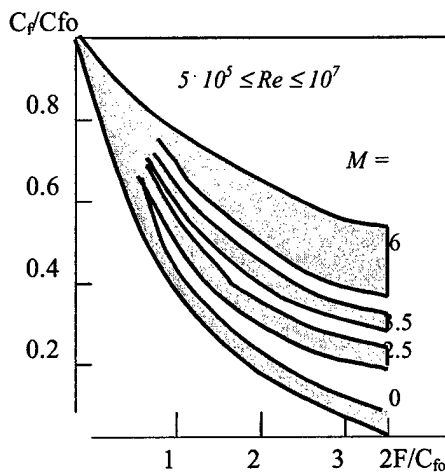


Fig.2.1.4. Surface friction decrease by air injection ($F = \frac{\rho_l V_l}{\rho_\infty V_\infty}$).

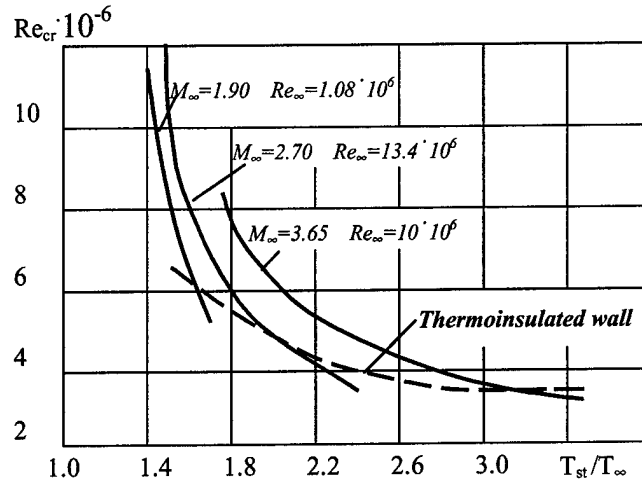


Fig.2.1.5. Critical Reynolds number dependence on relative temperature of a wall and Mach number M_∞ .

Considering this or another way of friction drag reduction it should be kept in mind that a laminar boundary layer is more predisposed to a separation than a turbulent one. Therefore an influence on a boundary layer in order to reduce friction drag raises the possibility of its separation that can result in the appearance of non-computational (calculated) modes. If these modes result in more negative consequences than the friction increase it is necessary to take measures for separation preventing. Such measures can be body surface shape change or boundary layer turbulization by application of ink or mechanical vortex generators with a various design and surface arrangement [22]. The opposite case is possible as well - for example, boundary layer turbulization in order to (with the aim of) separation shift at "thick" low-streamlined bodies (an orb) and at "thin" bodies (wing profiles). In the first case, providing base drag reduction with friction drag increase due to turbulization we obtain reduction of total drag. In the second - the friction drag increase value exceeds the base component reduction value what results in the total drag growth. The theoretical principles of all these methods are presented in [23] and the examples of their practical realization can be found in [22, 11].

It should be noted that methods of friction drag reduction considered are based on either removal of high-entropy gas layers at the wall (suction), or additional mechanical energy transfer to these layers (mobile walls, tangential ejection, mixing intensification with upper layers of a boundary layer etc.).

Other well-known ways of friction drag reduction use wall heating or wall cooling, as the wall temperature change influences a lot both the drag value itself under this or that flow mode and laminar-turbulent transition, i.e. the critical Reynolds number value. It is known that heat supply from a wall to a boundary layer decreases velocity gradient increasing the layer thickness that results in reduction of friction stress. We observe opposite picture when wall cooling. At the same time increase of the wall temperature causes earlier transition, i.e. results in reduction of critical Reynolds number. Fig.2.1.5 [24] presents the outcomes of experiments on investigations of relative wall temperature and Mach number M influence on critical Reynolds number for a plane smooth plate. Critical Reynolds number increases with M increase at the same relative temperature, since the heat rejection is increased. The lower dashed line connects points corresponding to the thermal-insulating surface. In this case the influence of Mach number is of other sort: critical Reynolds number decreases with Mach number growth. The physical explanation is that the relative wall temperature increases with Mach number at the thermal insulating surface grows. As a result the boundary layer thickness increases, the velocity profiles completeness decreases, and the laminar boundary layer becomes less steady. As it could be seen well-known methods are based for the particular body on the influence on a boundary layer using as a rule the wall condition change.

Lift Control.

The ways of lift increase at the boundary layer control are based, as a rule, on separation prevention and delaying for a particular body or on a controlled separation generation. These methods include well-known mechanical methods (dashboards, trimmers, rollers, slats, rotated cylinders installed at a wing leading edge, trimmer with a free streamline) or gas-dynamic (injection, suction etc.) methods mentioned above.

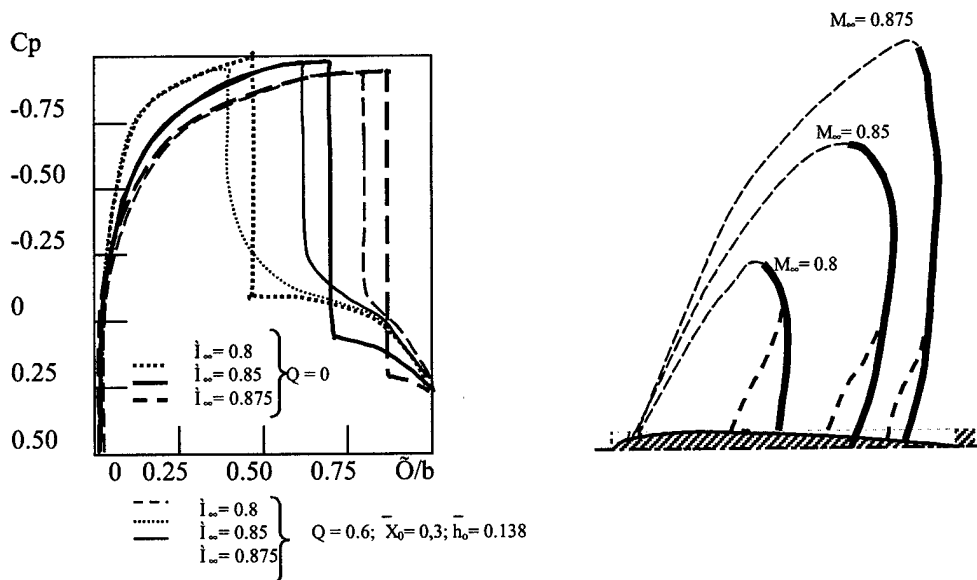


Fig. 2.1.6. Influence energy addition on pressure distribution.

Recently in search of new economic and simply realized methods of boundary layer control the possibility of control by means of gas property and gas state changes in a boundary layer itself and in an external non-viscous flow is considered. This direction is connected to the development of power methods of streamlining control based on energy supply to a flow streamlined FV. Though the theoretical and experimental researches carried out within the framework of this direction are mainly devoted to the wave drag reduction, the results of some of them demonstrate the possibility of influence on a boundary layer as well. Thus in S.K. Korzh computational work (in printing) transonic streamline of NASA-0012 profile with local energy supply in supersonic area in front of local shock is considered (see Fig.2.1.6). It can be seen from the figure that both shock position and longitudinal gradients in an external flow can vary depending on Mach number \bar{M} of an undisturbed flow with energy supply that can influence positively the

transition or separation of a boundary layer.

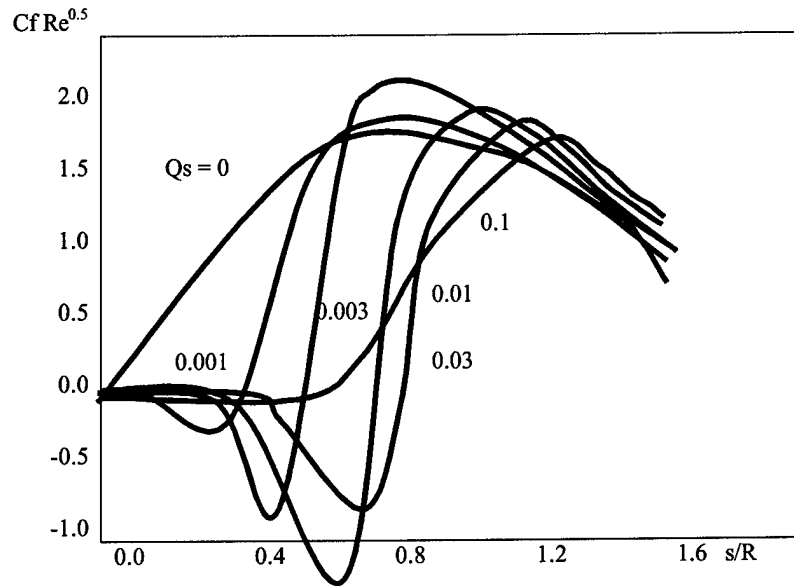


Fig.2.1.7. Surface friction distribution along body ($M = 3$; $Re = 10^4$).

The paper [5] can be considered as the other example of energy supply influence on friction drag. Here an orb streamlining by a supersonic gas flow with local energy supply to the undisturbed flow is considered. Fig.2.1.7 shows the distribution of a local friction coefficient along an orb surface. It can be seen that the friction coefficient at the orb part from a critical point up to a reattachment at various values of energy supply is much less (and even becomes negative) but after flow reattachment it becomes a little bit higher than in case of the orb streamlining by the undisturbed flow. In ref. [26] the influence of the local heat supply to the plate in a supersonic flow on the pressure and friction distribution is investigated on the basis of the Navier-Stokes equations solutions (Fig.2.1.8, 2.1.9). It is also shown that in a vicinity of heat- and mass supply location closed separation area and area with high excessive pressure are generated. In a reattachment area friction stress becomes higher than the one in the beginning of the plate and at the downstream plate part it is higher than the one in case without heat- and mass supply (it becomes negative in separation area as well as in ref. [5]). The essential pressure increase generates high cross-sectional force at a zero angle of attack.

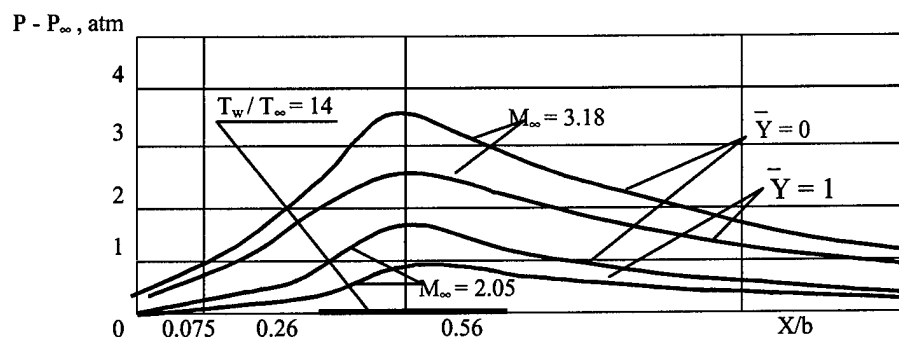


Fig. 2.1.8. Pressure distribution along plate.

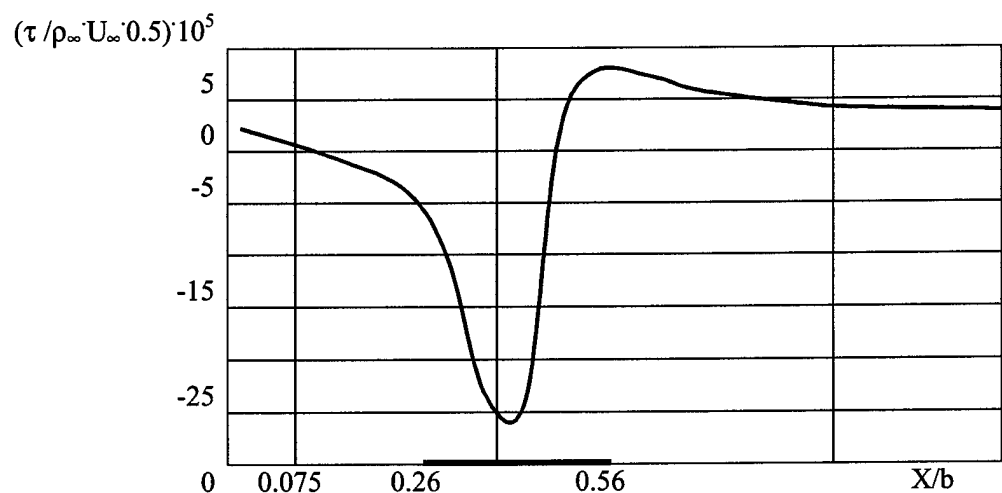


Fig. 2.1.9. Surface friction distribution along plate.

In ref. [26, 27] volumetric energy supply in rectangular area of laminar and turbulent boundary layers on a plate at number $\dot{I} = 3$ was considered. In ref. [8] influence of energy supply to a turbulent boundary layer also was investigated but in contrast to the mentioned above conditions of constant wall temperature the condition of thermal insulating wall was used. Fig. 2.1.10 shows the outcomes of calculations of a turbulent boundary layer indicating that energy supply can be an effective means of friction drag reduction.

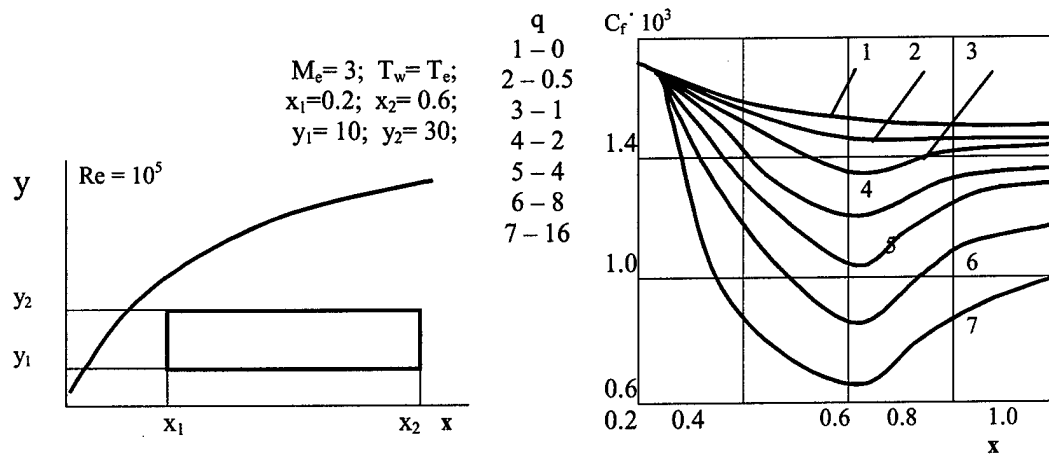


Fig. 2.1.10. Friction coefficient dependence on energy addition.

In a number of M.N. Kogan's works (see, for example [28]) the possibility of laminar boundary layer stabilization by means of plate heating at a leading edge was studied. It is shown that the heating increases stability of a laminar boundary layer. The result is interesting especially as usually such effect because of known reasons results in wall cooling. Electro-gasdynamic influence on the development of the small disturbances in a boundary layer at the plate and in the thin profile was considered in [8]. Here the unipolarly charged ionic jet spread along a surface is considered. The system of electrodes used for an ionic jet in glow discharge generation was simulated by two semi-infinite gauze electrodes (not causing a flow disturbances) installed in sections x_1 and x_2 of a profile perpendicular to a running flow and by one electrode inside a profile in its tip. It was shown that at the electro-gasdynamic streamlining Reynolds number of a boundary layer transition could increase up to 13% for a plane plate and up to 8-11% for a thin profile.

Interdependence of parameters.

All samples above show that a lot of different factors defines a behavior and conditions of a boundary layer. Namely, these are three main groups:

- parameters and conditions of outer non-viscous, in relation to boundary layer, airflow;
- parameters of a gas and flow inside boundary layer;
- parameters and conditions of wall itself.

A value of friction tension depends on Mach Number of non-viscous flow and longitudinal gradient of velocity strongly. From the other side a degree of initial turbulence essential influents on a boundary layer instability development. It effects on laminar-turbulent transition point, i.e. on a critical value on Reynolds number.

Roughness of a streamlined body wall exerts a similar influence as a degree of initial turbulence. At turbulent mode the roughness of a wall defines a friction tension. Besides, a curvature of the wall (influence of centrifugal forces), permeability of surface (blowing out, sucking of a gas through the wall, erosion of wall substance...), flexibility, relative temperature of the wall, catalytic ability of a wall surface influent on a friction drag and a separation point. Two last factors are rather important for a high temperature, chemical active layers. Recombination will do on a different way in depends on relation between a wall temperature and stagnation temperature of flow. It directly influents on a value of thermal load on a wall and on viscous tension. A catalytic ability of the surface also effects on processes inside of boundary layer.

As a sample a temperature distribution on a surface of thermal protective plate in a subsonic jet of dissociated air is presented in Fig.2.1.11 [30]. Here 1 – low-catalytic coating, 2 – high-level catalytic coating (chrome-nickel composition), 3 – at local high catalytic insertion, 4- position of the insertion. The result is well seen.

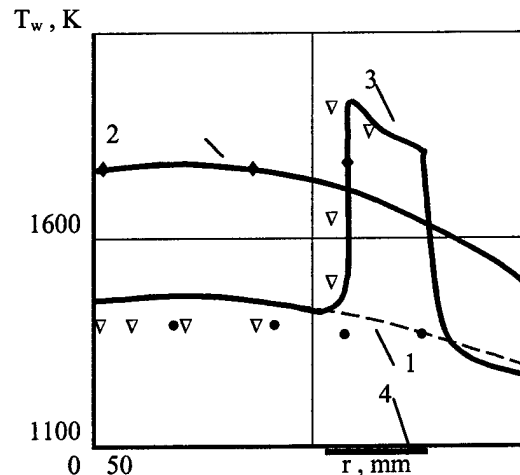


Fig. 2.1.11. Influence of a catalytic property of surface on temperature in dissociated airflow.

Besides of factors in outer airflow and conditions on a wall, role of gas properties inside of boundary layer is important as well as thermal and chemical processes. They are viscosity, heat transfer, diffusion, character and intensity of direct and inverse chemical reactions, rate of them and relative rates of relaxation processes. An influence of some of them one can see in Fig.2.1.12 [24].

Here the dependencies of friction factor on Mach number are presented at different Prandtl numbers and different possible degree factor in equations of viscosity. These equations are often used in calculations. Prandtl number shows a relation between heat, which occurs in boundary layer due to viscous dissipation, and heat transfer due to thermal conductivity.

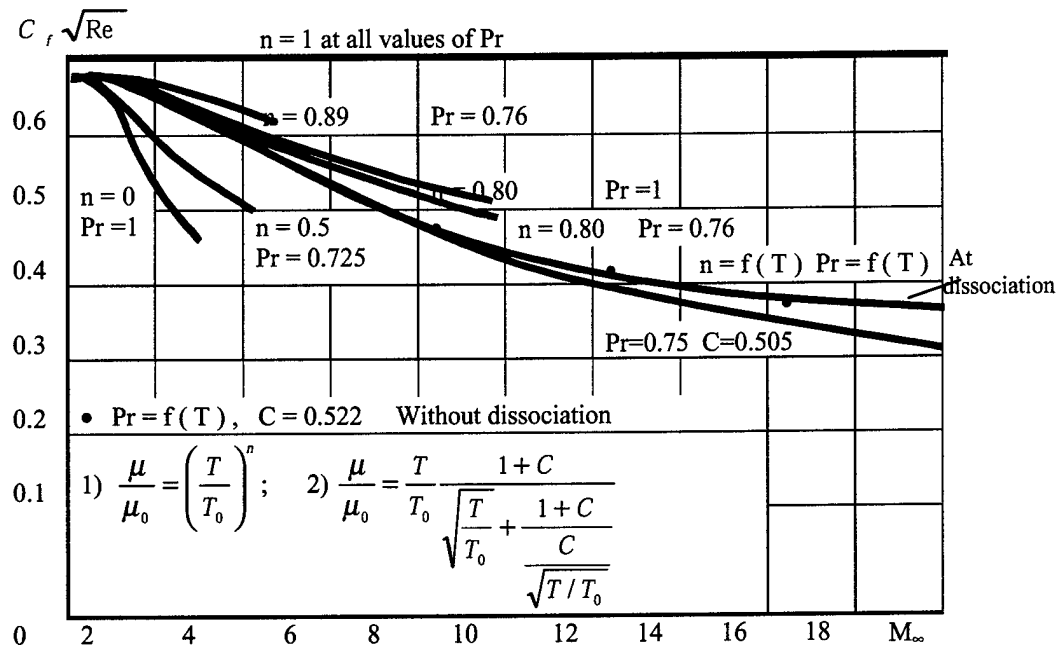


Fig. 2.1.12. Friction factor dependence on Mach number at different suggestions.

Finally, last note about factors, which effect on parameters of boundary layer. At mathematical simulation of boundary layer problem on continuation there was defined that initial data on left edge effect on BL development below in flow. At the same time they (initial condition) depend on formation processes of BL. An essential difference exists in initial state of turbulent BL in case of development at reconnection after laminar separation or in case of laminar-turbulent transition. The similar difference might be at formation of BL in critical point of blunted bodies in supersonic airflow in dependence on condition in points of reconnection on bodies with nose needles. A further development of BL depends on type of transition [11] or initial conditions. At any cases (on profiled bodies and plane plate) viscous tension has a maximal value in places of BL occurring. It shows that namely in such places loses of **mechanical energy** are maximal. So a parameter, which present ratio a thickness of energy loses via thickness of impulse loses, has a significant importance. Seems that namely on this reason a gas blowing out near fore part is the most effective [23]. Moreover, heating of simple plate near fore edge decreases a friction drag and leads to stabilization of laminar boundary layer (in contradiction with general conception) [26,8].

2.2. Navier-Stokes Analysis of Previous Experiment on Drag Reduction.

2.2.1. Experiment's description.

The model experiments on the reduction of the aerodynamic drag of axially symmetric bodies were fulfilled by means of plasma jets blowing and DC discharges in 1997-1998 in frames of EOARD-MTC Contract [32]. Some results are described in ref.[35]. An analysis of the results has been made in 1998 in frames of APL/JHU-MTC Contract [33]. Here we summarise an important data and conclusion of that work due to their significance for this work.

The statement of the experiments in the most general form looks as follows: the plasma formation is created near the AD's model, which is placed into an approaching airflow ahead of it or near the lateral surface. The interaction of the plasma formation and the airflow changes the structure of the flow and physical properties of the air. First of all, it effects the thermodynamic properties those results to the redistribution of the pressure on model's surface. Thus the effect of the drag reduction and the active control of lift in such a statement does not cause any doubt now. But the main task is to obtain high energetic efficiency of such influence. At the most cases using a body with an optimal AD shape has to lead to decrease of the efficiency. This behaviour is well demonstrated in Fig.2.2.1. [4]

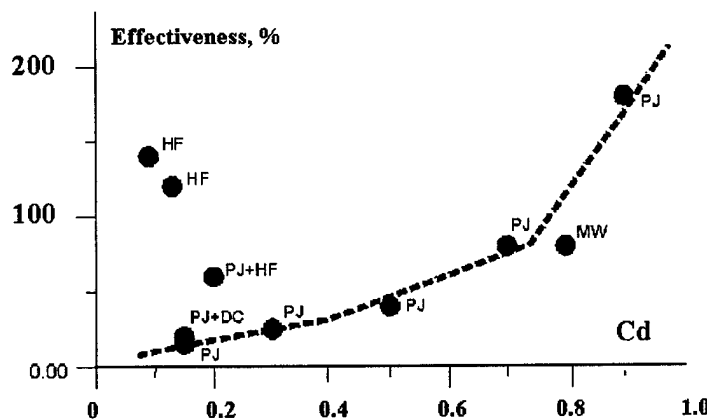


Fig.2.2.1.

Effectiveness of drag reduction by means of plasma formation in dependence on a "quality" of AD model shape.

From the other side even at well-streamlined body the experiments show a visible plasma effect in a drag force. The most probable explanation that the effect is related to friction force decrease.

In References [32,35] there are described P/A experiments with the axe-symmetric model with the blunt cone and a spike in the head part. On the surface of the head part there were located the sectionalised electrodes, on the top of the spike there was located the anode. Polarity of the electrodes could be changed. The drag reduction in these experiments was 10-20% regarding the discharge power and to the current direction. There are different kinds of DC discharges could be obtained near the surface of model at the same electrode configuration.

In References [34,33] there are described P/A experiments with the axe-symmetric model with the optimal shape of the nose part for the Mach number 1.8-2.0. The main dimensions of the model were: maximal diameter 40mm; length of model 290mm; length of fore-body 105mm; distance from nose to DC electrodes 50mm. The electrodes were stacked in slits of a detail. The isolation of the wire withstands pulse voltage no less than 30kV. The same wire brings power to an internal conductor of erosive gun (initiator of the main discharge). DC discharge in the flow has the characteristic filament- like structure. In this case the width of separate plasma filament does not exceed units of mm. These filaments are in dynamic development in the discharge gap, they appear and disappear in it. The frequency of these filament fluctuations was about 10 kHz. The dimensions and luminosity of the plasma formation at the model were determined by the current of the discharge, the gas flow velocity and the static pressure in the flow. At the grounding of one of the sectional electrodes and at the discharge total current $I_d < 1A$ it was possible to realise a transverse circle discharge. At $I_d > 1A$ on the model a filamentary discharge was realised: – a circle discharge combined with longitudinal plasma filaments, issuing from each of the sectional electrodes.

The wind tunnel T-113 of TsAGI is the supersonic set of periodical action, non-return airflow and closed-jet type. The working part has the square cross section of 600×600 mm and the length of 1.9 m. In the setting chamber, five de-turbulizing grids have been installed. For realisation of the low static pressure in the working part of the wind tunnel, two supersonic ejectors are used.

Operation condition:

Static pressure	140, 200 and 300Torr,
Medium	air;
Airflow velocity	Mach number $M=1.78$;
Reynolds number	$Re=10^5-10^6$
Average input power DC discharge	$W_m=0.3-3$ kW
Operation mode	continuous
Operation time	$T=2-10$ sec

The Schlieren photo of model with DC discharge on the surface are shown on Fig.2.2.2.

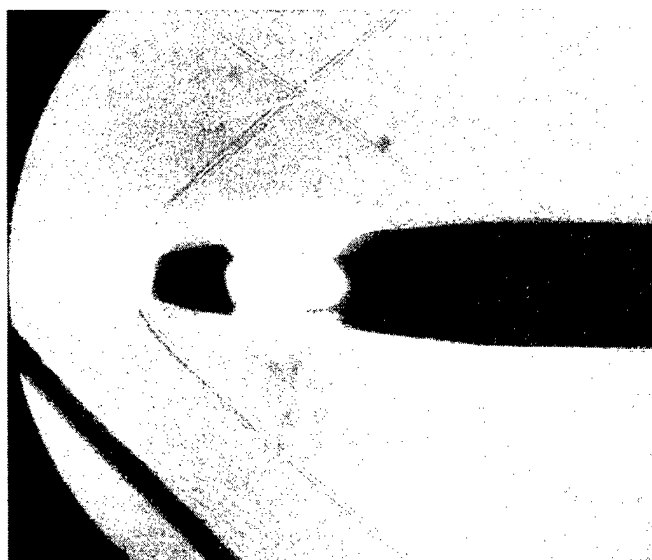


Fig.2.2.2. Schlieren photo of standard DC discharge on the surface of AD model. Well seen a plasma layer near a model surface.

The investigations of the DC plasma generator influence on the aerodynamic characteristics of the AD model were carried out at the «zero» angle of attack. Below the results of experiments are grouped according to the static pressure. All results we tried to represent in table 2.2.1. Here P_{st} is the static pressure of experiment, W_m is the mean power of discharge, J is the current of DC discharge, V is the gap's voltage of DC discharge. The data in the Table are taken from MTC report and [34].

Table 2.2.1.

Pst, Torr	DC parameters, Wm, J, V	Drag Reduction	Initial drag factor	Energetic Efficiency , %	Relative Input Power, %
140	2.4kW	4.6%,	0.17	8.1	57
200	4.2kW, 4A, 900-1000V	7%	0.18	10%	70
200	3kW, 2A	7%	0.17	20%	35
300	4.8kW, 3.5A, 1350-1560V	4.5%	0.16	6%	67
300	1.3kW, 1A,1300V	4%	0.2	20%	20

2.2.2. Calculations.

The numerical investigations of the problem of a drag reduction by means of electro-discharge plasma are carried out devoted to both study the process of the gas and electromagnetic field interaction and the gas dynamic aspects of the problem. Most of gas dynamic results has been received on the base of a heat source model when the electromagnetic energy absorption is simulated by the heat deposition with intensity distributed by given law in the finite flow domain.

With linearized approach it was shown that the energy supply into a segment ahead of a thin axis-symmetric body is very effective for the wave drag reduction [36,37]. Possibility of the flowfield radical change and decreasing of the wave drag by a small energy supply to the local region upstream of a blunt body is demonstrated in [2,38]. The modification of super-sonic flow over a cylinder with appearance of narrow rarefied channel upstream is examined in [39]. The influence of local energy supply on the wave drag is studied for axis-symmetric flow over sphere in [40] and for elliptic nosed body in [41]. An appearance of a separated zone and a considerable wave drag reduction (up to 50%) are noted. The investigations of a 2-D flow restructuring in the shock layer of a sphere and a drag reduction phenomenon by the energy supply are performed in [42]. It is

established that saved energy multiply exceeds a supplied one. 3-D flows with the energy supply in a shock layer ahead of the blunt bodies are studied in [43,44]. The obtained results are supported the opportunity of the influence by the energy supply on the lift-to-drag ratio and angular momentum characteristics.

In all previously mentioned papers the authors used the model of inviscid thermodynamically perfect gas with constant specific heats. Recently a number of papers appeared using the model of viscous heat conducting gas. In [45] some results for supersonic flow near spherical bluntness based on full Navier-Stokes equations are presented. The analysis of obtained data showed that the essential drag reduction can be received at rather small values of the heat supply intensity, at which the heat load is increased relatively weakly.

In the present report the numerical study of a supersonic axis-symmetric air flow through the isolated heat source, over sphere forebody with a heat source in the free stream and over TsAGI experimental model with wall heat deposition are performed. The computations are carried out on the basis of Navier-Stokes equations for a thermal equilibrium air model through the finite volume approach. The effects of local energy supply on flow structure, aerodynamic forces and heat transfer rate are analyzed depending on heat source strength, size of energy supply domain, the Mach and Reynolds numbers.

Gas-phase model

The air is considered as an ideal $O_2 - N_2$ mixture with the constant species mole fractions X_k equal to 0.21 and 0.79 respectively. The rotational and vibrational energy modes of these molecules are described by the equilibrium "rigid rotator - harmonic oscillator" model with characteristic vibrational temperatures $T_{v,O_2} = 2228 K$ and $T_{v,N_2} = 3336 K$. In this gas-phase model the gas state in the time-space point (t, \vec{r}) may be described by the set of independent primitive variables $Z = (p, \vec{u}, T)$, where p is a pressure, \vec{u} is a velocity vector, T is a temperature. The gas state equation is given by

$$p = \rho R_u T / \bar{M},$$

where ρ is density, R_u is a universal gas constant and \bar{M} is a average molecular weight of the mixture. The internal energy per unit mass e and the heat capacity c_p are defined by expressions

$$e = \frac{5}{2} \frac{R_a}{\bar{M}} T + \frac{R_a}{\bar{M}} \sum_k \frac{T_{v,k} X_k}{\exp(T_{v,k}/T) - 1};$$

$$c_p = \frac{7}{2} \frac{R_a}{\bar{M}} T + \frac{R_a}{\bar{M}} \sum_k \frac{(T_{v,k}/T)^2 \exp(T_{v,k}/T) X_k}{[\exp(T_{v,k}/T) - 1]^2};$$

The viscosity is calculated using a power law variation with temperature, $\mu \approx T^{0.683}$. The thermal conductivity λ is defined from condition that the Prandtl number $Pr = \mu c_p / \lambda$ is constant, $Pr = 0.7$.

Governing equations and wall boundary conditions

The laminar axisymmetric gas flowfields are calculated on basis of the Navier-Stokes equations for the discussed above gas-phase model. The integral form of the time-dependent two-dimensional governing equations in the cylindrical coordinates (x, y, φ) may be written as

$$\frac{d}{dt} \int_S U y dS + \int_{\delta S} \vec{n} \cdot \vec{F} y dl = \int_S \dot{U} y dS,$$

where S is a fixed control domain in any meridian plane (x, y) , δS is a boundary of domain, $\vec{n} = (n_x, n_y)$ is an unit outward normal to δS , U is a set of conserved variables per unit volume, $\vec{F} = \vec{F}^{inv} + \vec{F}^{vis}$ represents a sum of the inviscid and viscous fluxes of U through the domain boundary and \dot{U} consists of the source terms. For considered gas-phase model these vectors are given by

$$U = \{\rho, \rho u, \rho v, \rho e_0\}^T;$$

$$\bar{\mathbf{F}} = \begin{Bmatrix} \rho \bar{u} \\ \rho \bar{u} u + p \bar{n} n_x \\ \rho \bar{u} v + p \bar{n} n_y \\ \rho \bar{u} h_0 \end{Bmatrix} + \begin{Bmatrix} 0 \\ \bar{\tau}_x \\ \bar{\tau}_y \\ \bar{q} + u \bar{\tau}_x + v \bar{\tau}_y \end{Bmatrix};$$

$$\bar{\mathbf{U}} = \{0, 0, (p + \tau_{\varphi\varphi}) / y, \omega_h\}^T.$$

Here u, v are the components of velocity vector $\bar{\mathbf{u}}$, $e_0 = e + 0.5(\bar{\mathbf{u}} \cdot \bar{\mathbf{u}})$ is a total energy per unit mass, $h_0 = e_0 + p / \rho$ is a total enthalpy, $\bar{\tau}_x = (\tau_{xx}, \tau_{xy})$, $\bar{\tau}_y = (\tau_{yx}, \tau_{yy})$ is the x - and y -momentum viscous fluxes respectively, $\tau_{\varphi\varphi}$ is a azimuth component of the φ -momentum viscous flux, \bar{q} is a heat flux. The components of viscous momentum fluxes are corresponding nonzero components of a viscous stress tensor that is determined by expression

$$\bar{\tau} = \mu \left[\left(\frac{\partial \bar{\mathbf{u}}}{\partial \bar{r}} \right) + \left(\frac{\partial \bar{\mathbf{u}}}{\partial \bar{r}} \right)^T - \frac{2}{3} \left(\frac{\partial}{\partial \bar{r}} \cdot \bar{\mathbf{u}} \right) \bar{\mathbf{I}} \right],$$

where $\bar{\mathbf{I}}$ is unit tensor. Heat flux \bar{q} is given by

$$\bar{q} = -\lambda \frac{\partial T}{\partial \bar{r}}$$

The turbulent flow is described by unsteady Favre-averaged Navier-Stokes equations. The Boussinesq approximation for the Reynolds stress tensor is used. At this assumption governing equations for turbulent flow coincide with Navier-Stokes equations if molecular viscosity and thermal conductivity to replace on sum molecular and turbulent (eddy) transport coefficients. For calculations eddy viscosity algebraic Baldwin-Lomax turbulence model is used [45,46]. Eddy viscosity in internal region of a boundary layer in this model is defined by Prandtl-Van Driest formula

$$\mu_t^{\text{int}} = 0.16 n^2 \rho \mu |\omega| \left(1 - \exp \left(- \frac{n \rho u_w^*}{A \mu} \right) \right)^2$$

where n is a distance from surface, $\omega = \partial u / \partial y - \partial v / \partial x$, $u_w^* = (\tau_w / \rho)^{1/2}$ is dynamical velocity, τ_w is skin friction, $A=26$.

In the external boundary layer region eddy viscosity is given by expression

$$\mu_t^{ext} = 0.0168 C_{cp} F_{wk} F_{kl}$$

where

$$F_{wk} = \min [n_{\max} F_{\max}, C_{wk} n_{\max} (\bar{u} \cdot \bar{u})_{\max} / F_{\max}],$$

$$F = n |\omega| \left(1 - \exp \left(- \frac{n \rho u_w^*}{A \mu} \right) \right)^2,$$

$$F_{kl} = [1 + 5.5 (n / n_{\max})^6]^{-1}, \quad F_{\max} = F(n_{\max}) = \max_n F, \quad (\bar{u} \cdot \bar{u})_{\max} = \max_n (\bar{u} \cdot \bar{u}),$$

$$C_{wk} = 0.25, \quad C_{cp} = 1.6.$$

The boundary of internal and external regions is defined from conditions $\mu_t^{int} = \mu_t^{ext}$. The turbulent thermal conductivity is given by

$$\lambda_t = \mu_t c_p / Pr_t,$$

where turbulent Prandtl number $Pr_t = 0.9$.

The un-blown and non-slip wall conditions are used in calculations

$$\bar{u} = 0$$

The both heat isolated and cooled wall conditions are employed also

$$q_w = 0 \quad \text{or} \quad T = T_w.$$

Numerical method

The governing equations are solved in the curvilinear structured mesh through a finite volume approach. At this approach the finite difference equations system consists of numerical analogs of the conservation equations for the quadrilateral cells covering the computation domain and the difference approximation of the boundary conditions. This method yields an approximate solution $Z_{i,j}$ in a center (x_{ij}, y_{ij}) of each cell and in a

center of each cell side $(x_{w,i}, y_{w,i})$ lying on the wall. The cells are built by intersection of the two discrete curve sets. The inviscid fluxes F_G^{inv} through cell sides are calculated from result of the exact Riemann problem solution $Z_G = \mathfrak{R}(Z_G^L, Z_G^R)$ where \mathfrak{R} is the Riemann problem solver. The left and right interfacial values Z_G^L and Z_G^R are defined by the limited one-dimensional extrapolation of z from the cell-centers to the cell sides. The numerical viscous fluxes F_G^{vis} through cell sides are evaluated using the central and one-sided difference formulae of the second order accuracy.

Difference equations are solved by the two-layer implicit iterative scheme based on implicit approximation of the time-dependent Navier-Stokes equations. The (\pm) splitting of the numerical fluxes Jacobians is used in a construction of the implicit iterative operator. Its approximate inversion is realized by the Gauss-Seidel line space marching along stream-wise direction with the LU-decomposition of the block-tridiagonal matrices to be solved in every line step.

The numerical analysis of TsAGI experiments has been performed on a basis of axisymmetrical viscous flow model at presence in the stream near wall a local heat supply region that modeled DC discharge. It is supposed that heat source term in co-ordinate system (s, n) where s is distance along body surface from stagnation point and n - distance from body surface along normal in point with co-ordinate s is written in the following form:

$$\omega_h = a_h \rho G_1(s) G_2(n)$$

Function $G_1(s)$ is given in one from following forms

$$(1) \quad G_1(s) = \left(1 - ((s - s_h) / d_{sh})^2 + |1 - ((s - s_h) / d_{sh})^2| \right) / 2$$

or

$$2) \quad G_1(s) = \begin{cases} 0 & \text{at } s \leq s_h - d_{sh} \\ (s - s_h) \exp(-(s - s_h) / d_{sh}) & \text{at } s > s_h - d_{sh} \end{cases}$$

Function $G_2(n)$ is defined by expression

$$G_2(n) = \exp(-((n - n_h) / d_{nh})^2)$$

The value of a_h is determined from condition

$$2\pi \int \omega_h y dx dy = P_d ,$$

where integrating is performed on the whole computation domain and P_d is input discharge power in the heat. The laminar-to-turbulent transition is described by the weight coefficient $\Gamma(s)$ before turbulent viscosity and thermal conductivity. The value of $\Gamma(s)$ monotone changes from zero to unit in the given range from $s = s_{tr}$ to $s = s + ds_{tr}$.

In the calculations body surface geometry was closed to it for TsAGI experiment model and was specified by following set of relations:

$$\begin{aligned} x_z \leq x \leq x_e : & \quad ((x - x_0) / a)^2 + (y / b)^2 = 1 \\ x_e \leq x \leq x_c : & \quad y = y_c (x / x_c)^{0.62} \\ x_c \leq x \leq x_f : & \quad y = y_c \end{aligned}$$

where $x_e = 2.128$ cm, $x_c = 12.0$ cm, $x_f = x_z + 29.0$ cm, $y_c = 2$ cm, $a / b = 2$, $x_z = x_0 - a$.

Parameters x_0 and a are determined from a condition of smooth interface at $x = x_e$.

Calculations were performed for some combinations of the free stream, gas heating and laminar-turbulent transition parameters. In all variants it is assumed to be: $M_\infty = 1.78$, $T_0 = 260$ K, $s_h = 5$ cm, $d_{sh} = 1.25$ cm, $n_h = 0$, $ds_{tr} = 0.4$ cm. Other parameters are varied. Their values are represented in Table 2.2.2. In this table a dimensionless heat supply parameter Q_h , the drag coefficients C_{px} , C_{fx} , C_x , drag reduction D and heat supply efficiency E are listed also. These parameters are calculated by following formulas

$$Q_h = P_d / (0.5 C_x(0) \rho_\infty u_\infty^3 \pi y_c^2); \quad C_{px} = -2\pi \int (p_w - p_\infty) n_{wx} y ds / (0.5 \rho_\infty u_\infty^2 \pi y_c^2),$$

$$C_{fx} = -2\pi \int (\vec{\tau}_{wx} \cdot \vec{n}_w) y ds / (0.5 \rho_\infty u_\infty^2 \pi y_c^2), \quad C_x = C_{px} + C_{fx}, \quad D = 1 - C_x(Q_h) / C_x(0)$$

$$E = \frac{(C_x(0) - C_x(Q_h)) 0.5 \rho_\infty u_\infty^3 \pi r_c^2}{Q_h 0.5 C_x(0) \rho_\infty u_\infty^3 \pi r_c^2} = \frac{1 - C_x(Q_h) / C_x(0)}{Q_h}$$

Table 2.2.2. Calculations parameters for TsAGI experiment conditions

N.	P, torr	Pd, kW	Qh	Tw, K	G ₁ (s)	s _{tr} , cm	d _{hh} , cm	C _{px}	C _{fx}	C _x	D %	E %
1	140	0	0	300	-	lam	-	0.115	0.0150	0.130	-	-
2	140	2.4	0.79	300	1	lam	0.1	0.118	0.016	0.134	-3.0	-3.8
3	140	4.8	1.57	300	1	lam	0.1	0.120	0.018	0.138	-6.2	-3.9
4	140	0	0	h.i.	-	lam	-	0.115	0.015	0.130	-	-
5	140	2.4	0.79	h.i.	1	lam	0.1	0.118	0.016	0.134	-3.2	-4.1
6	140	4.8	1.57	h.i.	1	lam	0.1	0.122	0.016	0.138	-6.6	-4.2
7	140	0	0	300	-	0.	-	0.116	0.060	0.177	-	-
8	140	2.4	0.58	300	1	0.	0.1	0.119	0.052	0.170	3.7	6.3
9	140	4.8	1.16	300	1	0.	0.1	0.120	0.048	0.168	4.9	4.3
10	140	0.	0	h.i.	-	0.	-	0.116	0.063	0.180	-	-
11	140	2.4	0.57	h.i.	1	0.	0.1	0.119	0.048	0.168	6.7	11.7
12	140	4.8	1.13	h.i.	1	0	0.1	0.122	0.043	0.165	8.2	7.3
13	140	0.	0	h.i.	-	2.0	-	0.116	0.063	0.179	-	-
14	140	2.4	0.57	h.i.	1	2.0	0.1	0.119	0.047	0.167	6.7	11.6
15	140	4.8	1.14	h.i.	1	2.0	0.1	0.122	0.042	0.164	8.2	4.2
16	140	0.	0	h.i.	-	3.8	-	0.116	0.061	0.177	-	-
17	140	2.4	0.58	h.i.	1	3.8	0.1	0.119	0.046	0.165	6.8	11.7
18	140	4.8	1.15	h.i.	1	3.8	0.1	0.122	0.040	0.162	8.7	7.5
19	140	2.4	0.58	h.i.	2	3.8	0.1	0.120	0.046	0.166	6.4	11.1
20	140	4.8	1.15	h.i.	2	3.8	0.1	0.123	0.039	0.162	8.9	7.7
21	140	2.4	0.58	h.i.	1	3.8	0.2	0.120	0.051	0.170	3.7	6.4
22	140	4.8	1.15	h.i.	1	3.8	0.2	0.123	0.045	0.169	5.0	4.3
23	200	0	0	h.i.	1	3.8	-	0.116	0.059	0.175	-	-
24	200	2.4	0.41	h.i.	1	3.8	0.1	0.118	0.047	0.165	5.4	13.2
25	200	4.8	0.82	h.i.	1	3.8	0.1	0.120	0.040	0.161	8.1	5.8
26	300	0	0	h.i.	1	3.8	-	0.116	0.055	0.170	-	-
27	300	2.4	0.28	h.i.	1	3.8	0.1	0.117	0.046	0.164	3.9	14.0
28	300	4.8	0.56	h.i.	1	3.8	0.1	0.119	0.040	0.159	6.6	11.8

Results of simulations.

The results of simulations are shown in Table 2.2.2 and in Fig.2.2.3-2.2.6. The distribution of specific friction coefficient along surface of body (axis X) is presented in Fig.2.2.3 for various location of laminar- turbulent transition point. The following four different cases are presented in the Fig.2.2.3 as following:

“1”- a laminar flow around model, $S_{tr} = \infty$,

“2”- mixture laminar/turbulent flow around model, $S_{tr}=3.8\text{cm}$, $\Delta S_{tr}=0.4\text{cm}$,

“3”- mixture laminar/turbulent flow around model, $S_{tr}=2,0\text{ cm}$, $\Delta S_{tr}=0.5\text{cm}$,

“4”- full turbulent flow, $S_{tr} = 0$.

These results were obtained for the case of static pressure $P= 140\text{Torr}$ and heat insulated surface. Transition Reynolds number calculated on the base of momentum thickness and gas parameters on the outer boundary layer equals to 340 in case No2 and equals to 270 in case No3.

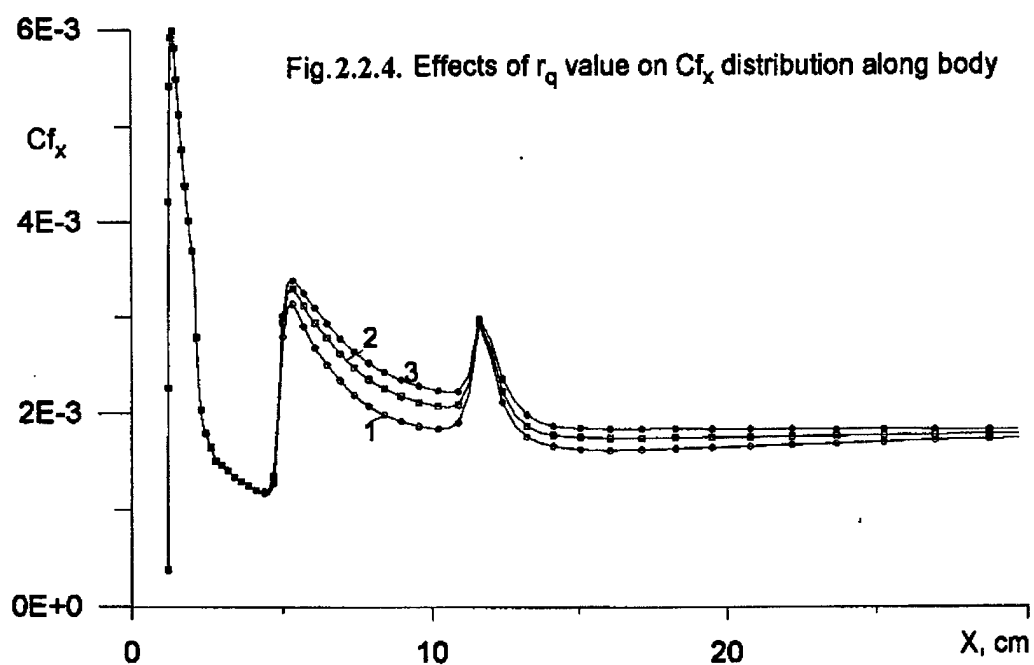
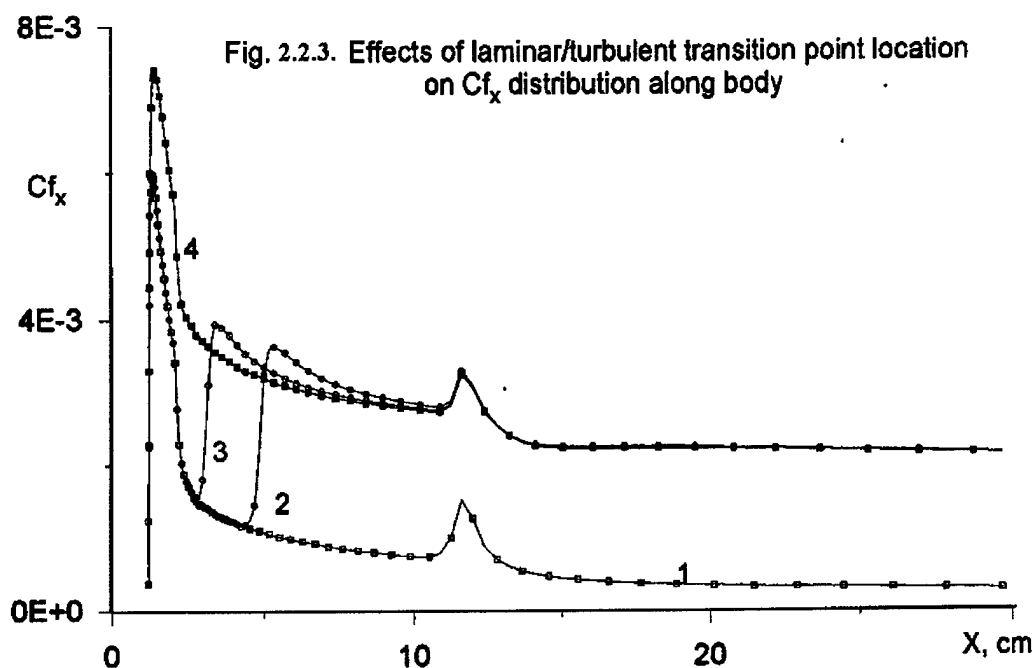
The distribution of friction coefficient along body axis X on location of laminar- turbulent transition point corresponding to the case 2 with heat source is presented in Fig.2.2.4. Heat source has following parameters:

mean power - 2.4 kW,

function $F(s)$ #2, which describes influence of relaxation process in plasma.

location of point of transition:- $S_{tr}=3.8\text{ cm}$,

parameter of function $G(N)$:- $d_{nq}= 0.1\text{ cm}(1)$, $d_{nq}= 0.15\text{ cm}(2)$, $d_{nq}= 0.20\text{ cm}(3)$.



It is seen that heating by DC discharge decreases the value of C_f . This effect increases with decrease of value d_{nq} . Influence of heat intensity distribution along body on C_f is shown on Fig.2.2.5.

The curve No1 corresponds to following condition:

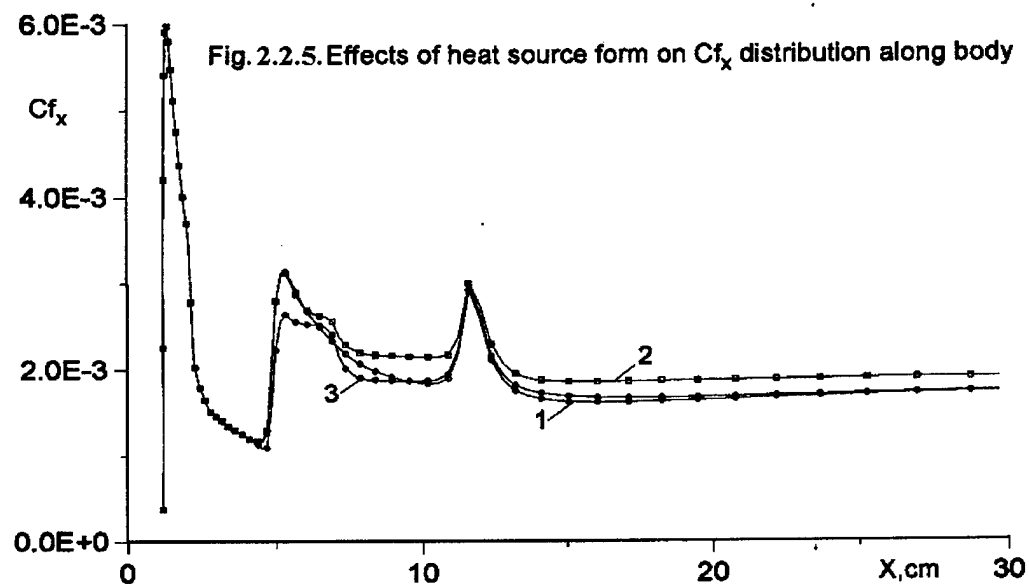
$F(s)\#2$, $Q_t = 2,4 \text{ kW}$, $d_{nq} = 0.1 \text{ cm}$, $S_{tr} = 3.8 \text{ cm}$.

The curve No2 corresponds to following condition:

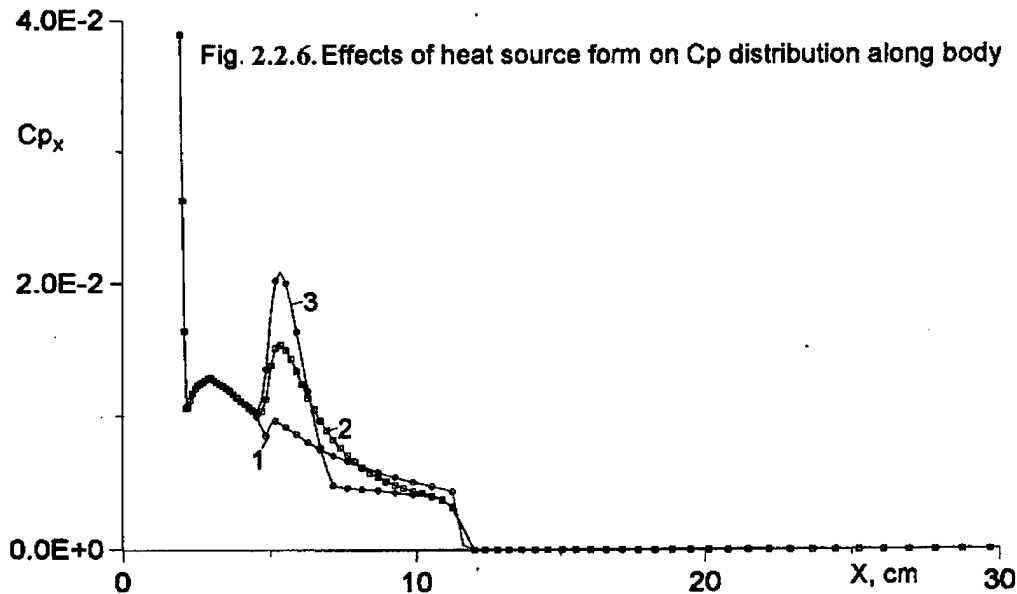
$F(s)\#1$, $Q_t = 1,44 \text{ kW}$, $d_{nq} = 0.1 \text{ cm}$, $S_{tr} = 3.8 \text{ cm}$.

The curve No3 corresponds to following condition

$F(s)\#1$, $Q_t = 2,4 \text{ kW}$, $d_{nq} = 0.1 \text{ cm}$, $S_{tr} = 3.8 \text{ cm}$.



It is seen that decrease of C_{fx} considerably depends on value Q_t and less depends on distribution of power along body surface.



The distribution of pressure coefficient C_{px} along body axis X is shown in Fig.2.2.6. It can be seen that influence of heat source on C_{px} is small. There are a small increase value of C_{px} in the region of heat source location and small decrease in outside of this region. So, summarizing effect of action of heat source is small.

Distribution of pressure P and gas temperature in the flow around model with heat source, created DC discharge, is shown in Fig.2.2.7 and Fig.2.2.8. The parameters of numerical experiment are following:

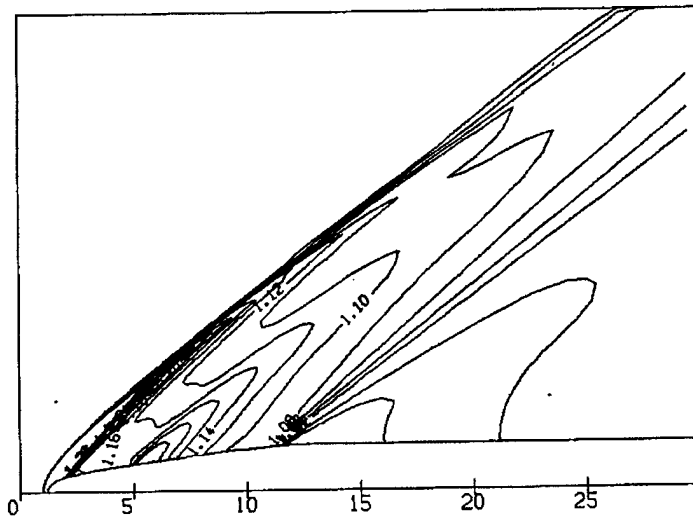
Static pressure, $P_{st}= 140\text{Torr}$,

Mean input power, $Q_i= 2,4\text{ kW}$,

$F(s)\#2$, $d_{nq}= 0.2\text{ cm}$, $S_{tr}=3.8\text{ cm}$,

Heat insulated body surface.

There is generation of weak pressure disturbance near the region of location of DC discharge. This disturbance propagates in the direction down flow stream. Heat gas layer is created by DC discharge. Maximum gas temperature in this layer reaches 356K.



coefficient C_x some decreases (up to ~9 percents). This effect is greater for the heat isolated (h.i.) wall. The drag reduction increases with increasing of heat deposition but with increasing of Q_h the reducing rate drops. The efficiency of heat deposition in considered conditions is very small and it does not exceed 0.15. With increasing Q_h efficiency is reduced. The heat source size increasing leads to decreasing of the drag reduction and heat supply efficiency. The effects of the transition point location and of the form of heat supply distribution along body surface were insignificant.

It is known [48], that heating of body surface can decrease friction coefficient C_f . The simulation gives the heating of body surface up to $\Delta T_w = 200\text{K}$ (close to one, realized in the experiments with DC discharge). It has been obtained that value of C_f decreased in the same way. But the relative decrease C_f value was 2-3 times less than one corresponding to volume (near the surface) heating by DC discharge. Thus direct heating of surface can't explain all experimental results.

Comparison of Tables 2.2.1 and 2.2.2 shows that the good coincidence between experimental and calculated values of drag reduction were obtained. It was possible to achieve by means of laminar-turbulent transition takes into account. So, an experimental fact on drag reduction at plasma influence on a model with a good AD shape can be explained only by reduction of the friction. It is very important result for our work.

2.3. Interim Conclusions.

At volume type of energy input in boundary layer it will be "hot" not only near a point of heating but in region below due to airflow (independently on velocity of outer flow). Below the point (line) of energy input there will be a heated boundary layer and relatively "cold" wall. At least, heat transfer will have direction to the wall. In this case a BL will be stabilized due to more full profile of it. A gas temperature in BL will be changed slower along streamlines due to recombination processes. Thus a local Reynolds number will change slower also.

The most peculiarities of hypersonic BL is a similar to supersonic and subsonic BL with energy release in more or less degree. A main difference is that a heating of BL is provided by means of outer sources (dissipation of electromagnetic energy in discharge, for instance) but not only by dissipation of mechanic power. A power of external source can be controlled outside in accordance with defined task. At high level of input energy and thin BL (high power density) a gas density in BL could occur so low, that mode of flow passes continuous to transitional or free-molecular one. So, a Knudsen number in this case will be less than 1. For example, at altitude 20-30km and gas temperature 3000-10000K Knudsen number will be in range $Kn=0.02-0.1$. Plasma influence is just unpredictable.

Taking into account above notes, a suggested places for a plasma formation (heat release) might be areas with maximal mechanical energy loses, namely: area of critical point and line of reconnection after flow separation, fore part of plates and profiles and areas of shock waves interaction with BL. In last case plasma generation or/and heat release should lead to weakening and displacement of the shock fore flow on supersonic part of the boundary layer (see Fig.2.1.6). It has to effect on longitudinal pressure gradient in area of interaction. A laminar-turbulent transition could remove below. In case of strong shock wave and flow separation due to interaction of BL with SW, plasma formation can prevent separation processes.

Generally, volume type of energy input into a BL will effect on external non-viscous flow. A character of influence depends on specific model of interaction [31] between discharge and gas flow. Two different modes: "streamlining" and "flowing through" are shown schematically in Fig.2.3.1 (a) and (b) correspondingly. Really both mechanisms take place in a different proportion. In first case an influence on external flow is more

than in second one. Speed of flow is important at description of specific mechanism of interaction. At location of such discharge in a special geometrical configuration, like in Fig.2.3.2, there is possible to provide a frictionless flow around a body. In second case an energy release or plasma formation will more influent on a boundary layer itself, in particular, will lead to increase of a kinetic energy of gas.

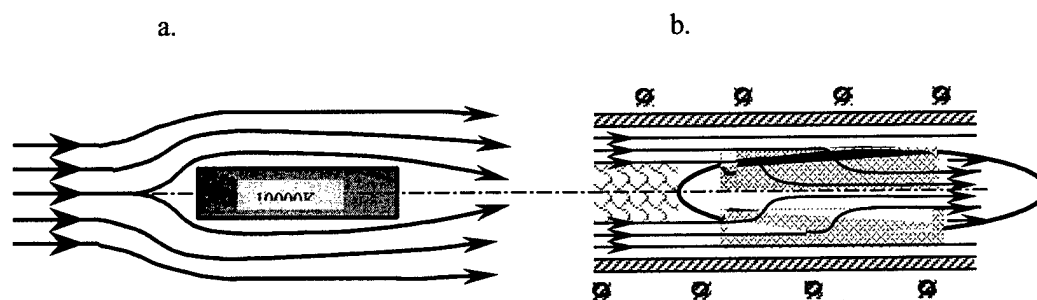


Fig.2.3.1. Two modes of plasma streamlining.

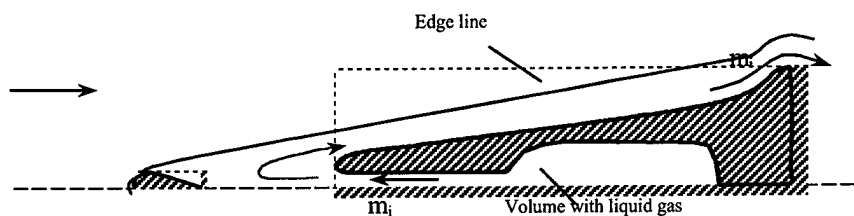


Fig. 2.3.2. Frictionless mode of streamlining.

So, two important conclusions should be done.

1. Numerical simulations show that the part experimental facts in a field of Plasma Aerodynamics (particular at optimal AD shape of the model) can be explained by a plasma influence on parameters of boundary layer and near surface layer as well as on position of laminar-turbulent transition and separation lines location.
2. Analysis of available data arrows on the most effective points of an energy deposition: near (fore) places with a maximal mechanical energy loses.

3. Description of Experimental Installation.

Experimental installation consists of the following parts:

- Transonic Wind Tunnel ST-1 with a control panel;
- Aerodynamic Model with a build in balances;
- Plasma Generator and Power Supply;
- Visualization system;
- Measuring devices and synchronization system.

3.1. Transonic Wind Tunnel ST-1.

Transonic wind tunnel ST-1 concerns to the type of ejector open-ended short-term operation tubes. It consists of a fore-chamber (1), nozzle (2), operating (test) section (3), Mach number regulator (4), ejector (5), diffuser (6), receiver (7) and high-pressure line with an adjusting valve (8) and setting valve (9) (Fig. 3.1.1).

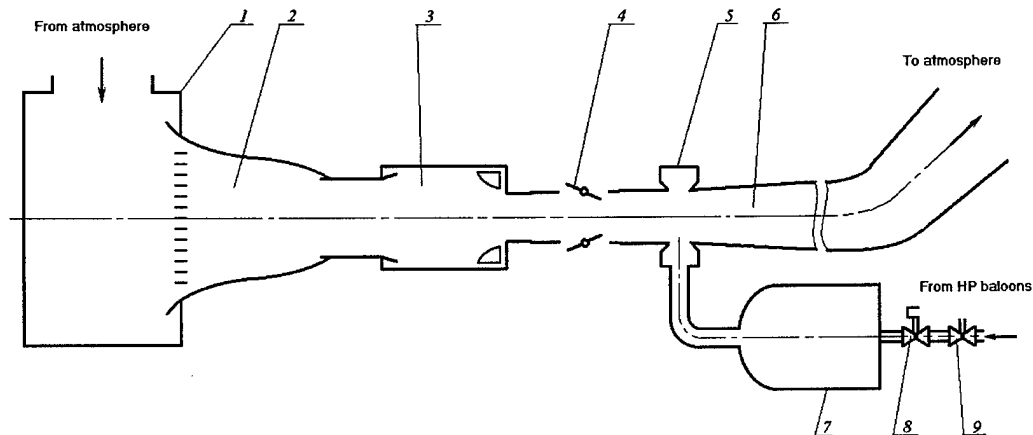


Fig.3.1.1. Principal layout of WT ST-1.

The fore-chamber communicates with the atmosphere and provides an air supply to the nozzle. The flow velocity in it is so small that the deceleration conditions existence is possible to be assumed.

In the nozzle the flow is accelerated. The highest outlet velocity value can reach the sound velocity value. The further velocity increase takes place due to flow extension.

The operating section is closed and has a rectangular cross-section of 300x250 mm.

The under test model is set on the special holder in the operating section. For the optical (direct) observation and model monitoring there are several windows closed by protective glasses in lateral walls of an operation section.

The flow Mach number regulation is made with the help of the shutters (4) set in tunnel walls behind the operating section. At the closed shutters the air flows through the operating section and therefore flow velocity in it will be maximum. At the shutters opening the flow velocity in the operating section decreases proportionally to the shutters turning angle value as the air will be partially sucked through the opened shutters, passing the operating section.

The ST-1 tunnel allows obtaining the transonic flow with Mach number that can vary continuously from 0.4 up to 1.17 for a small model.

The high-pressure air is supplied from the receiver to the ejector with the help of which the pressure difference necessary for the obtaining of the accounted velocity value in the operating section is created. Through the ejector loop circuit high-speed air in-flowed to the diffuser and carrying away the operating section air creates a flow in it. Then this flow is ejected in the atmosphere through the diffuser. The flow deceleration takes place in the diffuser in such a way that the energy losses were maximal.

The ejector operation stability is provided for the receiver dampening pressure fluctuations arising during the air throttling by the regulating valve.

The ST-1 tunnel switch-in and cut-off are realized with the help of shutoff and regulating valves which are operated by the remote control unit as well as the Mach number regulator shutters.

The airflow Mach number in the operating section is determined under the aerodynamic functions tables by static pressure to stagnation pressure ratio. The static pressure measurement is realized with the sensor whose sensing element represents the thin-walled metal chamber with bonded resistance strain gauges.

For the monitoring of the model streamlining by the airflow in the tunnel operating section a Schlieren device is applied — a device IAB-451 assembled by the mirror-meniscus optical scheme.

Model.

The scheme of the model is presented in the Fig.3.1.2.

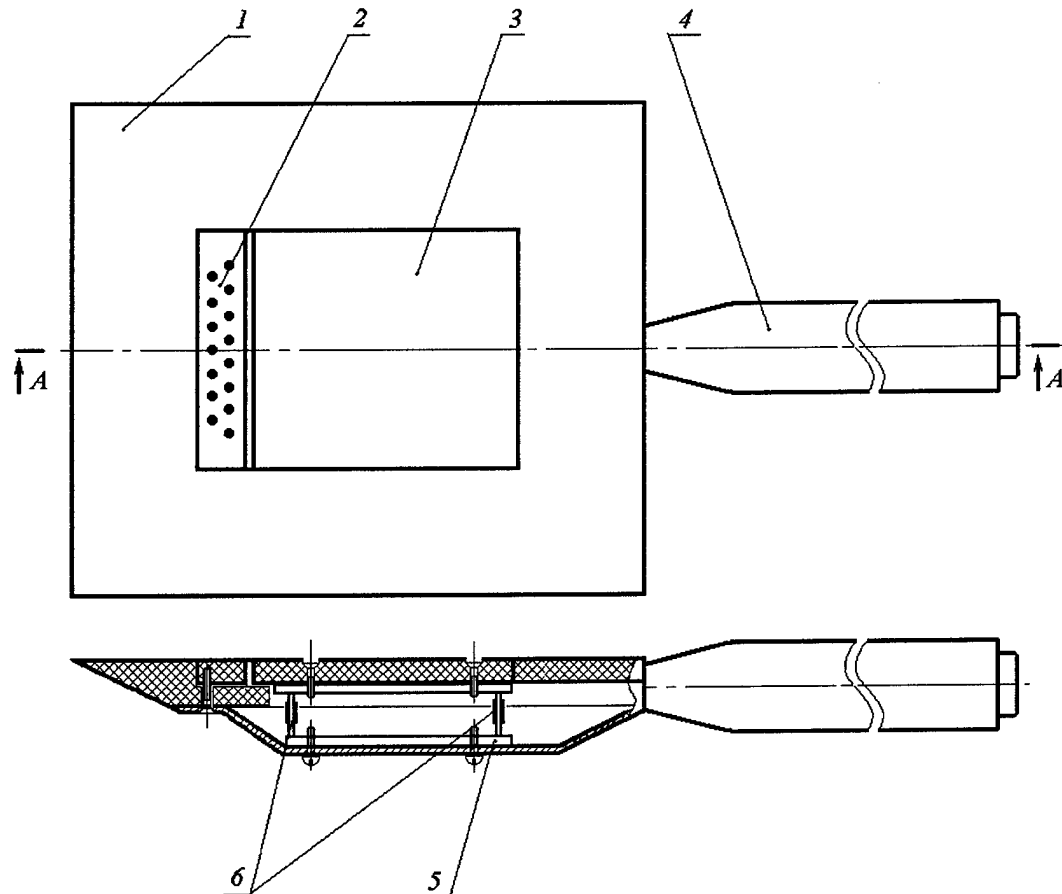


Fig.3.1.2. Principal scheme of the model for ST-1 runs.

For the research of the friction reduction on a surface with the help of the surface plasma a special model has been designed. It consists of the following basic elements:

1. · Aerodynamic body, installed from one window up to second one;
2. · Immovable (small) plate with 17 electrodes;
3. · Movable (large) plate without electrodes in this series;
4. · Holder with the strut;
5. · Strain gauge balance;
6. · Tenso resistive strain gauge bridge elements.

The basic element of the model is the body (1) that plays a role of a structure carrier. The model body is right-angled with a sharpen leading edge and fastens on the model holder.

The body consists of two parts. The base part represents a metal duct with housing for the balance. The top part represents a dielectric wedged nose plate 1,5cm width with a slot for the installation of large and small plates with electrodes. Its upper plane is aligned to the up-running flow direction. The screws connect body top and bottom parts.

Holder (4) represents a hollow steel cylinder with a nose as a truncated cone. The model body is fastened directly to the cone forward part. The balance wires are laid inside the holder. The model is set in the tunnel pylon with the help of the holder.

The large plate has no electrodes in this series of experiments. It is attached to the dual-component strain balance (5) that is inside the body. The balance is intended for the large plate aerodynamic drag measurement. The balance represents a steel frame that is a sensing element. The frame fastens to the back wall of the model body bottom part. The large plate fastens to the frame top part by the screws. For the force measurements four tenso resistance strain gauges (6) are located at the balance frame. The resistance strain gauges are assembled in a semi-bridge circuit. The signal from them is amplified with the help of the low-frequency amplifier 8×10^4 that is the member of the measuring complex.

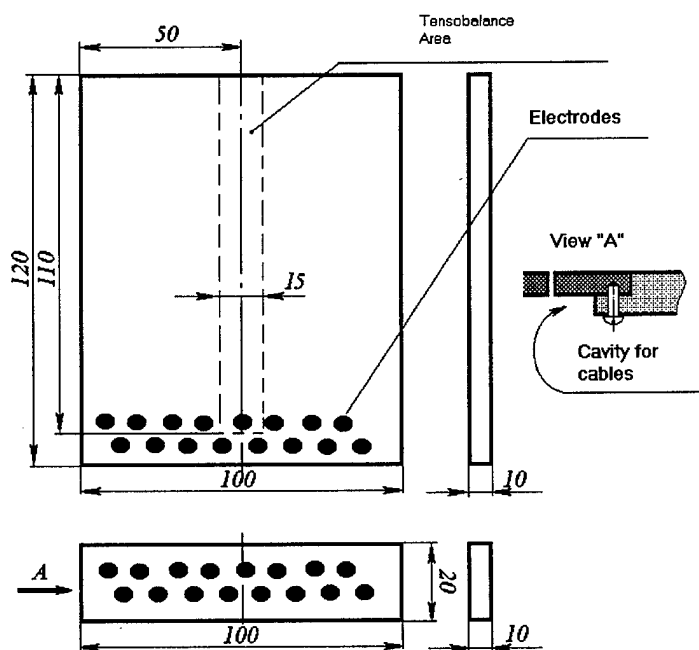


Fig.3.1.3. Geometry of the model for a ST-1 experiment. The electrodes on a large plate can be used for the next step of the work.

Large and small plates (2 and 3) are right-angled. At the small plate there are the electrodes for the electric discharge realization. The feeding wires from the electrodes are removed in a base part of the model body. The small plate with electrodes is fixed at the

body by the thermosetting adhesive.

Photo of assembled model for test in ST-1 is shown in Fig.3.1.4a. More detail image is presented in Fig.3.1.4b. Also here the electrode system is seen. Electrodes have been made from a cooper alloy. The wires have a good double Teflon insulation.

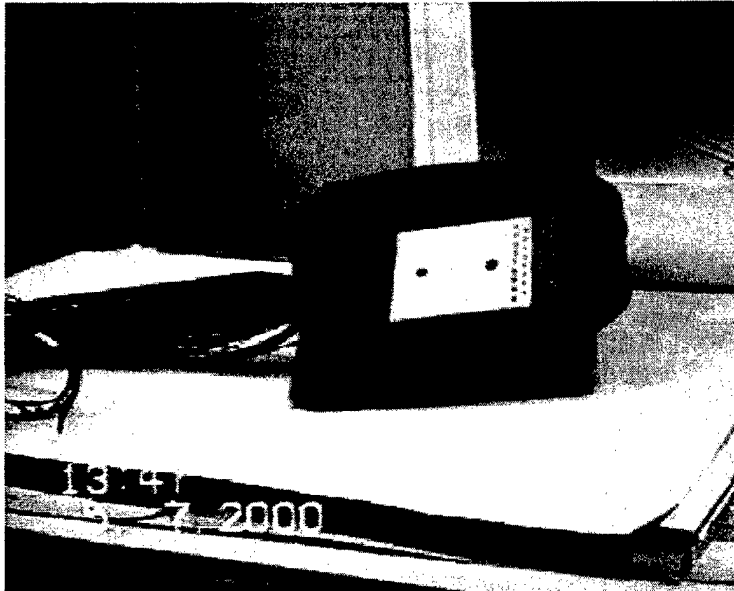
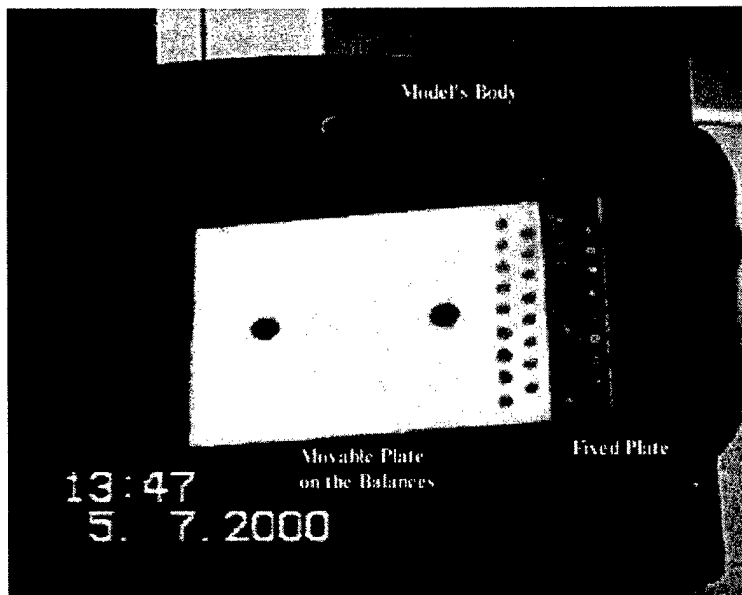


Fig. 4 a, b.
Photos of the
equipped model for
ST-1 runs.



3.2. Plasma Generator of Surface Type.

Pulse repetitive multi-electrode surface discharge is used for a plasma excitation at the experiments. Electric energy input to the plasma volume 2-15kW at area of plate's surface 0.001-0.015m². Different schemes of plasma location in respective to test plate position can be used. The most prospective configuration was a plasma generation near fore edge of the plate (i.e. near an area of maximal energy losses of airflow).

A scheme of electrodes fixing is shown in Fig.3.2.1.

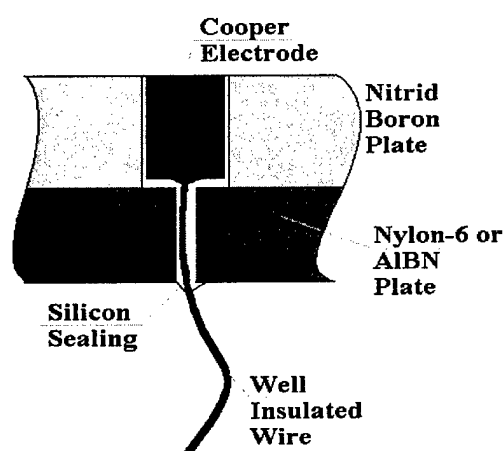


Fig.3.2.1. Scheme of the electrodes installation.

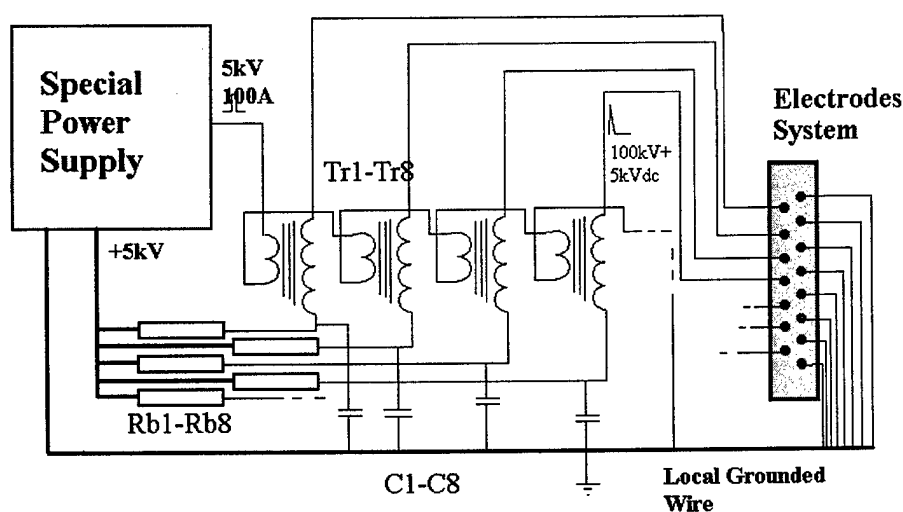


Fig.3.2.2. Principal scheme of Power Supply connection.

An original power supply with individual excitation of each electrode has been used. A principal scheme of the PS connection with the surface plasma generator is presented in Fig.3.2.2. The PC provides DC power with voltage 5kV from large electrical capacity and high current pulses with a frequency from 10Hz up to 5kHz. These pulses go on high voltage transformers, individually for each electrode. Thus all electrodes have an independent excitation of the electric discharge. Ballast resistors manage two functions: limit a discharge current and redistribute the discharge current on all electrodes more-less homogeneously.

At such kind of discharge supply it is possible to measure an input power by means of measuring of voltage on the discharge gap. The input power can be calculated in accordance with a simple formula:

$$W_{pl} = U_{pl} \times (U_{ps} - U_{pl}) / N R_b;$$

Where W_{pl} - input power to a plasma volume, U_{pl} -voltage on a plasma gap; U_{ps} -voltage of power supply; N -number of ballast resistors; R_b -resistivity of ballast. The dependence of input power on voltage of plasma gap is presented in Fig.3.2.3 for a ballast resistor $R_b=10k\Omega$. Well seen that the maximal input power is achieved at gap voltage in a half of input voltage. Two values of ballast resistor have been used at the experiment: 10k Ω and 2k Ω . So at the first case a maximal input power could be about 4kW, at

the second case- about 22kW.

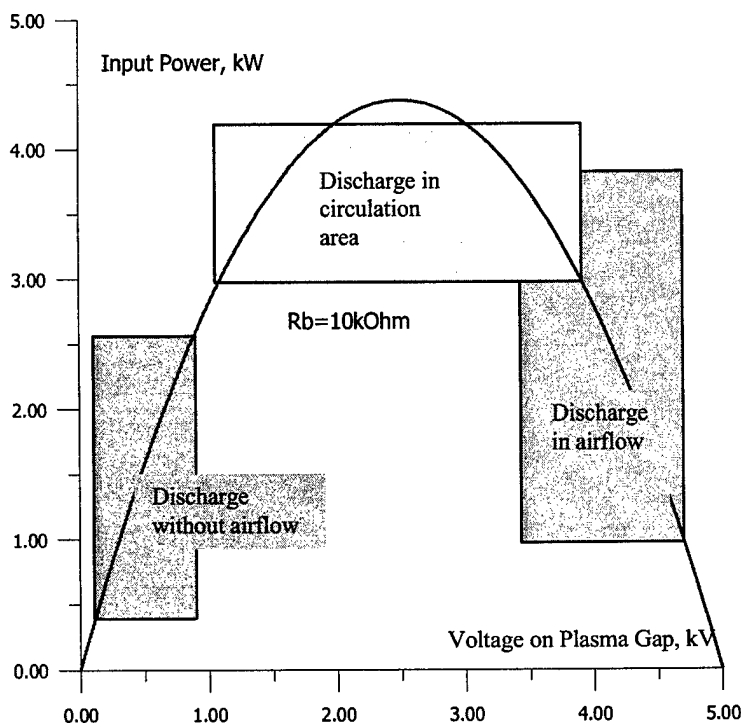


Fig.3.2.3.

Volt-Power characteristic of the discharge and areas of the discharge existing at different conditions.

$P_{st}=400-760\text{Torr}$.

It has to be noted that different conditions of the plasma excitation and burning leads to a different level of input power. Such areas are presented in Fig.3.2.3 roughly. At atmospheric condition without airflow the discharge is quickly transformed to arc-like configuration on a one or few electrodes. This form is stable and, as a rule, leads to an electrode damage. Voltage on the electrodes is not exceeded level 1kV. The discharge structure in airflow was non-homogeneous in free stream and relatively homogeneous at using artificial separation initiator. These forms are relatively stable. Gap voltage in high-speed airflow is about 3-4.5kV and 2-3kV at discharge location in a circulation zone. In a free stream a large level of wide-spectrum vibrations are appeared on a voltage record.

To avoid a large level of EM noise we were forced to disconnect of power supply from grounded parts. So only well insulated instruments could be apply for the measurements.

Following photos present main operation modes of multi-electrode surface discharge.

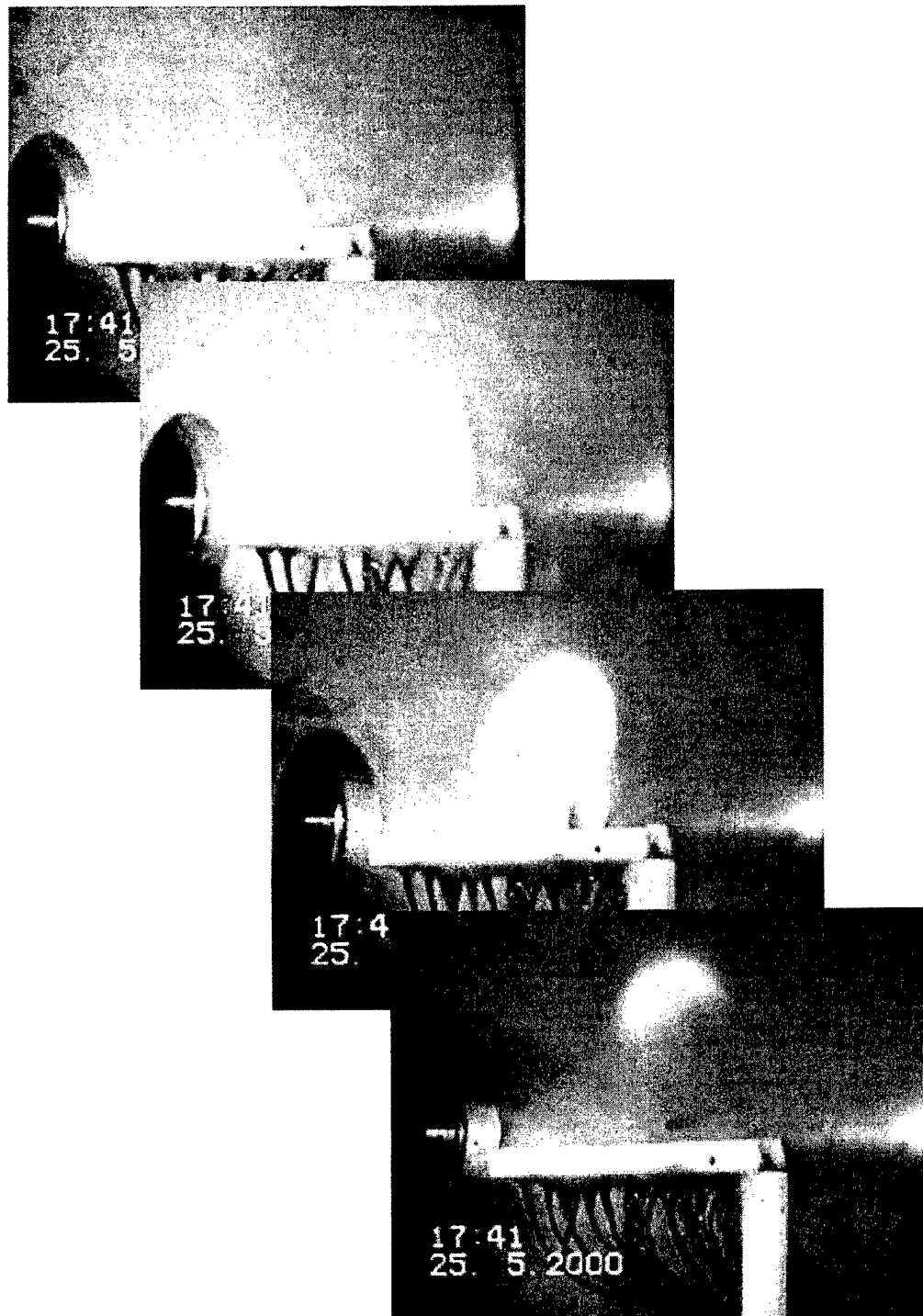
Discharge Appearance.

Several different schemes have been tested to provide a stable plasma generation on all electrodes simultaneously at relatively high pressure. Finally, the power supply with an individual discharge excitation on each electrode has been chosen. It can be characterized by the following parameters:

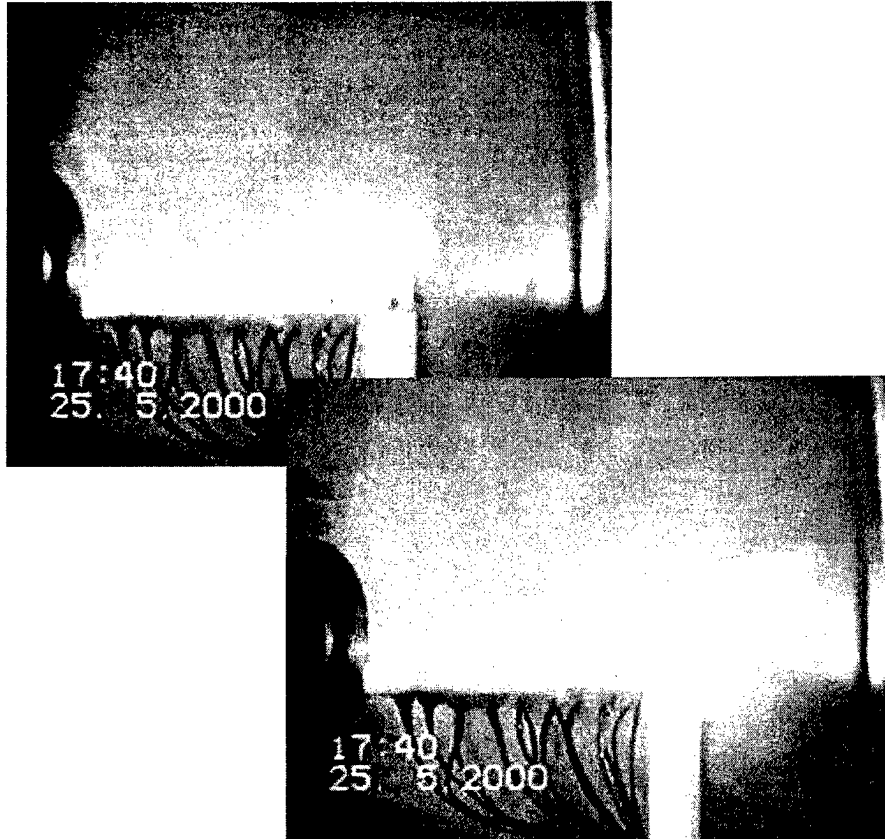
Frequency of high voltage pulses	up to 5kHz;
Initial voltage	5kV;
Breakdown voltage	not less than 50kV;
Current on each electrode	0.2-2A;
Pulse duration	0.01-5s;
Numbers of active electrodes pairs	7;
Electrode diameter	4mm;
Material of active dielectric plate	boron-nitride, Nylon-6, boron-silicate;
Operation modes	pulse-periodic, quasi-continuous.

Pulse-periodic mode (model runs).

The photos in Fig.3.2.4 present different phases of discharge evolution at Nylon-6 plate without airflow. Period of frames is 20ms.



The photos in Fig.3.2.5 present different phases of discharge evolution at Nylon-6 plate with airflow. Period of frames is 20ms.



Well seen the difference. Not all electrodes work at such condition. Erosion of the plate occurs near the electrodes and in the gaps between them. After the model experiments the material of the plate has been changed. Boron-nitride and boron-silicate are used at the all last experiments.

The photo in Fig.3.2.6 presents the surface discharge at boron-silicate plate with airflow.

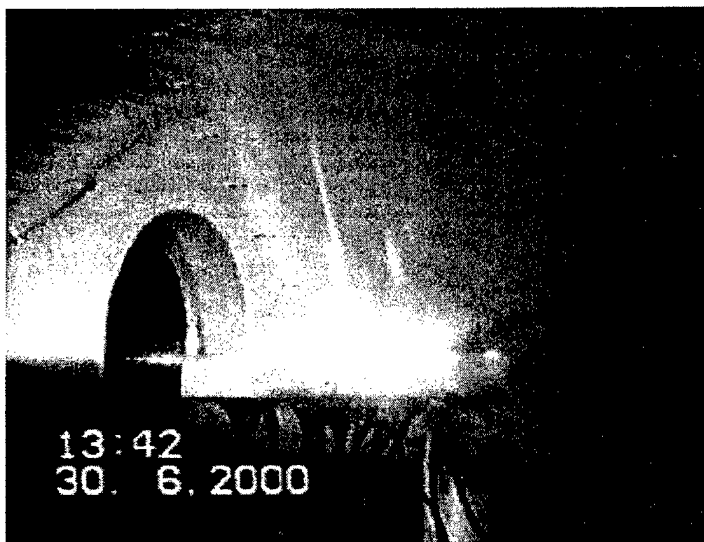


Fig.3.2.6.
Model experiments on the
discharge excitation.
B-Si plate.

In this case the scheme of separate discharge excitation through each electrode's pair has been used. Seen that discharge occupied the most part of the plate. Measurements show that 5 from 7 pair electrodes work simultaneously at each period of time.

Quasi-continuous discharge. No airflow.

The photos in Fig.3.2.7 present different phases of discharge evolution at B-N plate without airflow. Period of frames is 20ms.

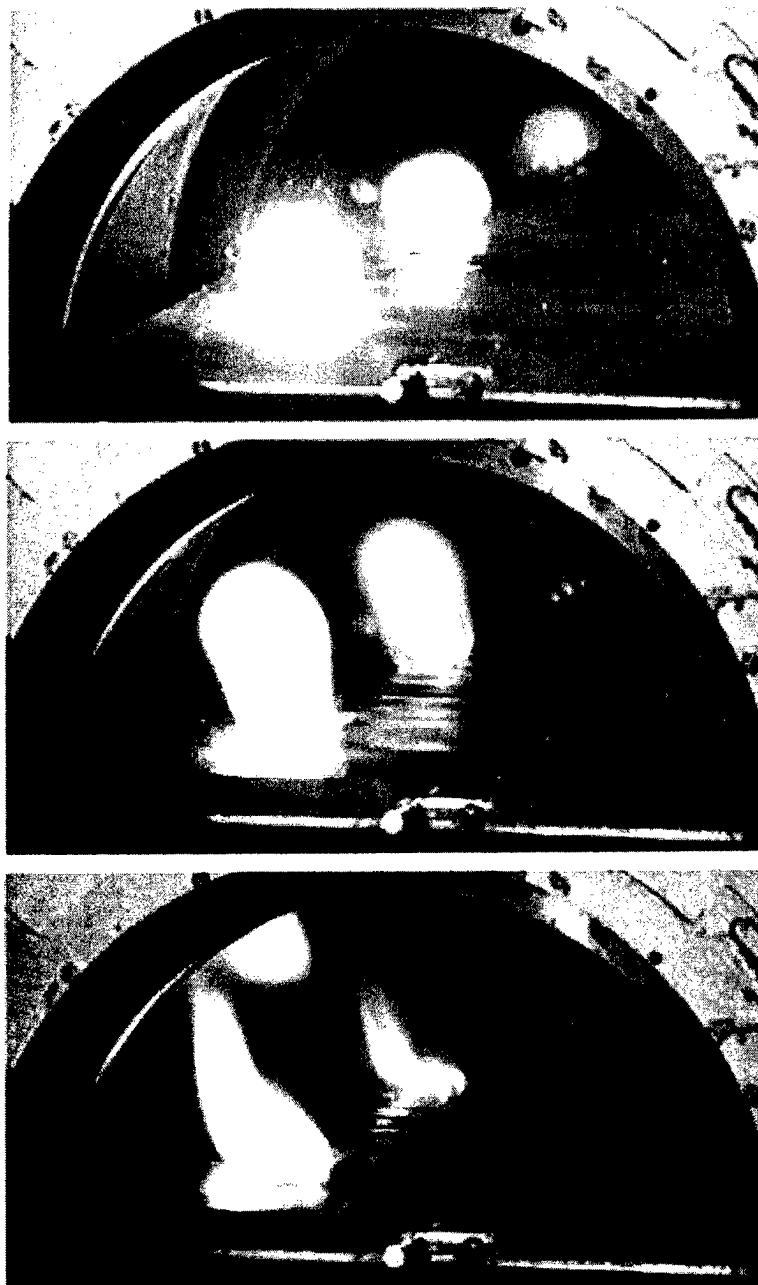
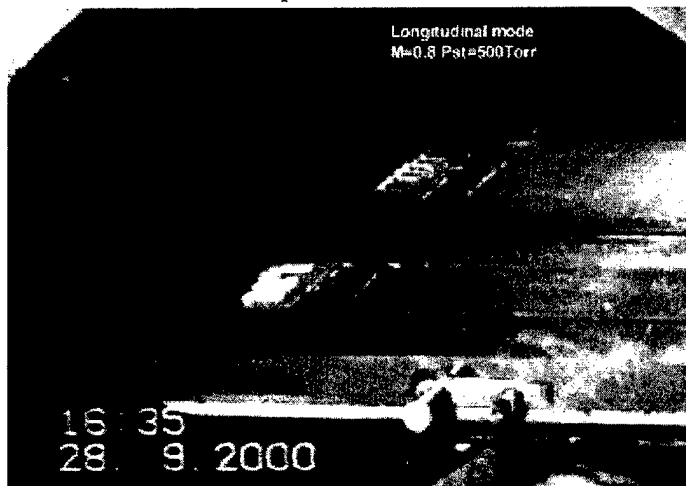


Fig.3.2.7. Sequential photos of atmospheric discharge.

Full current was about 14A at gap voltage about 1kV. A switch on was very short due to electrodes damage. Plate was made from B-N. One can see three images of the discharge. Two last images are result of reflection from glass windows. Good for details observation.

Quasi-continuous discharge. Free stream airflow.

The photos in Fig.3.2.8 present two different modes of the discharge on B-N plate at transonic airflow. Exposition is 20ms.



Longitudinal mode of transonic discharge.

$I_d=0.7-1A$, $V_d=4kV$;

$R_b=10k\Omega$

Discharge near profiled plate at subsonic airflow. $M=0.6$, $V_d=3kV$, $R_b=2k\Omega$



Transversal-longitudinal mode of transonic discharge. $M=0.8$

$I_d=1.5-2A$, $V_d=4.5kV$;

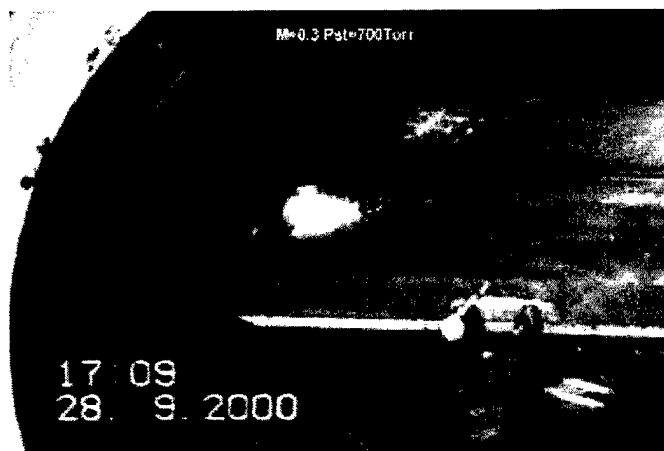
$R_b=2k\Omega$.

Fig.3.2.8. Photos of the discharge in transonic airflow. $P_{st}\approx 500Torr$.

Well seen that second and third discharges are more bright than first one. Plasma at the third discharge is penetrating longer in X direction. It was due to more power input. Switches on were about 2sec of duration. Plate was made from B-N. One can see three images of the discharge on each photo. Two last images are result of reflection from glass windows.

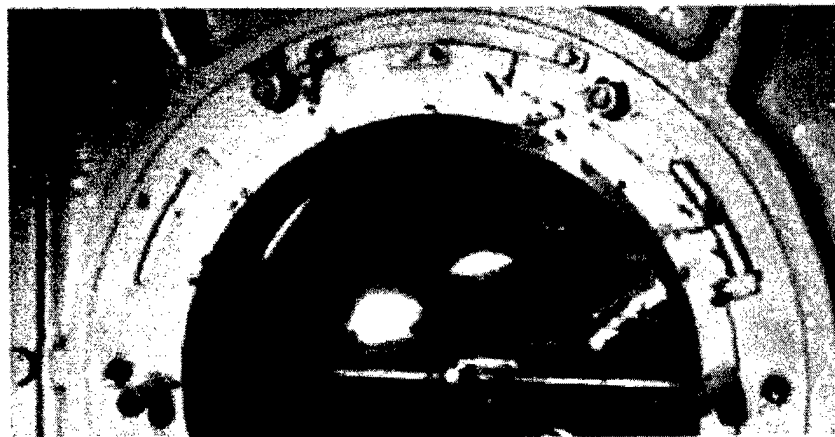
Quasi-continuous discharge. Airflow. Circulation zone.

The photos in Fig.3.2.9 present the discharge on B-N plate at subsonic airflow in a presence of circulation zone after an artificial obstacle. Exposition was 20ms.



Multi-electrode discharge in a separation zone at subsonic airflow.

$I_d=1-1.5A$, $V_d=3kV$;
 $R_b=10k\Omega$



Discharge in a separation zone at subsonic airflow.

Profiled Plate.
 $I_d=5A$,
 $V_d=3kV$,
 $R_b=2k\Omega$.

Fig.3.2.9. Photos of discharge at presence of separation zones..

Switches on were about 1sec of duration. Plate was made from B-N. One can see three images of the discharge. Two last images are result of reflection from glass windows. A circulation zone increases the input power. Each portion of gas blows through the discharge area during amore time.

3.3. Measurement System and Synchronization.

Measuring-registering instrumentation complex of ST-1 description.

At the experimental research of the plain and profiled plate aerodynamic drag reduction with the help of energy supply the measuring-registering instrumentation complex has been used. This complex consists of the following elements:

- • Pressure transducers in the ST-1 tunnel operating section (3);
- • Strain gauge balance (4);
- • 8-channel amplifier 8×10^4 (5);
- • Mirror-galvanometer oscillograph NO43.1 (6);
- • Shadow Schlieren device IAB-451 (7-10).

After a modernization the oscilloscope "Tektronix TDS-210" and computer "Toshiba-420" have been included for the digital recording of balances signal.

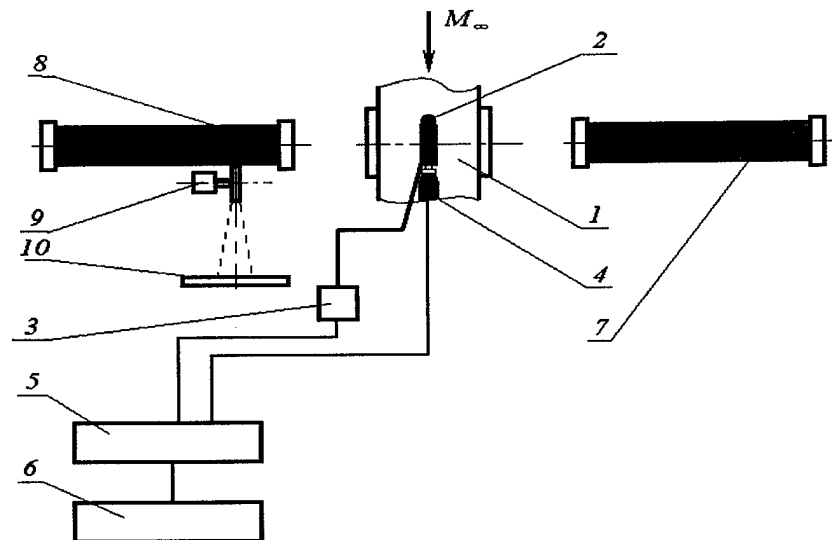


Fig.3.3.1. Layout of measuring system of ST-1.

The pressure transducers in ST-1 tunnel test section (3) are applied for the test section Mach number definition (1). The transducer signal is amplified by the low-frequency 8-channel amplifier 8×10^4 (5). Then the signal from the amplifier is transmitted to the mirror-galvanometer oscillograph (6), which in turn records the pressure variation diagram on a photo-tape.

For the aerodynamic drag measurements strain gauge balance (4) is used, the signal

from which is also transmitted to the 8 ALF amplifier and then to the mirror-galvanometer oscillograph and is recorded as the temporary diagram.

Before the experiment realization the pressure transducer and strain balance calibration is carried out for the calibration coefficients K_p and K_q are to be determined.

For the model streamlining monitoring the device IAB-451 is used, which consists of a collimator (7) and an observation tube (8). At the experiment realization the streamlining monitoring is carried out with the help of a screen (10); besides the camera (9) filming is realized. An appropriate layout is presented in Fig.3.3.1.

In the out of a wind tunnel the gauge of absolute pressure "HoneyWellTM" is established, reference of base pressure is deduced in a point of measurements of this gauge, and thus, the checking of reference of the base pressure gauge is made.

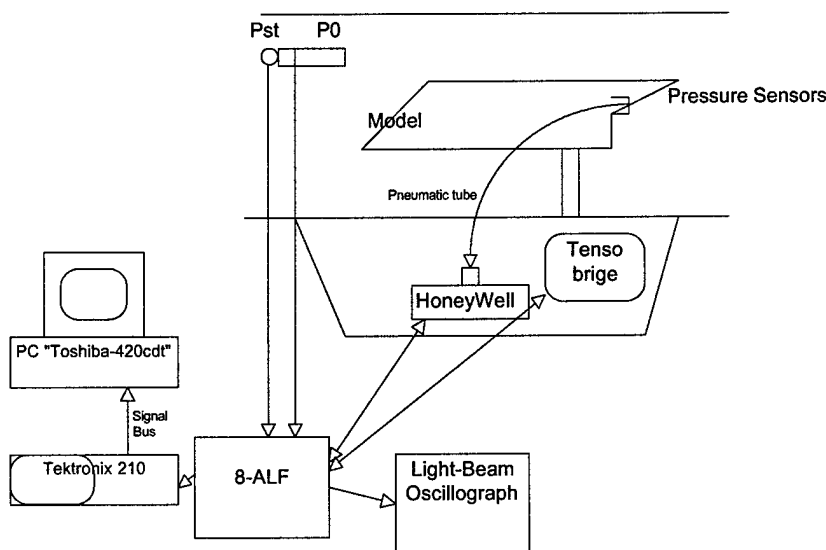


Fig.3.3.2. Principal layout of data acquisition system.

An appropriate scheme of data acquisition is presented in Fig.3.3.2. Flow control gauges P_0 and P_{st} of the "HoneyWell" differential type are used for calculations of the aerodynamic characteristics of a flow (Mach number, high-speed pressure). Their reference pressure is observed and calculated on calibration curves according to the indications of the gauge of absolute pressure "HoneyWellTM". Instead of light-beam oscilloscope the digital oscilloscope "Tektronix TDS-210" has been used to record the balances data. After this the results are recorded by PC "Toshiba" by means of PCMC port.

During processing the acquired information, all measured meanings were

transformed to absolute physical values the meanings of the characteristics of a flow and aerodynamic factor Cd and Cf were calculated.

Main expressions for the calculations are presented below:

$$q = \frac{\gamma}{2} \cdot M^2 \cdot P_{st}$$

$$V = M \cdot \sqrt{\gamma \cdot R \cdot T_{st}} \quad T_{st} = T_0 \cdot \left(\frac{1}{1 + \frac{\gamma-1}{2} \cdot M^2} \right)$$

$$M = \sqrt{\frac{2}{\gamma-1} \left[\left(\frac{P_0}{P_{st}} \right)^{\frac{\gamma-1}{\gamma}} - 1 \right]}$$

$$\frac{P_0}{P_{st}} = \left[\frac{(\gamma+1) \cdot M^2}{2 + (\gamma-1) \cdot M^2} \right]^{\frac{\gamma}{\gamma-1}} \times \left[\frac{(\gamma+1)}{2 \cdot \gamma \cdot M^2 - (\gamma-1)} \right]^{\frac{1}{\gamma-1}}$$

An observation of BL and recognition of the gas parameters inside of BL are difficult due to low thickness and small gradients of gas density. New informative methods are complex technically, as a rule [49,50]. More conventional methods give a limited information and have to be used together one with others [51].

Diagnostic part of the installation includes the following:

- Schlieren-system, allowing visualizing the flow under investigation with separation of the needed phase of a process;
- Spectral system, allowing to obtain emission spectrums of plasma;
- Pressure sensors, with the possibility to select a necessary phase of a process;
- Tenso-balances;
- Video-tape recorder;
- Thermo-tabs and thermocouples.

All this allows researching the processes of interaction of surface plasmas with AD bodies in subsonic and transonic flow.

Schlieren system has been modernized especially for this experiment. A time resolution of it is about 1ms. It can be synchronized with defined phase of plasma excitation process. Real spatial resolution is about 1mm. The Schlieren system has been

connected with a video camera. At the last runs a picture has been recorded in dynamics.

Spectroscopy of the second positive system of molecular nitrogen and CN molecular spectrum were chosen as a method of gas temperature measurements. The optical spectrums are going to be registered by means of a spectrograph MDR-23 connected with a CCD camera with spectral resolution of about 0.01nm/pixel. The device spread function is 0.12-0.15nm. So, a partially resolved molecular spectrum can be obtained in experiment. For the determination of gas temperature in a discharge the method of optical emission spectrum shape fitting is going to be adopted. The exact full spectrum of 0-0 transition of the second positive nitrogen system, including R-, P- and Q-branches (the last is very weak) is generating under the defined temperature and it is then convoluted with the spread function of the spectral device. The synthetic spectrum obtained in such a manner is then compared with the real one. It is made in a procedure of best fitting of the spectrum contour by variation of the defined temperature. In this case the special attention is paid for the best coincidence of the spectral shape at the lower rotational numbers, where the distribution over the rotational levels is known to establish at a temperature practically equal to that of the gas. The accuracy of the temperature determination by this procedure can be estimated in 50K. The spectroscopic measurements have no been provided in this series of runs.

Temperature of the surface of the model has been evaluated by using the painted thermo-tabs with a different threshold of reaction (100-150-200C). Thermocouples are planed to use at the next experiments.

Synchronization.

A time diagram of the processes at the standard run of ST-1 is shown in Fig.3.3.3.

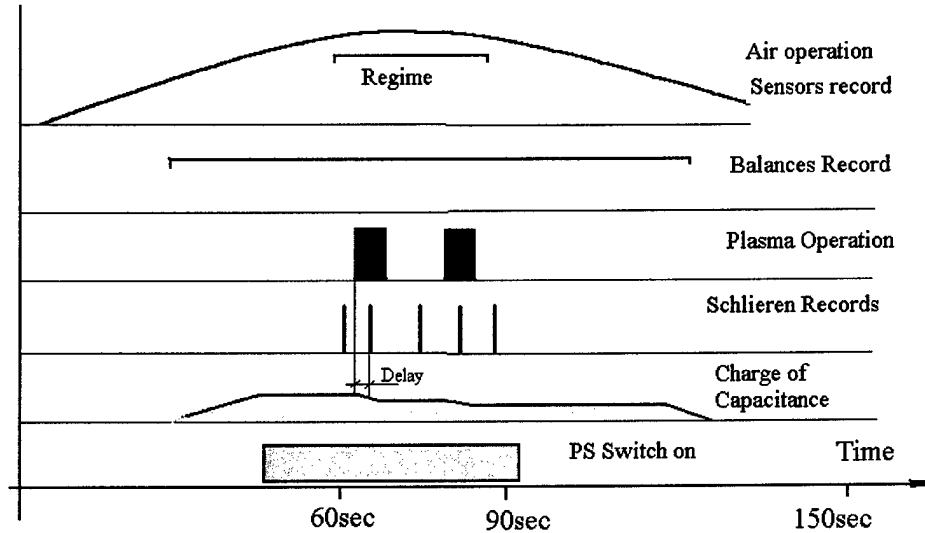


Fig.3.3.3. Time Diagram of ST-1 operation.

A process starts from opening of an air gauges for an ejector operation. When Mach number achieves a defined value, permission for systems operation is given. At this time the capacitance is charged and the PS is switched on without 5kV input. After signal "Regime" 5kV is switched on and plasma is burned during a defined time (1-2sec, as a rule). Photo-camera makes the record before, during and after each plasma excitation with a defined delay. The run duration usually is about 2.5min.

4. Experimental Results.

Four experimental sessions took place in frames of this Contract: July, 5-7; September, 27-28; October, 02; October, 04-05. The experimental results are represented in this chapter. The data have been obtained at the following conditions.

- Mach Number of airflow, M_∞ 0.99-0.3;
- Stagnation pressure, P_0 750-780Torr;
- Static pressure, P_{st} 400-700Torr;
- Stagnation temperature, T_0 ambient, 290-305K;
- Static temperature, T_{st} 250-300K;
- Reynolds number on 0.1m $(1\div 3)\times 10^6$;
- Calculated position of transition line fore and on a movable plate;
- Dimension of WT test section 250×300mm;
- Dimension of the model 250×250×45mm;
- Dimension of the movable (tested) plate plain 100×120×10mm,
profiled plate 100×120×18(7%)mm;
- Angle of attack $0\div 1^\circ$;
- Number of electrodes 17 (7 "hot" + 10 grounded);
- Ballast resistance in a circuit 10k Ω and 2k Ω per each "hot"
electrode;
- Voltage of Power Supply 5kV + 50kVpulsed;
- Main capacitance in Power Supply 4.8mF;
- Storage Energy 60kJ;
- Plasma pulse duration 2sec;
- Total electric current $1\div 15$ A;
- Input power $2\div 18$ kW.

4.1. Description of the Runs.

The most important data and results of the WT runs are represented in Table 4.1.1.

Table 4.1.1. WT Runs Description.

Date, No	Type of the model	Conditions: $P_{st}(\text{Torr})$, Ballast resistors, Flow over the plate.	Mean power Input, kW	Short Description	Mach Number, M_∞	Result
July, 6, No 1s	Plain Plate	$P_{st}=410\text{Torr}$; $R=10\text{kOhm}$; Transonic	$\sim 1.5\text{-}3\text{kW}$	Balances fault; Large noise; Two discharges on appr. 1 sec of each.	0.98	Effect on Schlieren Photo.
2s	Plain Plate	$P_{st}=550\text{Torr}$; $R=10\text{kOhm}$; Subsonic	$\sim 1.5\text{-}3\text{kW}$	Balances fault; Two discharges on appr. 1 sec of each. Electrodes damage.	0.7	???
3s	Plain Plate	$P_{st}=460\text{Torr}$; $R=10\text{kOhm}$; Transonic; Obstacle before discharge area.	$\sim 1.5\text{-}3\text{kW}$	Balances fault; Two discharges on appr. 1 sec of each.	0.92	Effect on Schlieren Photo.
4s	Plain Plate	$P_{st}=470\text{Torr}$; $R=10\text{kOhm}$; Transonic; Obstacle before discharge area.	$\sim 1.5\text{-}3\text{kW}$	Balances fault; Two discharges on appr. 1 sec of each.	0.9	Effect on Schlieren Photo.
5s	Plain Plate	$P_{st}=490\text{Torr}$; $R=10\text{kOhm}$; Transonic; Obstacle before discharge area.	$\sim 1.5\text{-}3\text{kW}$	Balances fault; Two discharges on appr. 1 sec of each. Distuning of Schlieren device.	0.85	???

September, 28, No 1	Plain Plate	$P_{st}=425\text{Torr}$; $R=10\text{kOhm}$, Transonic	2-3kW	EM noise on balances. Two discharges on appr. 1 sec of each.	0.97	Noise.
2	Plain Plate	$P_{st}=510\text{Torr}$; $R=10\text{kOhm}$ Transonic	2-3kW	EM noise on balances. Two discharges on appr. 1 sec of each.	0.80	Noise.
3	Plain Plate	$P_{st}=600\text{Torr}$; $R=10\text{kOhm}$ Subsonic	2-3kW	EM noise on balances. Two discharges on appr. 1 sec of each.	0.6	Noise.
4	Plain Plate	$P_{st}=555\text{Torr}$; $R=10\text{kOhm}$ Subsonic	2-3kW	One discharge.	0.7	Balances Effect
5	Plain Plate	$P_{st}=600\text{Torr}$; $R=10\text{kOhm}$, Subsonic, Artificial obstacle on moving plate	2-3kW	One discharge	0.6	No balances effect
6	Plain Plate	$P_{st}=625\text{Torr}$; $R=10\text{kOhm}$ Subsonic, Artificial obstacle on moving plate	2kW	Two discharges	0.55	No balances effect
7	Plain Plate	$P_{st}=685\text{Torr}$; $R=10\text{kOhm}$ Subsonic. Obstacle before discharge area.	4-4.5kW	Balances fault	0.4	Visible effect on Schlieren Photos
			Wpl		M_∞	
October, 2, No 01	Plain Plate	$P_{st}=418\text{Torr}$; $R=10\text{kOhm}$ Transonic, Artificial obstacle before discharge area.	2-4kW	Balances fault	0.97	Visible effect on Schlieren Photos
02	Plain Plate	$P_{st}=625\text{Torr}$; $R=10\text{kOhm}$ Subsonic, Artificial obstacle before discharge area.	4-4.5kW	Discharge fault	0.55	No Discharge
03	Plain Plate	$P_{st}=645\text{Torr}$; $R=10\text{kOhm}$ Subsonic	No discharge	Discharge fault	0.5	No discharge

				W/pl		Fault	M_∞	
October, 5, No11	Plain Plate	$P_{st}=410\text{Torr}$; $R=10\text{kOhm}$ Transonic		No discharge		Fault	0.98	No discharge
12	Plain Plate	$P_{st}=420\text{Torr}$; $R=10\text{kOhm}$ Transonic		2-3kW		2 discharges, about 1sec, surface longitudinal discharge,	0.95	Effect
13	Plain Plate	$P_{st}=450\text{Torr}$; $R=2\text{kOhm}$; Transonic		2-3kW		Fault	0.9	No discharges
14	Plain Plate	$P_{st}=510\text{Torr}$; $R=2\text{kOhm}$ Transonic (small area, unsteady)		3-6kW		Discharges 0.5sec, 0.2sec 0.5sec, surface longitudinal mode. Shock Wave locates near fore edge of the plate. Discharge locates just after straight shock.	0.8	Unsteady operation mode, No effect on balances, 20% amplitude of vibrations.
15	Profiled Plate	$P_{st}=530\text{Torr}$; $R=2\text{kOhm}$; Subsonic		6kW		2 discharges, First is 0.5sec, second one is weak.	0.75	Balances Effect; Effect in Schlieren photo.
16	Profiled Plate	$P_{st}=605\text{Torr}$; $R=2\text{kOhm}$; Subsonic		8kW		1 Discharge, 1+0.5sec, unsteady	0.6	Two polar balances effect. Effect in Schlieren Photo.
17	Profiled Plate	$P_{st}=625\text{Torr}$; $R=2\text{kOhm}$; Artificial Separation Zone, Subsonic		15kW		1 Discharge, 0.5sec stable. Schlieren fault.	0.56	Balances Effect.
18	Profiled Plate	$P_{st}=660\text{Torr}$; $R=2\text{kOhm}$; Artificial Separation Zone, Subsonic		12kW		1 Discharge 1sec stable	0.45	Balances Effect of drag reduction; Effect in Schlieren photo.

4.2. Balances Measurements.

Transonic runs at free stream. Plain plate.

There were 6 runs at these conditions. The balances effect is definitely exist but unstable. In can be related to unstable position of a main shock above the plate (see 5.3.). The balance record of the run 12 (see table 4.1.1) is presented in Fig.4.2.1. Seen that a plasma effect occurs not just after switching on (sharp pike can be related to a EM noise at the relay operation). A signal trend is not a constant due to change of airflow parameters and high sensitivity of a main shock to them.

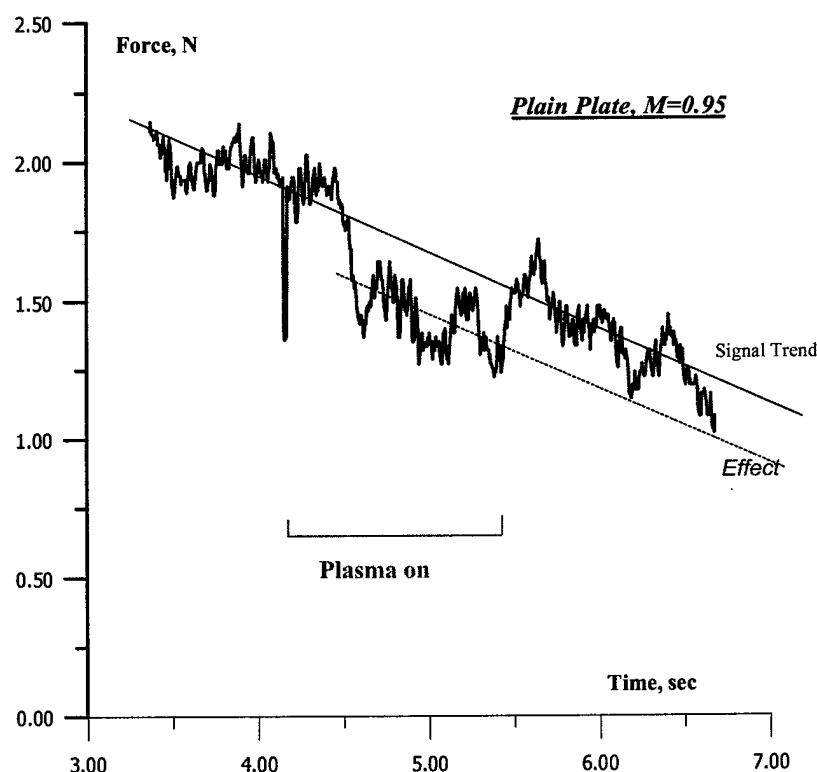


Fig.4.2.1. Balance record of Run No12. Transonic mode.

Seen that the value of a friction reduction is about 0.2N or 10% of a friction force.

Subsonic runs at free stream. Plain plate.

There were 4 runs at these conditions. The balance effect is definitely existing. Sometimes a two-polar plasma effect can be noted. The balance record of the run 4 (see table 4.1.1) is presented in Fig.4.2.2. This record was made by light-beam oscillograph. Here is a fragment. A force signal polarity is negative. A signal trend is not a constant due to change of airflow parameters.

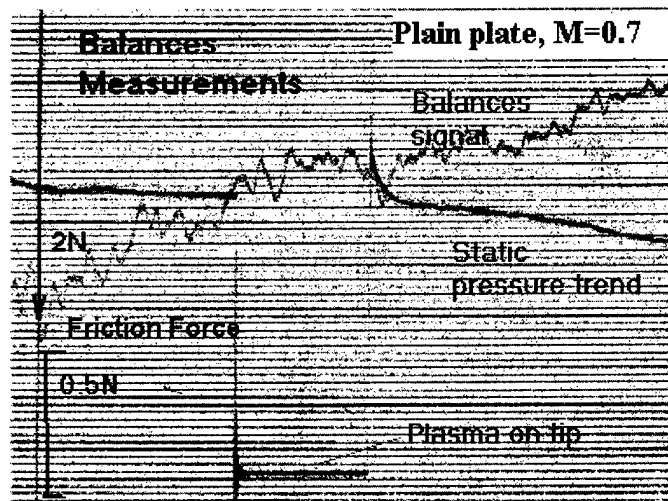


Fig. 4.2.2.
Balance record of Run No4.
Subsonic mode.

Seen that the value of a friction reduction is 0.1-0.2N or less than 10% of friction force.

Subsonic runs at free stream. Profiled plate.

There were 2 runs at these conditions. The balance effect is definitely existing. Sometimes a two-polar plasma effect can be obtained. The balance record of the run 15 (see table 4.1.1) is presented in Fig.4.2.3. This record was made by light-beam oscillograph. Here is a fragment. A force signal polarity is positive. The balance record of the run 16 (see table 4.1.1) is presented in Fig.4.2.4. A signal trend is not a constant due to change of airflow parameters.

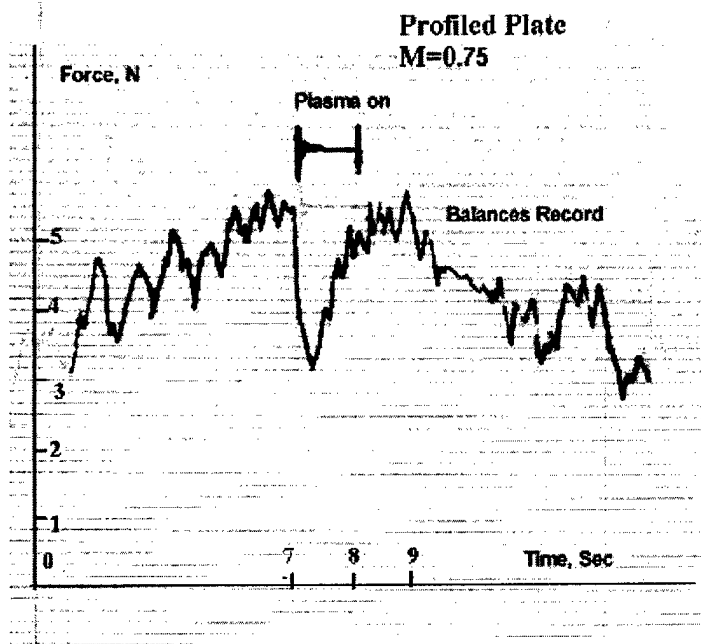


Fig. 4.2.3.
Balance record of Run
No15.
Subsonic mode.

Well seen that value of a tangential force is decreasing. It happens due to plasma influence. A signal curve has a specific shape with relaxation fronts. It is a circumstantial evidence of a thermal nature of the effect in this case.

The value of friction drag reduction was about 2N or about 40% of an initial level of the force.

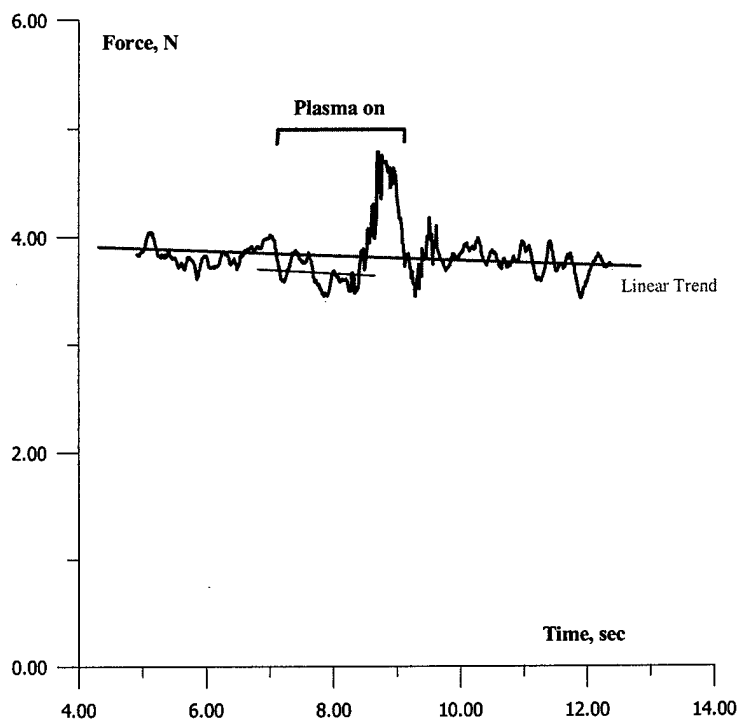


Fig. 4.2.4.
Balance record of Run
No16. Subsonic mode.

In this case a two-polar change of signal is observed. If the force reduction is about 0.2N at the first part of the pulse, the force increases in about 1N. Discharge operation in this case was unstable. We can suggest that an unstable separation processes occur in this run (see item 5.3.).

Subsonic runs at artificial separation zone. Profiled plate.

There were 2 runs at these conditions. The balance effect is definitely existing. Sometimes a two-polar plasma effect can be obtained. The balance record of the run 17 (see table 4.1.1) is presented in Fig.4.2.5. This record was made by light-beam oscillograph. Here is a fragment. A force signal polarity is positive. The balance record of the run 18 (see table 4.1.1) is presented in Fig.4.2.6. A signal trend is not a constant due to change of airflow parameters.

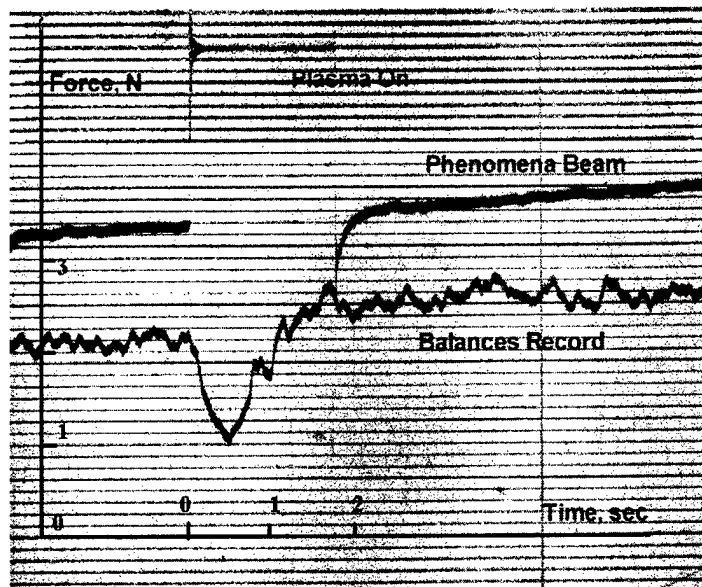


Fig. 4.2.5.
Balance record of Run
No17.
Profiled plate.
Subsonic mode.
Artificial obstacle.

Well seen that value of a tangential force is decreasing significant. It happens due to plasma influence. A signal curve has a specific shape with relaxation fronts. It is a circumstantial evidence of a thermal nature of the effect in this case. The time of plasma switching on was about 2sec and the electric power input was large because of discharge location in a separation zone. Large current leads to fast discharging of a capacitance. So the voltage in power supply is drop. As a result the plasma was stable only the first 0.5sec. An appropriate signal behavior one can see in the balance record.

The value of friction drag reduction was about 1N or about 50% of an initial level of the force.

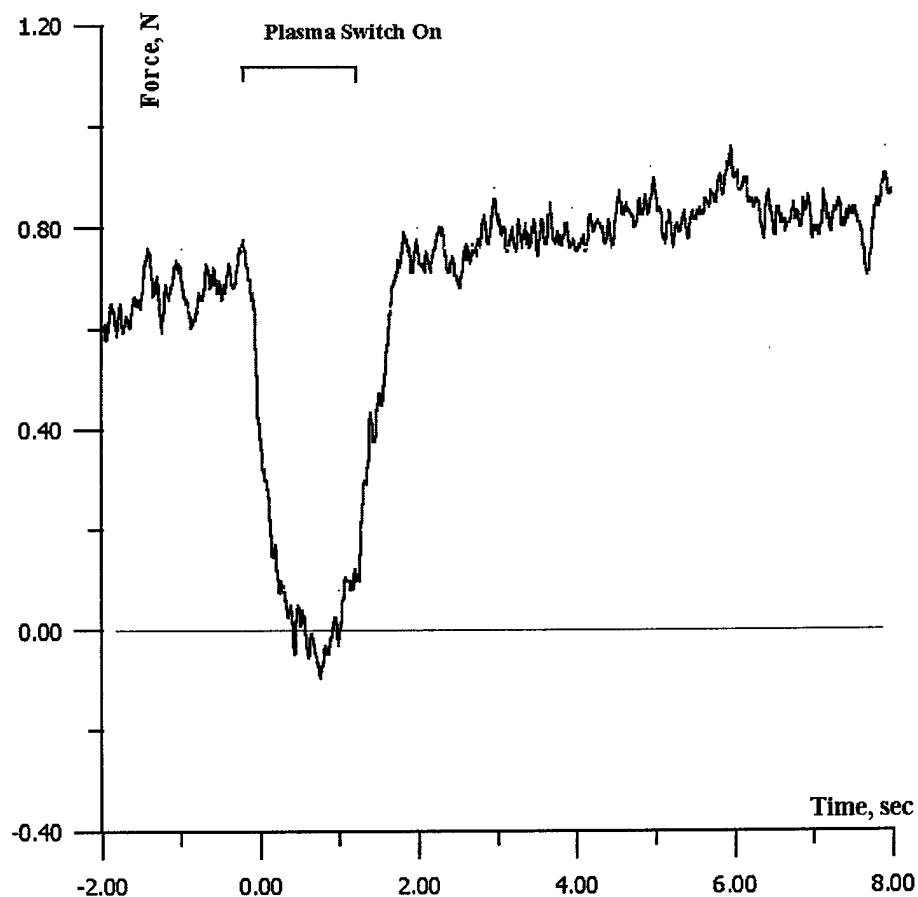


Fig. 4.2.6. Balance record of Run No18. Profiled plate.

Subsonic mode. Artificial obstacle.

The value of a tangential force is decreasing dramatically. It occurs due to plasma influence. In this case the input power to the discharge was a little bit less than in previous run (the pressure was larger). The value of friction drag reduction was about 100% of an initial level of the force. Such behavior is not contradicted to gasdynamic laws. Very probably that in this case a separation zone is swelled up and the pressure in a fore part of the profiled model can be less than in a base part.

4.3. Visualization of the Interaction.

The visualization was provided by means of video-tape camera and by Schlieren device. Here only the most interested runs are shown. Numbers of runs correspond to numbers in Table 4.1.1. Exposure was about 2ms.

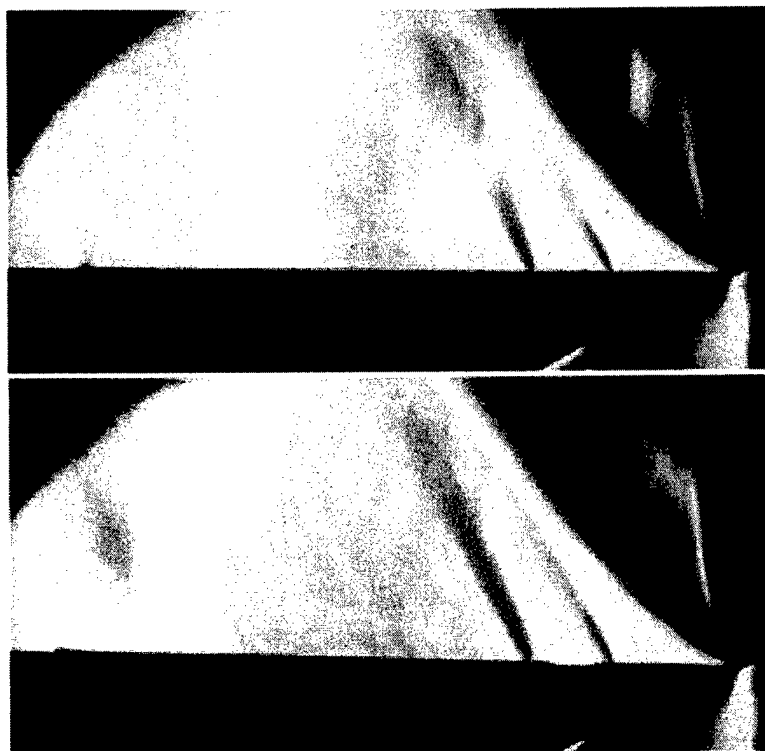
Schlieren photos very often not give a clear picture of change of a density distribution. Some methods of the picture's processing allow us to extract needed details. Modern powerful graphic editors give possibility to do it relatively easy. We are using a methods of a gradiental analysis GA and a nonlinear gradiental analysis NGA (psychedelic).

The explanation of picture's structure are presented in item 5.3 of this Report.

Transonic runs at free stream. Plain plate.

Discharge photos are presented in Fig.3.2.8.

Sample of Schlieren photo without discharge and at plasma operation are presented in Fig.4.3.1a,b accordingly.



a.

Fig.4.3.1.
Schlieren photos
without plasma (a)
and with plasma (b).
Run No1s.

b.

The main difference in the pictures is a change of position of the main shock above the plate.

These changes are visible more clearly after the image processing. Results of the processing are presented in Fig.4.3.2a,b accordingly.

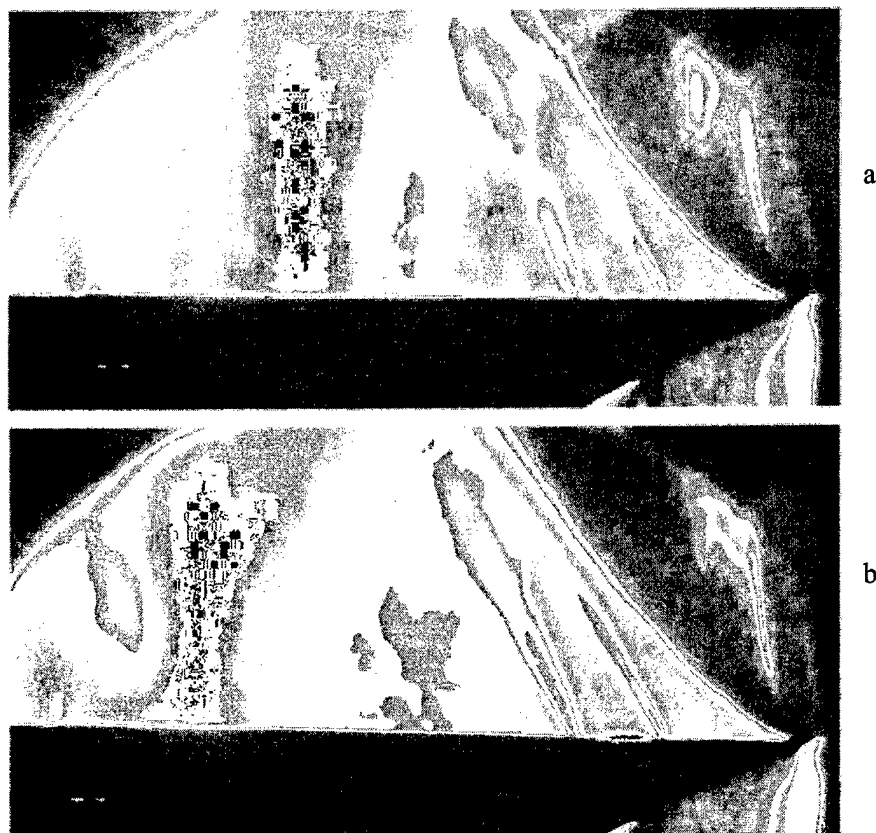


Fig.4.3.2. Run No1s

Processed Schlieren photos without plasma (a) and with plasma (b).

At low transonic mode it is visible that plasma operation leads to an earlier turbulization of flow. The turbulization primary is occurred due to BL interaction with a direct shock. The sample of such behavior is presented in Fig.4.3.3.

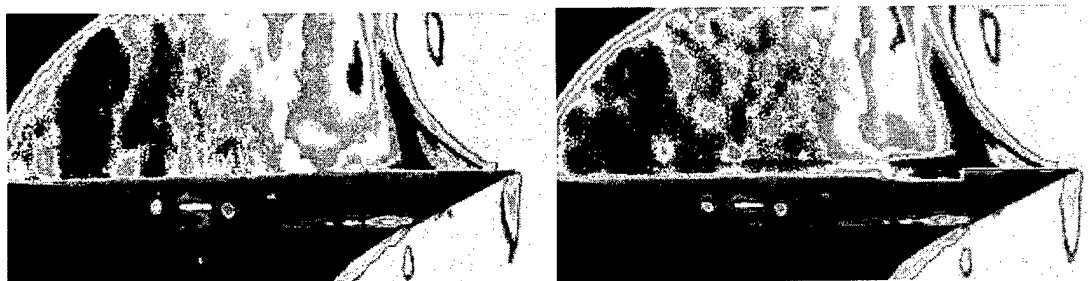


Fig.4.3.3. Run No14

Processed Schlieren photos without plasma (a) and with plasma (b).

Transonic runs at artificial separation zone. Plain plate.

Sample of Schlieren photo without discharge and at plasma operation are presented in Fig.4.3.4a,b accordingly.

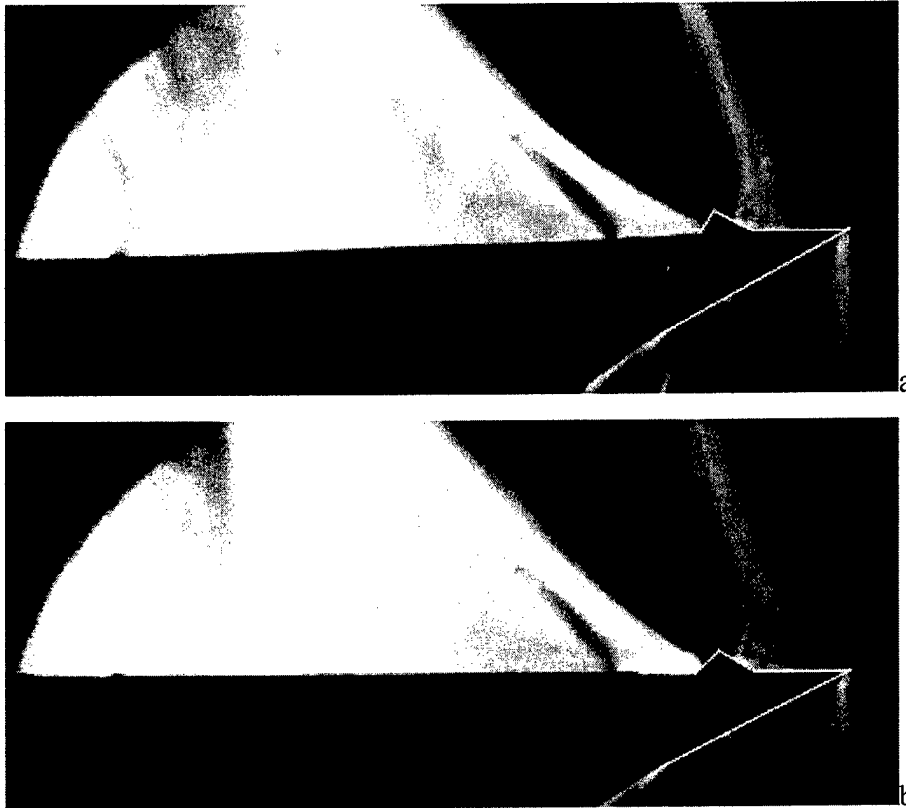


Fig.4.3.4.

Schlieren photos without plasma (a) and with plasma (b).

Run No01.

The main difference in the pictures is a change of position and the splitting of the main shock above the plate. The splitting is a visible result of a shock shifting downflow.

These changes are visible more clearly after the image processing. Results of the processing are presented in Fig.4.3.5a,b accordingly.

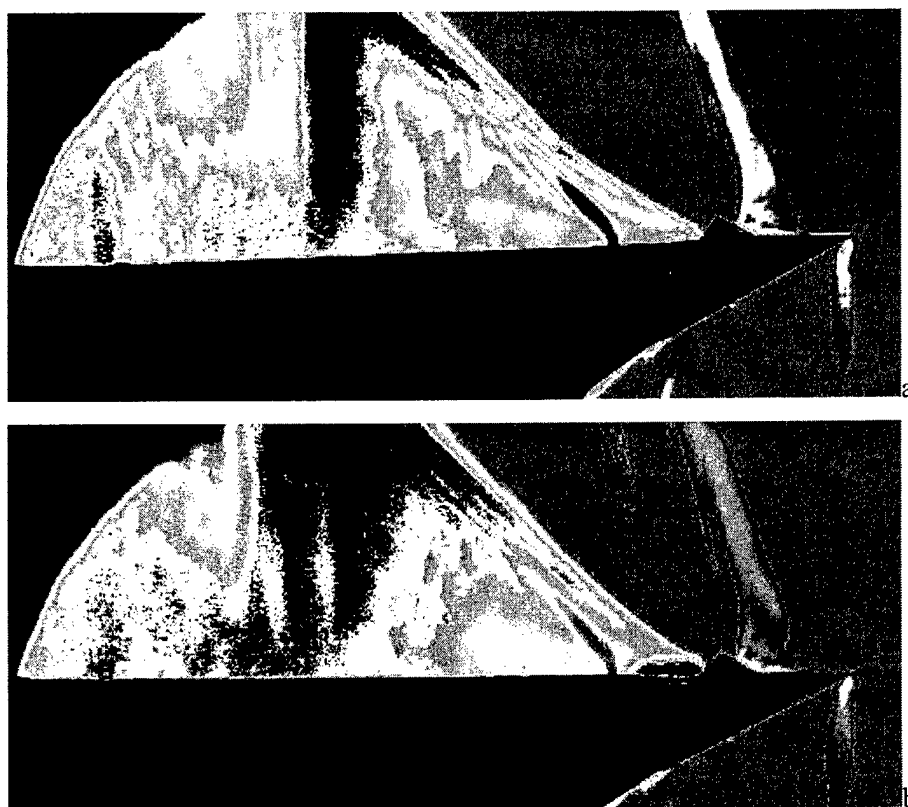


Fig.4.3.5.

Processed Schlieren photos without plasma (a) and with plasma (b).

Run No01.

Well seen that a disturbances downflow the plasma are more weak.

Subsonic runs at free stream. Plain plate.

Sample of Schlieren photo without discharge and at plasma operation are presented in Fig.4.3.6a,b accordingly.

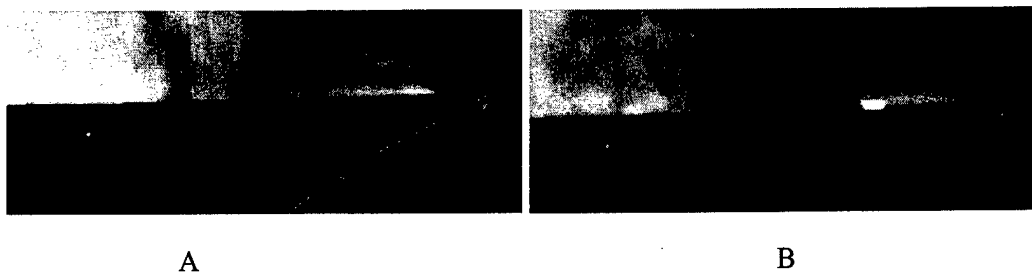


Fig.4.3.6. Run No3.

Schlieren photos without plasma (a) and with plasma (b).

These changes are visible more clearly after the image processing. Results of the processing are presented in Fig.4.3.7a,b accordingly.

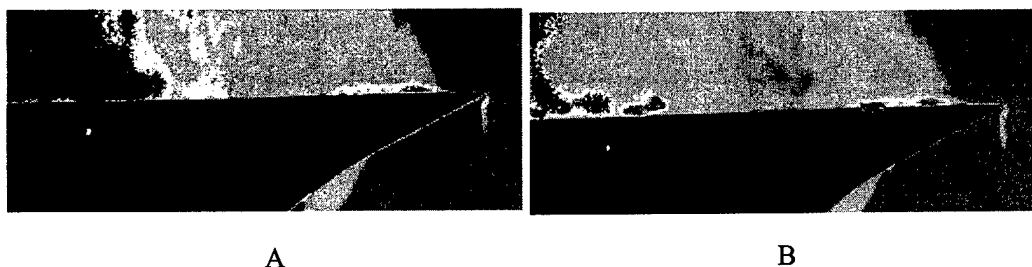


Fig.4.3.7. Run No3.

Processed Schlieren photos without plasma (a) and with plasma (b).

The main difference in the pictures is a change of position of the turbulent transition above the plate. This effect is in a contradiction with the data for a weak transonic mode but it is not chance. As illustration another processed Schlieren photos are presented in Fig.4.3.8 without plasma (A) and with it (B).

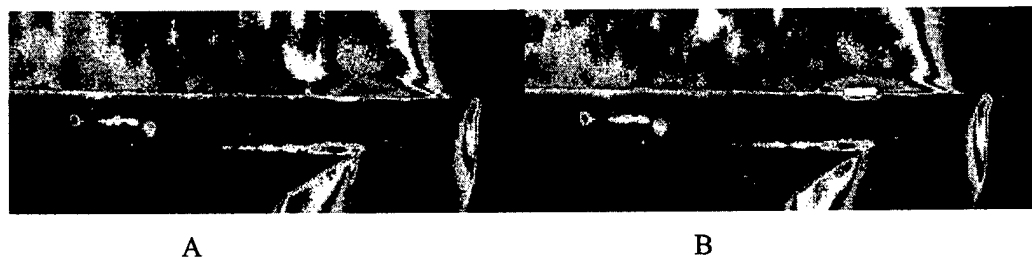


Fig.4.3.8. Run No4.

Processed Schlieren photos without plasma (a) and with plasma (b).

Subsonic runs at artificial separation zone. Plain plate.

The photos of discharge appearance are presented in Fig.3.2.9.

Sample of Schlieren photo at plasma operation is presented in Fig.4.3.9. Unfortunately we have no a reference Schlieren photo without discharge. Results of the processing are presented in Fig.4.3.10.

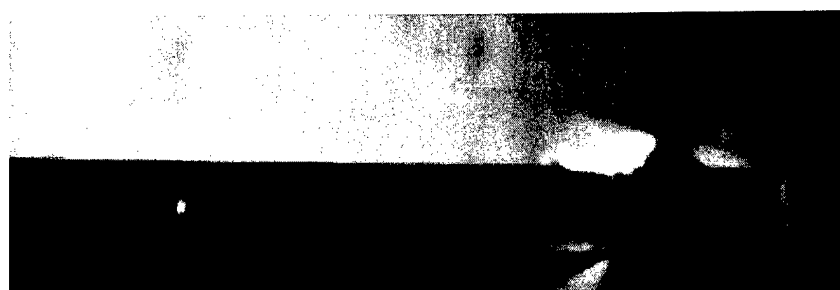


Fig.4.3.9. Run No7. Schlieren photo with plasma.



Fig.4.3.10. Run No7. Processed Schlieren photo with plasma.

The thermal plasma layer is well seen after the processing.

Subsonic runs at free stream. Profiled plate.

The photos of discharge appearance are presented in Fig.3.2.9.

Sample of Schlieren photo without discharge and at plasma operation are presented in Fig.4.3.11a,b accordingly.

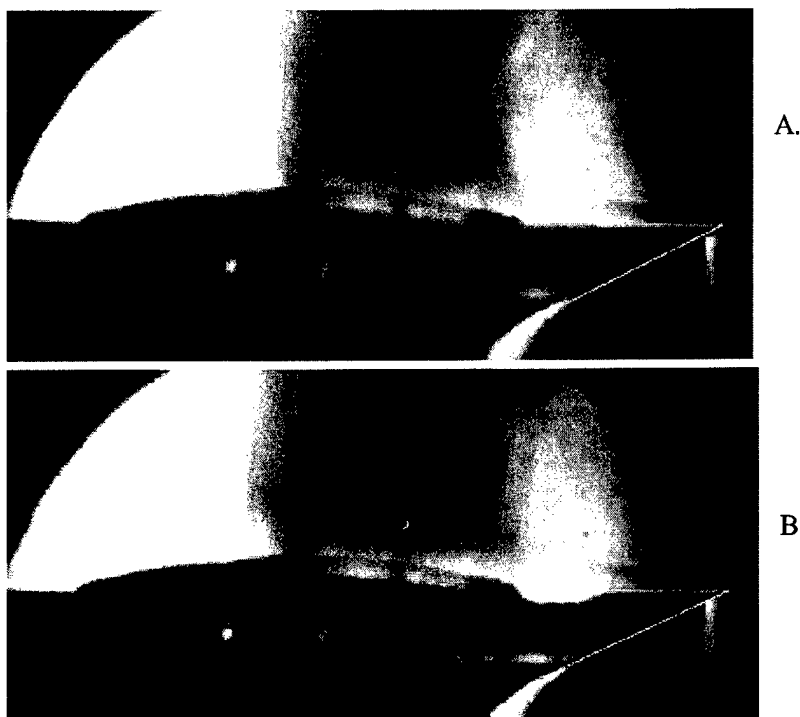


Fig.4.3.11. Run No4.

Schlieren photos without plasma (A) and with plasma (B).

These changes are visible more clearly after the image processing. Results of the processing are presented in Fig.4.3.12a,b accordingly.

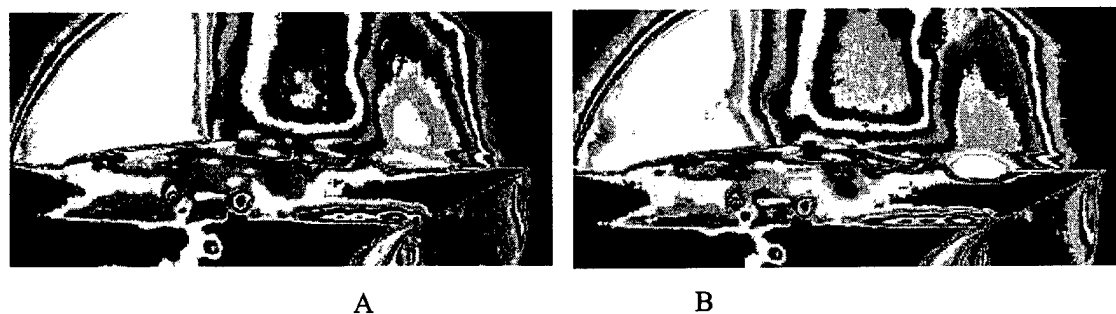


Fig.4.3.12. Run No15.

Processed Schlieren photos without plasma (A) and with plasma (B).

The area of high pressure in a back side on the model is less at plasma operation.

Subsonic runs at artificial separation zone. Profiled plate.

Sample of Schlieren photo without discharge and at plasma operation are presented in Fig.4.3.13a,b accordingly.

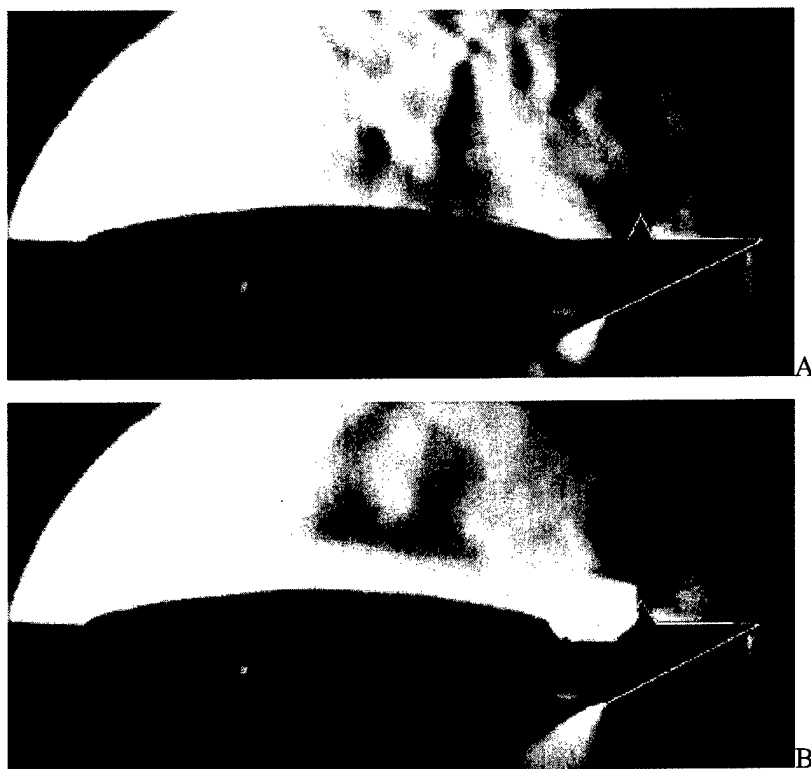


Fig.4.3.13. Run No18.

Schlieren photos without plasma (A) and with plasma (B).

Results of the image processing are presented in Fig.4.3.14a,b accordingly.

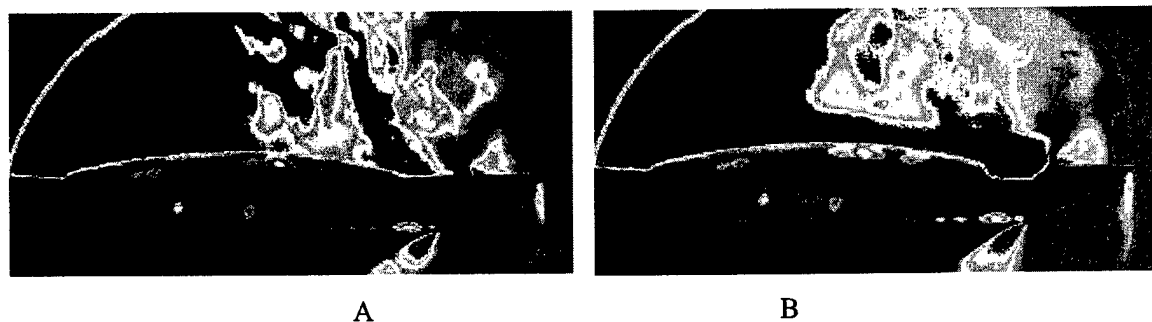


Fig.4.3.14. Run No18.

Processed Schlieren photos without plasma (A) and with plasma (B).

Well seen that the structure of airflow has been changed dramatically (see item 5.3).

4.4. Measurements of Input Power.

Measurements of the input power have been made by means of well insulated volt-meter. The results have been verified at model experiments.

The methodic and the main data is presented in item 3.2. and Table 4.1.1.

4.5. Surface Temperature.

The maximal surface temperature has been evaluated by means of painted thermotabs. The edge of a movable plate had a traces and small nidus of erosion. The results can be summarized by a chart, which is presented in Fig.4.5.1. The curve has been obtained for a subsonic operation mode at input power 10-15kW. Co-ordinate $X=0$ is a fore-edge of the movable plate.

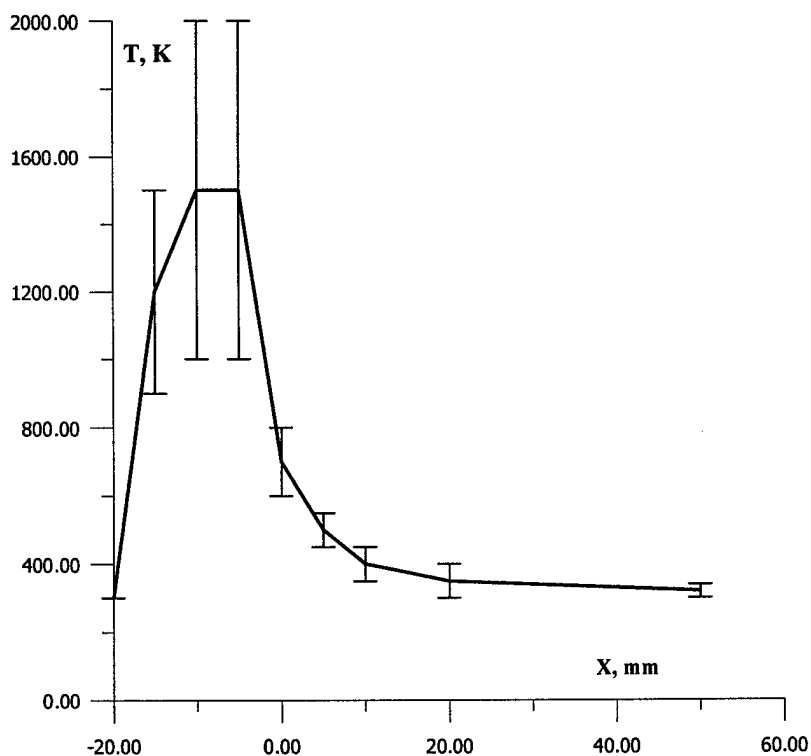


Fig.4.5.1.
Evaluation of a
maximal wall
temperature.

5. Simulation and Analysis.

5.1. Simulation in frames of laminar boundary layer model.

Express-analysis has been carried out to see the effect of plasma discharge in front of the test plate on the wall friction. Two flow fields have been computed in two-dimensional approximation, with and without discharge. For simplicity, laminar flow over the flat plate was considered. In both cases, the total pressure of 1bar and total temperature of 300 K were specified as inlet boundary conditions. The inflow boundary was set 50 mm left of the test plate. Static pressure of 0.6bar was specified at the outflow station. No-slip condition was assumed on the adiabatic wall (flat plate), and all the flow variables were interpolated from interior on the upper boundary. The discharge was simulated by specifying the energy-source distribution in the rectangular region of 10 mm in length (along the flow). Within the region energy-source intensity was assumed to exponentially drop from the wall with the characteristic decay length of 1 mm. The energy-source distribution was normalized so that the total input was 28 kW per 1 m of depth (2kW in real device).

Rectangular computational grid 177*33 was selected to solve these problems. Uniform mesh spacing was taken in flow direction and highly stretched grid was used near the wall, so that the nearest-to-wall grid point was located at 0.03 mm from the wall. The Navier-Stokes solver applied in calculations, makes use of exact solution of Riemann problem while calculating the inviscid fluxes (Godunov' method) and average-gradient approach was used in calculating the viscous fluxes. First-order Euler time-stepping was used to advance solution toward the steady-state.

Some preliminary results for the plain plate in a free stream can be seen in Figures 5.1.1÷5.1.6.

Mach number fields (filled-contours) and velocity-vectors at several stations are presented in Fig.5.1.1 (no-discharge case) and Fig.5.1.2 (plasma switch on). Temperature field for the discharge-case is shown in Fig.5.1.3.

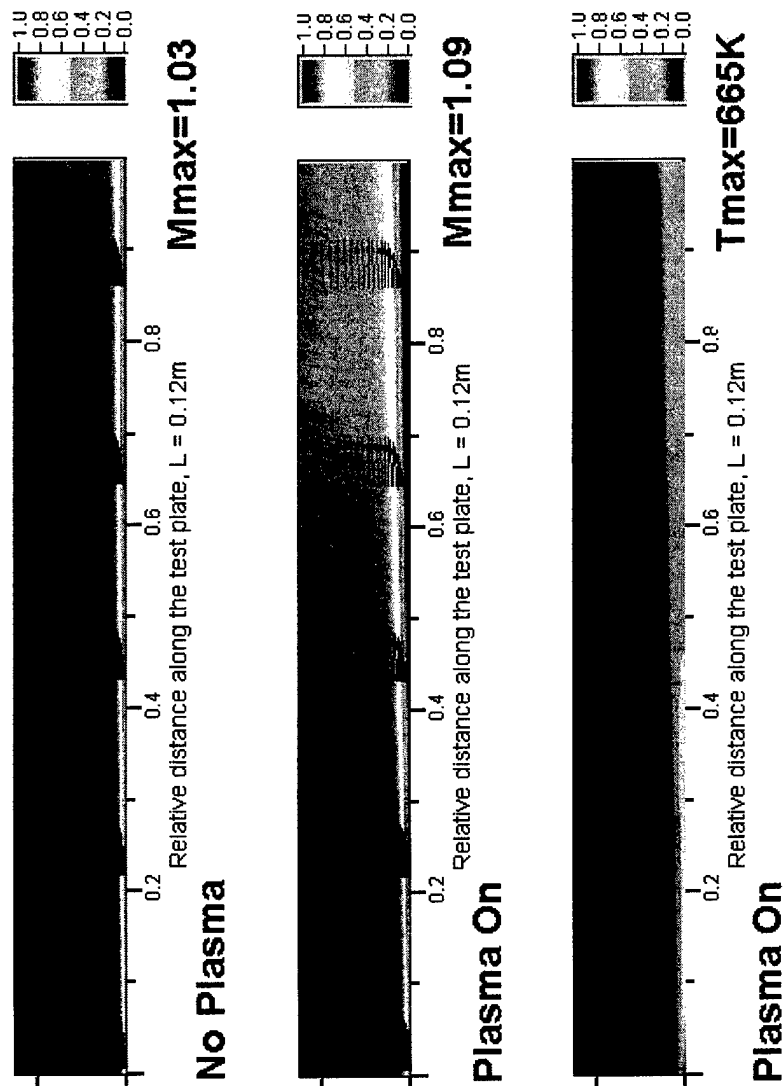


Fig.5.1.1

Fig.5.1.2.

Fig.5.1.3.

Fig.5.1.1. Mach number distribution (max=1.03) and velocity-vectors over the test plate without discharge.

Fig.5.1.2. Mach number distribution (max=1.09) and velocity-vectors over the test plate with discharge.

Fig.5.1.3. Temperature distribution (max=665K) over the test plate with discharge. Co-ordinate X=0 is on the edge of the movable plate.

Seen that the boundary layer at the plasma influence is much thicker. The detail results on profiles of Mach number and static temperature in boundary layer are presented

in Fig.5.1.4 and Fig.5.1.5: Mach number and temperature profiles on perpendicular to plate direction Y. Co-ordinate $X=0$ is related to the edge of the movable plate.

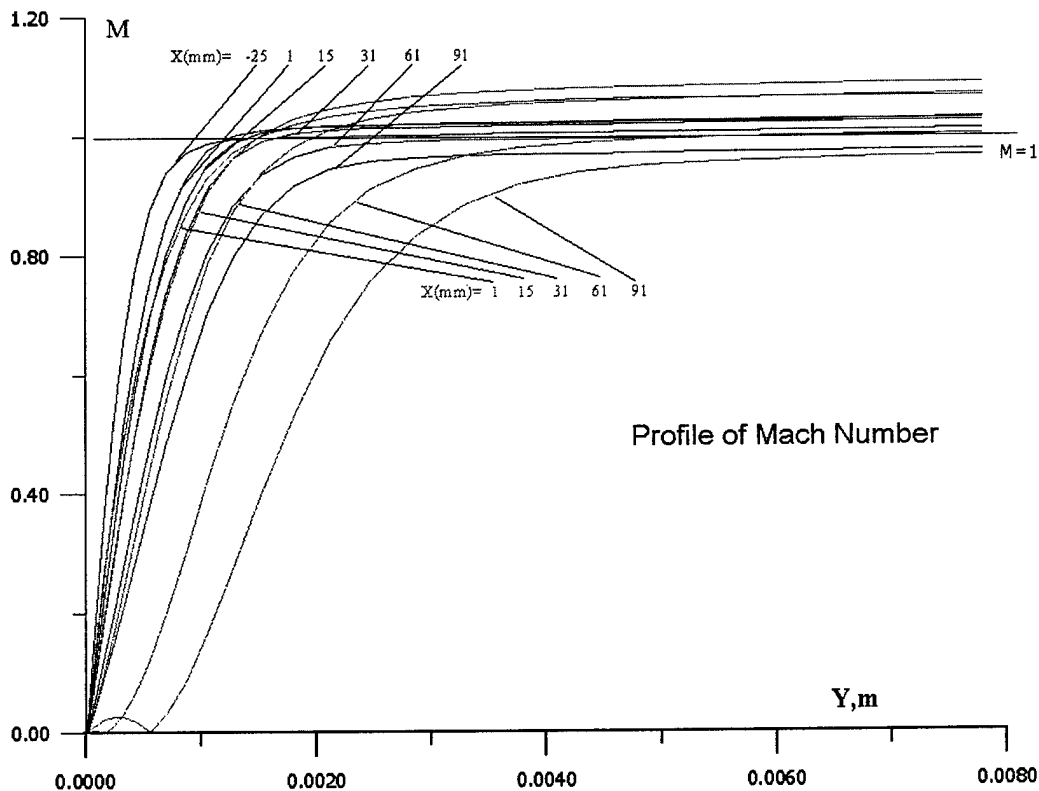


Fig.5.1.4. Mach number profiles in a boundary layer.

Blue lines are corresponded to run without plasma and red lines are corresponded to run with energy input. Well seen that in case of plasma the profiles are smoother. The calculation corresponds with a transonic operation mode. Mach number $M=1$ is achieved in both cases and approximately in the same cross-sections. But at plasma appearance such calculations give a separation zone near the wall. Physically it is not correct. It means that actually a turbulization of boundary layer take place, at least, in the second case (earlier than without plasma).

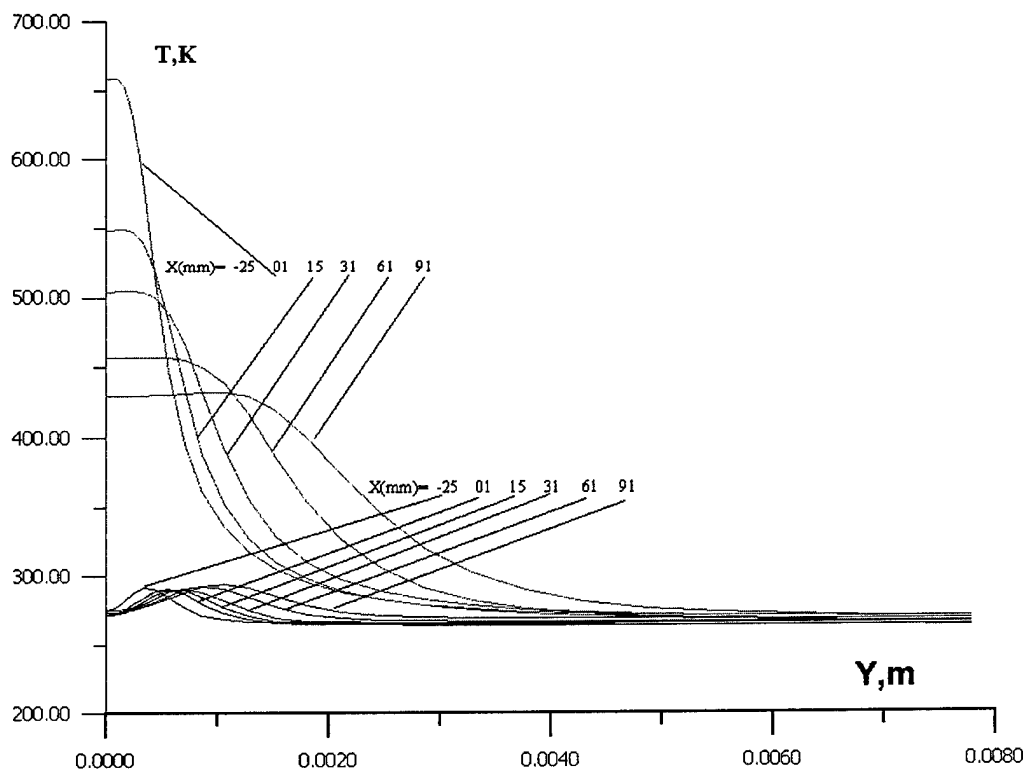


Fig.5.1.5. Temperature profiles in a boundary layer.

Blue lines are corresponded to run without plasma and red lines are corresponded to run with energy input. Well seen that outside of boundary layer the temperature is practically the same in both cases.

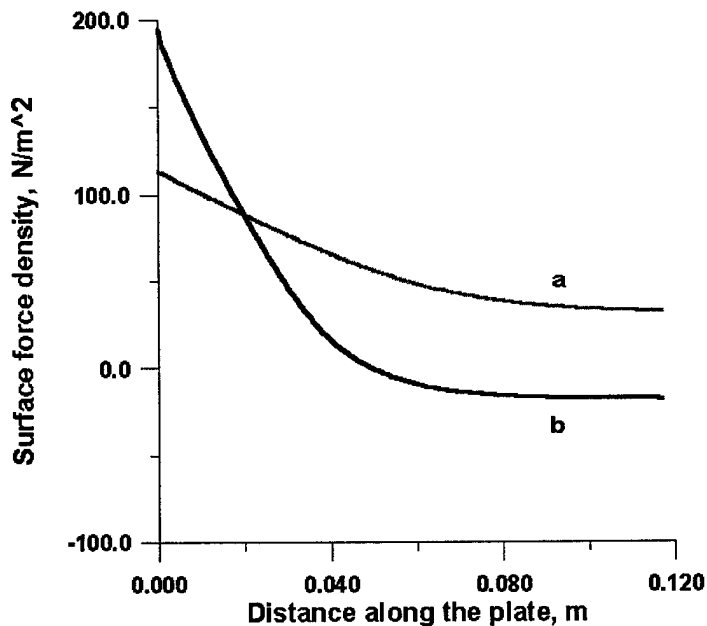


Fig.5.5.6. Distribution of the surface force density on the test plate.

a) flow without discharge,
total force is 6.91 N;

b) flow with discharge,
total force is 2.68 N.

In Fig.5.1.6 the wall friction distribution over the test plate is shown for both cases, without discharge (a) and with discharge (b). The net force values are also pointed out. The calculations give a negative force density near a base part of the plate. It corresponds to a separation process. Clear that in these cases the laminar boundary layer not exist. So the laminar approach is not adequate here.

A rough effort of simulation of the situation with an artificial obstacle (separation zone) has been provided. A calculated flowfield is presented in Fig.5.1.7-5.1.8 (Mach number and V-vectors without plasma and at plasma) and Fig.5.1.9 (pressure distribution and temperature contours).

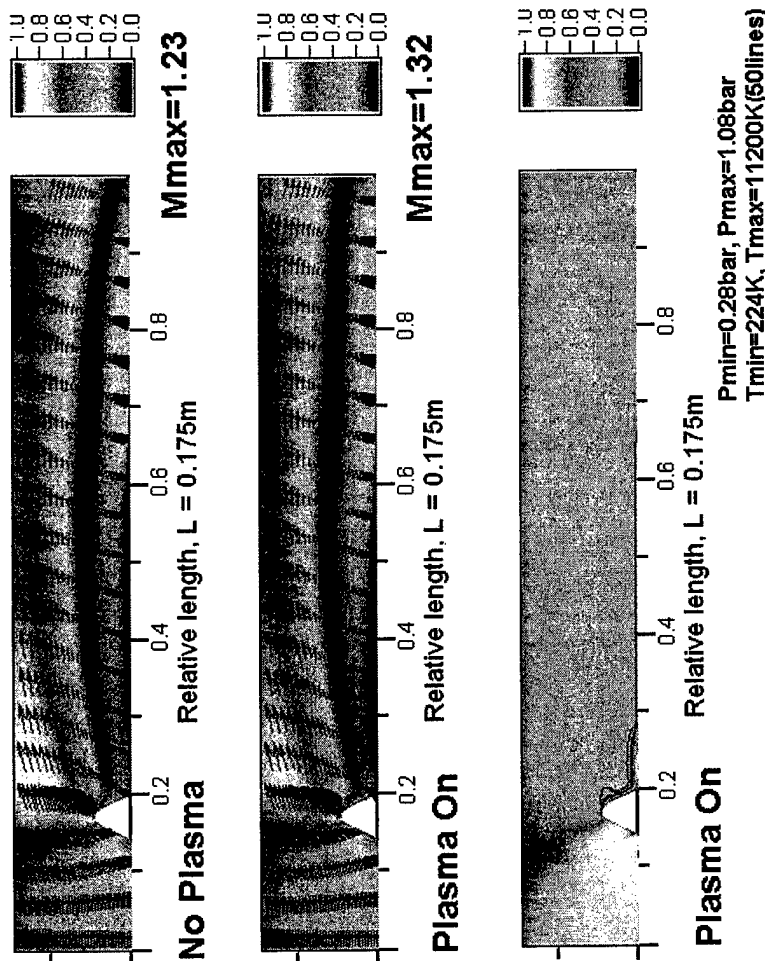


Fig.5.1.7.

Fig.5.1.8.

Fig.5.1.9.

Such calculations give only qualitative results. Seen that in case of plasma the separation zone is much huge. Mach number over such a zone has a more value. Clear that for more adequate results a model with turbulence should be applied.

5.2. Simulation in frames of turbulent boundary layer model.

The numerical analysis of experiments has been performed on a basis of plane viscous flow model at presence in the stream near wall a local heat supply region. Discharge on the model was simulated of this heat source. The thermally equilibrium chemically frozen model of heated air was used in these calculations. The turbulent flow is described by the Favre-averaged Navier-Stokes equations with additional source term in the energy equation. The Boussinesq approximation for the Reynolds stress tensor and algebraic Baldwin-Lomax turbulence model for calculation of turbulent transport coefficients is used. The laminar flow equations (Navier-Stokes equations) are obtained by neglecting the turbulent contributions. It is supposed that heat source term in co-ordinate system (s,n) , where s is distance along plate from its begin and n distance along normal from plate to point with co-ordinate (s,n) is written in the following form:

$$q_h = C_q F(s) G(n)$$

where functions $F(s)$ and $G(s)$ are given by

$$F(s) = \begin{cases} 1 & \text{for } s_{hb} \leq s \leq s_{he} \\ 0 & \text{for other cases} \end{cases} ; G(n) = \begin{cases} 1 & \text{for } 0 \leq n \leq n_{he} \\ 0 & \text{for other cases} \end{cases}$$

The value of C_q is defined from conditions

$$\int_{S_c} q_h ds = P_d$$

where S_c is computation domain, P_d - input power in heat per unit length. The viscosity is calculated using a power law variation with temperature, $\mu = a_\mu T^{0.683}$, molecular Prandtl number is $Pr = 0.7$ and turbulent Prandtl number is $Pr_t = 0.9$. It is supposed that on a body surface for velocity the no-slip condition $\bar{u} = 0$ and for temperature heat-isolated condition $q_w = 0$ are fulfilled, where q_w is heat flux to the wall.

The steady solution was found with help of time-marching technique using for numerical integrating of unsteady Navier-Stokes equations an implicit monotone difference scheme second order of accuracy, constructed with finite-volume approach. The inviscid fluxes through the interfaces of cells are calculated using exact Riemann problem solution defined by interfacial values of parameters in the adjoining cells. For determination these values it was used the non-oscillating one-dimensional reconstruction

of primitive variables: pressure p , temperature T and vector velocities \vec{u} inside cells along appropriate coordinate direction. Viscous fluxes through the "interior" sides of cells were determined on the space centered difference formulas and through the sides lying on the body surface using one-sided three-dot difference approximations. On every time step the flowfield parameters were defined due Gauss-Seidel line relaxation numerical technique.

The calculations were performed for laminar and turbulent models of flow at Mach number $M_\infty = 0.6$ and 1.0, total pressure $p_0 = 1 \text{ atm}$, total temperature $T_0 = 300 \text{ K}$, $P_d = 0$ and 270 W/cm , $s_{hb} = 2.5 \text{ cm}$, $s_{he} = 3.5 \text{ cm}$, $n_{he} = 0.1 \text{ cm}$. The grid 150×150 adapted to flow peculiarity was employed. The grid cells were condensed near plate surface, so that in a laminar sublayer region not less than 10 grid points are placed.

Fig. 5.2.1 shows the distributions along plate a Reynolds number Re_θ calculated through momentum thickness θ for conditions at outer edge of the laminar boundary layer (for $P_d = 0$). The value $Re_\theta = 300$ often is used as criterion of laminar -to-turbulent transitions. As the Fig.5.2.1 indicates transition (without heat supply) begins at $s \approx 2 \text{ cm}$ for both Much number if this criterion use.

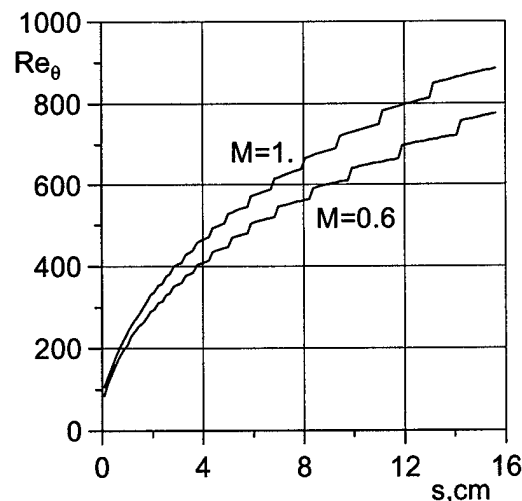


Fig. 5.2.1. Distributions of Reynolds number, calculated through momentum thickness

In table 5.2.1 it is listed values of total skin-friction coefficients C_f of moving part of plate (test plate) that was placed from $x = 4$ cm to $x = 16$ cm. The value of C_f is defined by expression

$$C_f = \int_{s_1}^{s_2} \tau_w ds / 0.5 \rho_\infty V_\infty^2 (s_2 - s_1),$$

where τ_w is skin-friction.

Table 5.2.1 Skin-friction coefficients of test plate

$C_f \cdot 10^3$	M	Pd, W/cm	Flow regime
0.662	0.6	0	laminar
0.449	0.6	375	laminar
3.17	0.6	0	turbulent
2.00	0.6	375	turbulent
0.563	1.0	0	laminar
0.420	1.0	375	laminar
2.90	1.0	0	turbulent
1.98	1.0	375	turbulent

This table indicates that the heat supply leads to decreasing of skin-friction both for laminar and turbulent flow. The peak of drag reduction for laminar flow is 0.68 and for turbulent flow it is 0.63.

On Fig.5.2.2-5.2.4 it is compared the distributions of wall temperature, pressure and local skin-friction coefficient along plate surface obtained in considered variants of calculations for $M_\infty = 0.6$. Similar data for $M_\infty = 1.0$ are presented in Fig. 5.2.5-5.2.7. Here and on all other figures by light symbols are designated results corresponding to $P_d = 0$, but by dark symbols correspond to results for $P_d = 375$ W/cm. The square symbols correspond to laminar flow, by round symbols are presented data for turbulent flow regime.

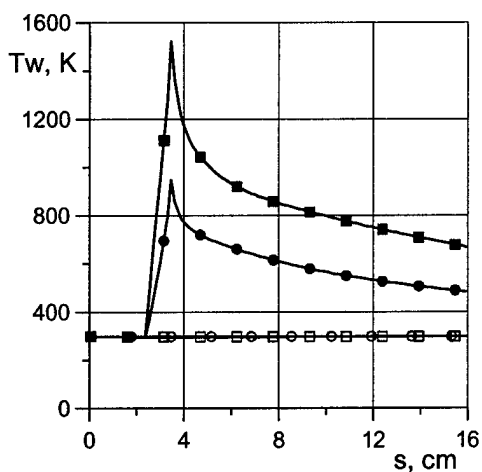


Fig.5.2.2. Wall temperature. $M_\infty = 0.6$.

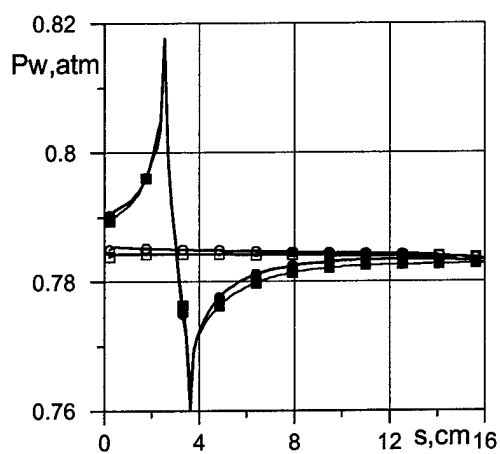


Fig.5.2.3. Wall pressure. $M_\infty = 0.6$

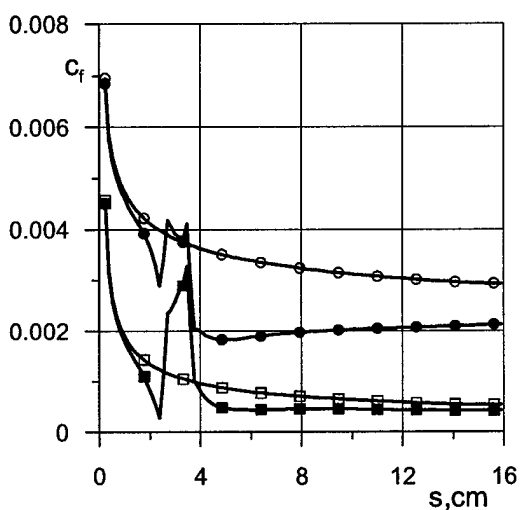


Fig.5.2.4. Skin friction coefficient. $M_\infty = 0.6$

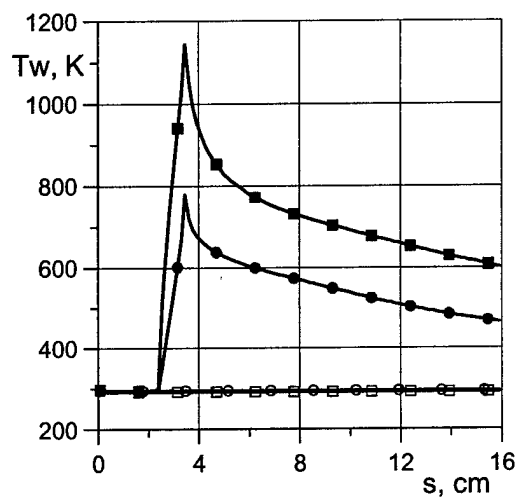


Fig.5.2.5. Wall-temperature $M_\infty = 1$.

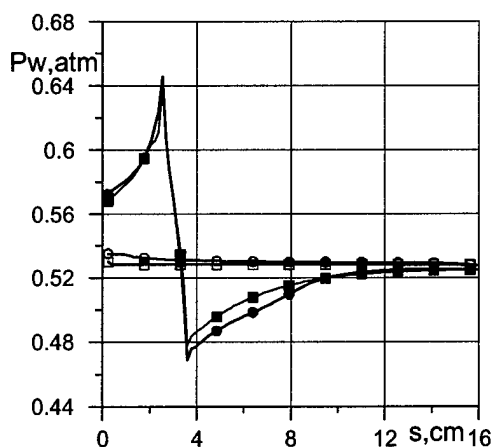


Fig.5.2.6. Wall pressure distribution.

$$M_{\infty} = 1.$$

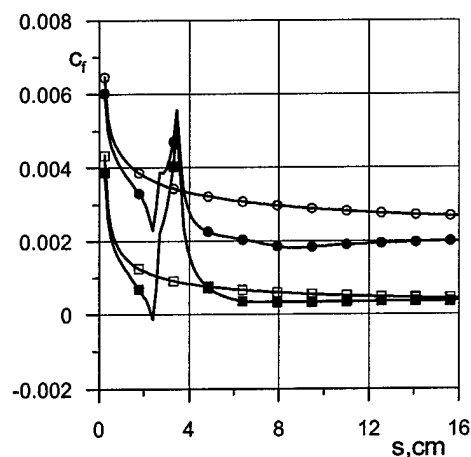


Fig.5.2.7. Skin-friction coefficient.

$$M_{\infty} = 1.$$

In Fig. 5.2.8-5.2.11 the distributions of the longitudinal component of velocity vector divided on free stream velocity, u/u_{∞} and gas temperature, T, K along normal to plate surface at $s = 3.6 \text{ cm}$ (in the end of heating region) and at $s = 10 \text{ cm}$ (in the moving plate center) are presented.

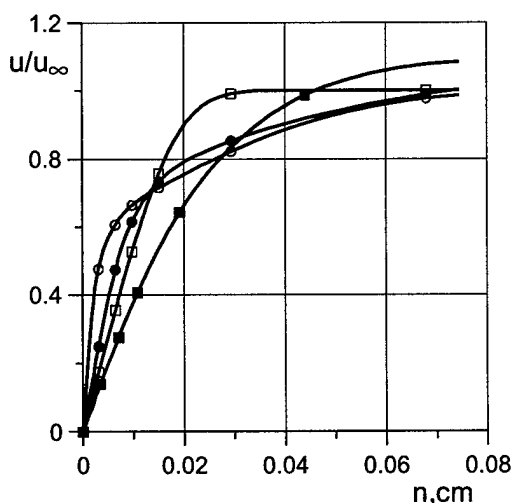


Fig.5.2.8. Velocity distributions.

$$M_{\infty} = 0.6, s = 3.6 \text{ cm}$$

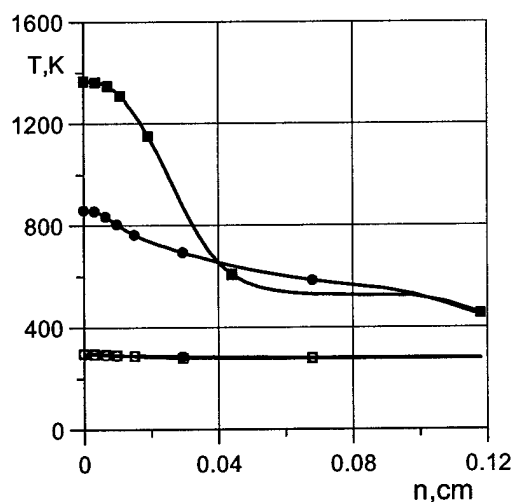


Fig.5.2.9. Temperature distributions

$$M_{\infty} = 0.6, s = 3.6 \text{ cm}$$

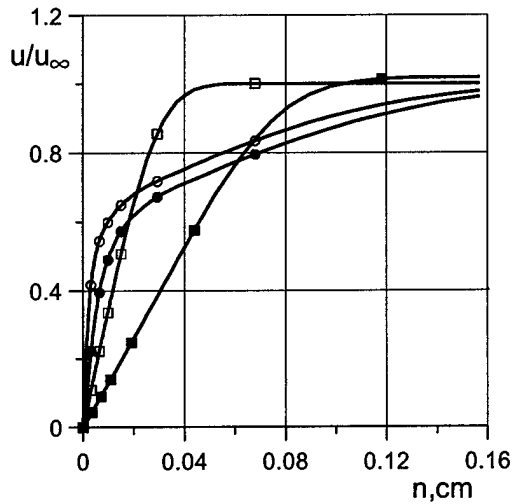


Fig. 5.2.10. Velocity distributions.

$M_\infty = 0.6$, $s = 10$. cm

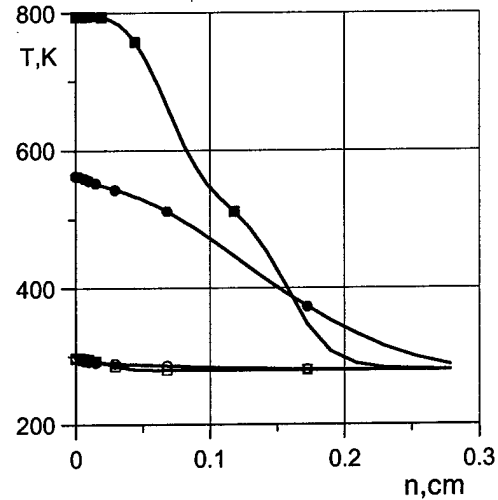


Fig. 5.2.11. Temperature distributions

$M_\infty = 0.6$, $s = 10$. cm

This data were obtained for $M_\infty = 0.6$. Similar results for $M_\infty = 1$. is displayed in Fig. 5.2.12-5.2.15.

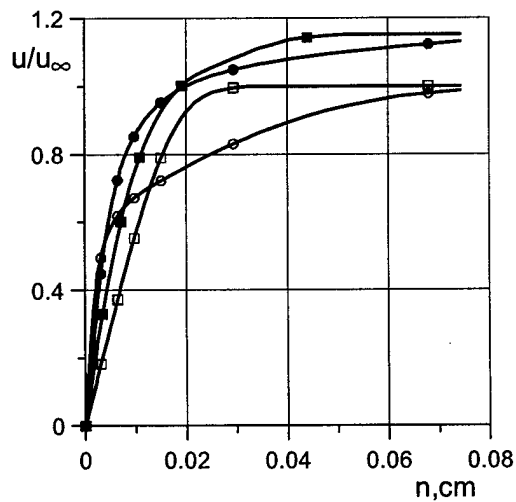


Fig. 5.2.12. Velocity distributions

$M_\infty = 1.0$, $s = 3.6$ cm

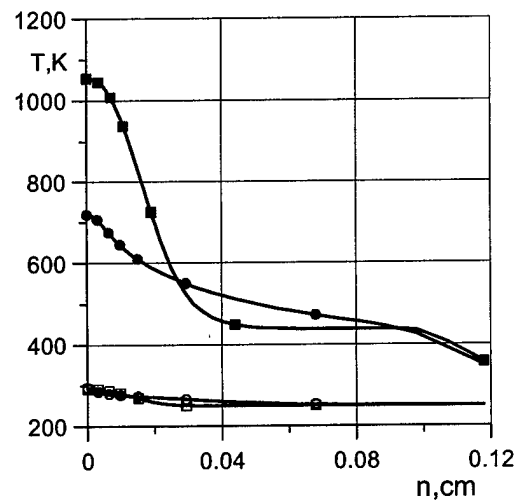


Fig. 5.2.13. Temperature distributions

$M_\infty = 1.0$, $s = 3.6$ cm

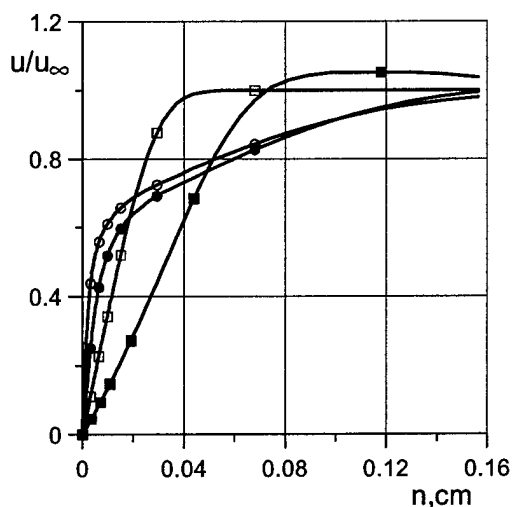


Fig.5.2.14. Velocity distributions

$M_{\infty} = 1.0$, $s = 10$ cm

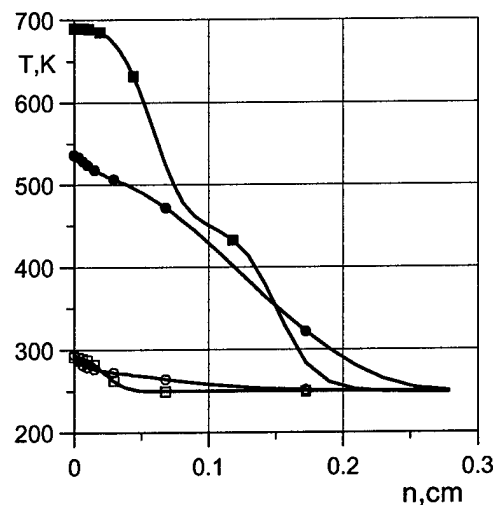


Fig.5.2.15. Temperature distribution

$M_{\infty} = 1.0$, $s = 10$ cm

So, the intermediate conclusion is that simulation in frames of turbulent boundary layer gives a good agreement with an experimental data qualitatively. A quantitatively agreement can be achieved by adjusting of condition and initial data. A more comprehensive simulations in a such way are required.

5.3. Analysis of data.

During analysis of friction drag reduction methods it was noted that the condition of boundary layer determining value of friction stresses depends on a great number of factors. All of them could be broken in three groups:

- factors, connected with parameters and properties of the inviscid flow external to the boundary layer;
- factors, determined by conditions on the round-flown surface and properties of the wall itself;
- factors, determined by properties of gas in the boundary layer itself and by aerothermochemical processes developing inside it.

It is necessary to note that the third group of factors when it is not subject to external action is determined by the factors of the first two groups, i.e. is dependent on them, and there is no sense to allocate them to a separate group. However the situation changes when there is an external action against the boundary layer not dependent on the wall conditions and those in the external inviscid flow. Direct energy supply right into the boundary layer via electrical discharge, laser or microwave radiation, etc. could be an example of such external action.

Besides, condition of the boundary layer downstream, as it was noted earlier, in many respects is determined by conditions of its formation (origin). It is stipulated by the fact that losses of mechanical energy in those places, as the practice shows, are maximal. Their value may come out different depending on flow mode (laminar or turbulent), as well as on whether the boundary layer is formed in a flow or the one earlier torn off the surface is being attached.

Desire to take into account influence of as many of the factors referred to above as possible during experimental research of influence of electrical discharge upon value of friction drag has determined selection of transonic flow modes ($M=0,4 - 1,05$).

The following reasons have served as the basis for such selection:

- Within the chosen range of Mach numbers there was a possibility of feeding electrical discharge energy both in subsonic, and in supersonic boundary layers;

- During turbulization of laminar boundary layer with shock waves there arises an opportunity of researching the influence of energy feed to the boundary layer on this laminar-turbulent transition.
- In transonic modes changes of the boundary layer condition are demonstrated most sharply, being expressed in easily observable changes of the external inviscid flow structure. Emergence of a lambda shock demonstrates that the boundary layer was laminar before interaction, while one straight shock appears in case of a turbulent boundary layer.
- Energy feed into the boundary layer causing friction stresses change may, due to convective heat exchange, result in transfer of shock waves to the external cold flow and, as a consequence, to redistribution of surface pressure, i.e. wave impedance change.

Optical and weight experiments have been conducted in executed research of influence of electrical discharge in the boundary layer on the friction drag. At Mach numbers larger than critical, optical experiments appeared to be more informative, while at smaller Mach numbers - the weight experiments. The reason is that at large supercritical Mach numbers the presence of shock waves results in increased pressure around back edge of the movable plate as compared with pressure at its front edge. This pressure difference attacks end faces of the movable plate through the gaps, creating forward-directed force. The value of this "thrust" significantly surpasses friction drag, therefore frictional force changes caused by discharge turned out insignificant because of high level of aerodynamic vibrations. It is necessary to find ways to compensate that "thrust" later. At subcritical and small supercritical Mach numbers this force was absent or was commensurable with a friction drag, therefore the latter's variation in those modes managed to get registered.

Discussion of optical and weight experiment results.

Flat plate.

$\dot{I}_{\infty}=0.9-0.99$. Photographs received with a Schlieren shadow device allow to note the following features. There is a lambda shock formed in the front part of the plate. The first (oblique) lambda shock appears approximately at the nose of the model, while the main shock is localized in the plate area, moving up and down the flow as measured against the middle of the plate. It is necessary to note, that the reason for bifurcation of the first oblique lambda shock in the upper part is its weakening by disturbance waves radiating from a part of the fixed plate, on which the electrodes are placed. For the same reason, as well as because of weakening of the first oblique lambda shock, it is possible to observe some "diffuseness" of the main shock wave (photo of runs 1 and 11). These photos match cases of flow without discharge and with discharge. Switching on discharge does not influence the first oblique lambda shock form, resulting, nevertheless, in essential change of the main shock wave. On shadow photos it is possible to see separation and noticeable bias down the flow of the main shock in the middle part of the model's width, where the electrical discharge energy was supplied to the boundary layer. It is possible to put in the basis of explanation of those phenomena the following considerations. The place of discharge is a source of the boundary layer laminarization because of gas viscosity increase in the boundary layer. Due to that intensive intermixing of heated in discharge and cold layers of external flow gas occurs later. A boundary "plasma" thermal layer is formed, which cross-sectional sizes are much greater than thickness of the boundary layer itself in case of discharge absence. It results in laminar-turbulent transition point moving down the flow and increasing the effective Mach number of the flow in supersonic area. Hence, the straight shock relocates downstream.

The same features are exhibited in the case of supplying energy behind an obstacle in the form of triangular barrier set before the movable plate (run 01). It is necessary to pay attention here to absence of disturbance waves produced in the previous cases by plate/electrode and electrode/electrode joints, since they are in a stagnant zone behind the obstacle. As a result the first oblique lambda shock, following the powerful centered wave of rarefaction going out of the side top, has, as it is seen in the picture, a precisely contoured shape. It is also necessary to note, that energy supply to the stagnant area is characterized by larger power insertion, than in the previous cases. Therefore heat up of

large masses of gas at the wall results in "spreading" the shock in the boundary layer at a greater distance from the wall.

$\dot{I}_{\infty}=0,8 - 0,9$. On the shadow photos one can also see a lambda shock, which position completely meets known legitimacies of transonic flows - when Mach number is decreasing, extent and intensity of shock waves go down too, and they move to the front edge. It is confirmed by comparison of flow patterns to strain gauge readings record. These photos show that the main shock wave at discharge burning moves from the movable plate to the area located between electrodes, while the slope angle of the first oblique lambda shock increases.

$\dot{I}_{\infty}=0,6-0,7$. For runs 3 and 4 of 28.09 the information available does not allow to make absolutely justified conclusions. However processed shadow photos allow to make a cautious conclusion about a probable laminarization of the boundary layer, i.e. tightening of laminar - turbulent transition.

$\dot{I}_{\infty}=0,4-0,6$. Emergence of boundary layer heating effect. The obstacle on the movable plate stabilizes discharge because of a stagnant zone formation.

Contoured (cylindrical) plate.

$\dot{I}_{\infty}=0,8$. During runs 15 and 16 shadow photos do not show visible differences in pressure distribution for cases with and without discharge, which provides grounds to believe that the apparent reduction of drag at burning discharge is stipulated by reduction frictional force. This reduction of frictional force is determined by the boundary layer thickness increase due to its heating by electrical discharge.

$\dot{I}_{\infty}=0,4-0,56$. Weight tests show, that discharge results in drag reduction of approximately 30-90%. The shadowgraphs show noticeable difference between cases with switched on and switched off discharges in the boundary layers. With discharge switched on one can observe a thick enough homogeneous heated up boundary layer. The reason of dropping drag should be searched for in heating of the boundary layer. It allows making a conclusion that in the latter case the boundary layer was laminar before the

discharge, while switching on discharge has not changed flow mode in it, considerably lowering viscous drag.

Transonic flow.

At large supercritical Mach numbers a lambda shaped shock wave (lambda shock) is formed on the top of the model. The first oblique lambda shock starts approximately from the model's nose, while the main shock is located approximately in the middle of the movable plate. The flow boost to supersonic velocity in the top of the flow becomes possible due to formation of a small locked separation area near the front sharp edge being a corollary of flow stall because of a small positive angle of attack. This angle of attack (equal to zero prior to the run) is being established after the duct (WT)'s reaching the working mode due to strong lifting force, defined by the model's asymmetry. Switching on the discharge, as one can see on the photo, barely influences the first oblique lambda shock's shape, while the main shock wave moves downstream noticeably. The explanation to this phenomenon can be given according to the following arguments.

It is known that after passing of the first oblique lambda shock, depending on its intensity the boundary layer may remain laminar, become turbulent or tear off the plate's surface with a subsequent affixion (separation zone formation). Let's consider two schemes of flow in Fig.5.3.1 and Fig.5.3.2. The first scheme matches the case, when the boundary layer remains laminar, the second one - when the boundary layer behind the first oblique lambda shock became turbulent. Here $V_s = a$ is a sonic velocity.

In the first case the subsonic part of the boundary layer is much greater in thickness than in the case of the turbulent boundary layer (compare velocity profiles). Therefore shock wave strength in the boundary area in the first case is lower, than in the second one. On the other hand, thickness of the turbulent boundary layer along the plate grows faster, than thickness of the laminar layer. Therefore deceleration degree of the external supersonic flow before the main shock in the second case will be greater. These two circumstances (larger intensity of the main shock and smaller local Mach numbers before it) result in placement of the main shock wave in the second case closer to the front edge.

Applying those reasons to our case, it is possible to explain displacement to the stern part of the main shock wave at burning discharge, if the following suppositions are made.

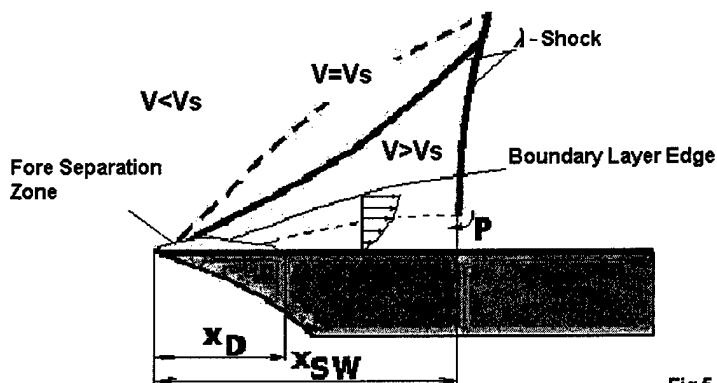


Fig.5.3.1.

Fig.5.3.1.

Flow scheme at
laminar boundary
layer.

Transonic mode.

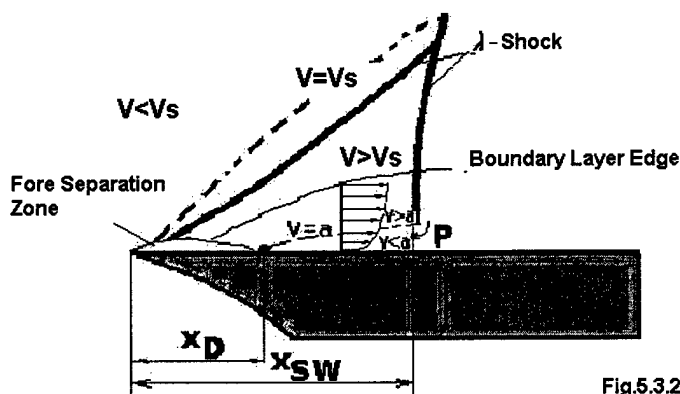


Fig.5.3.2.

Fig.5.3.2.

Flow scheme at
turbulent boundary
layer.

Transonic mode.

With Mach number close to one, intensity of the first oblique lambda shock is sufficient for the boundary layer attached behind the front separation area to become turbulent. This case is matched with shock wave structure on the photo of switched off discharge. Application of electrical discharge energy laminates the turbulent boundary layer formed after affixing, by warming it up (increments its mechanical energy and reduces Reynolds's number). The latter in view of the above-mentioned arguments (Fig.5.3.1) provides an explanation of the reasons for displacement of the main shock wave to the stern part of the model.

Subsonic profile flow around.

According to weight tests results, at Mach numbers smaller than critical burning of discharge at the plate before the front edge of the model's contoured movable part results in considerable drag reduction. This reduction of general drag is a consequence of reduction of both friction and profile drag. The reasons of friction drag decrease are described above. As for profile drag decrease, it could be explained if the discharge "flow around" model were accepted (see item. 2.3). Provided that the discharge, burning at the wall, is flown around by airflow, the model flow pattern will look as shown on fig. 2b. It is visible here that discharge organized directly behind the front separation zone, which in this case becomes open, together with it forms an extended stagnant area in front of the lower pressure profile. Pressure decrease at the frontal part of the profile results in profile drag decrease. It is possible to arrive to such conclusion comparing flow patterns of the profile without discharge in Fig.5.3.3 and with burning discharge in Fig.5.3.4.

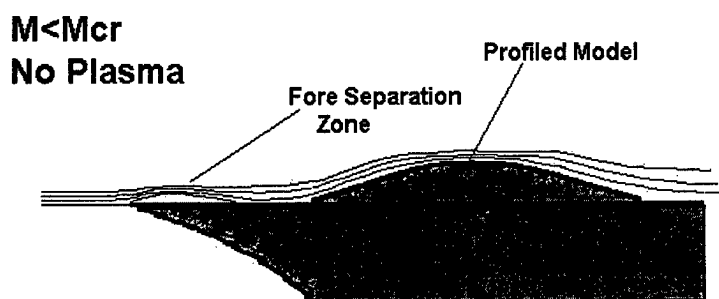


Fig.5.3.3.

Fig.5.3.3.
Flow scheme at
subsonic mode.
No Plasma.

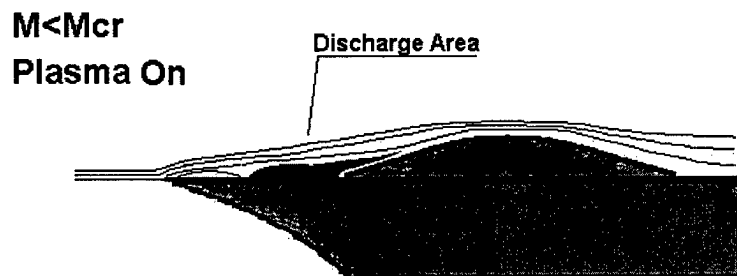


Fig.5.3.4.

Fig.5.3.4.
Flow scheme at
subsonic mode.
Plasma is switched
on.

6. Conclusions.

1. The work has demonstrated the fact of considerable influence of surface plasma formation on characteristics of flow around developed surface models. The rule of feasibility of applying exposure to the boundary layer in the field of maximal losses of mechanical energy has been confirmed.
2. The work has demonstrated the fact of transonic flow structure changing when exposed to plasma formation close to flown near model surface. Energy supply to the boundary layer in transonic modes may result in reformation of shock wave structure, which in various cases may appear both positive and negative from friction drag point of view. The shift of a direct shock wave above the surface has been observed in a result of plasma influence.
3. At subsonic regime of contoured plate flow around there has been obtained a flow drag reduction by several times through surface discharge.
4. Certain results mentioned above demonstrate a capability of prolonging laminar-turbulent transition, as well as reducing friction drag in case of both laminar and turbulent modes of flow in boundary layers with the help of correctly organized electrical discharges.
5. The work conducted comparison of experimental data and calculation results within the framework of laminar boundary layer and turbulence development models. Obtaining of the experimental data volume allows to verify calculation codes for problems with surface energy input.
6. For maintenance of stable discharge burning the electrodes should be placed behind shelves or in cavities, if the surface design allows. On flat surfaces it is necessary to apply discharges with high propagation velocity, for example high frequency or pulse streamer \ filament discharges. The design of a plasma generator and definition of operation modes depends on specific conditions (no universal decisions).

7. Program of further activity.

Lets describe briefly what could be done experimentally in a field of a discharge plasma influence on parameters of boundary layer. By the other words, how this work can be continue. Obviously that the program is not comprehensive.

1. Discharge Development.

Development of electrodeless or a single electrode HF surface discharge of filamentary type with a relatively high level of energy input.

Development of methods of control of filamentary plasma position in defined zones. Development of methods of control of distribution of energy release.

Design of special power supplies and circuits of energy input to the plasma.

2. Transonic mode.

Study of the physic mechanisms of plasma influence on shocks position near the surface. Application of diagnostic methods for a boundary layer parameter measurements.

Measurements of local airflow parameters near the surface at plasma operation. Development of methodic of separation friction and pressure distribution effects.

Study of effect on a profiled plate (at primary position of λ -shock downstream the plasma volume).

3. Subsonic mode.

Continuation of development of plasma influence on laminar-turbulent transition. Plasma influence on position and dimensions of separation zones near the AD elements conjunction.

Study of condition for a realization of separationless flows.

4. Scaling problems.

Prediction possible effects for a full scale vehicle. Energetic efficiency.

5. Study of processes of friction reduction at "high" temperature.

8. References

1. Workshop on Weakly Ionized Gases. USAF Academy, Colorado, 9-13 June 1997; Second Workshop on Weakly Ionized Gases. Proceedings. Norfolk, 24-25 April 1998, Third Workshop on Weakly Ionized Gases. Proceedings. Norfolk, 1-3 November 1999.
2. V.Bityurin, A.Klimov, S.Leonov "Assessment of a Concept of Advanced Flow/Flight Control for Hypersonic Flights in Atmosphere". November 1-5, 1999 / Norfolk, Virginia, AIAA 99-4820.
3. T. Cain, D. Boyd "Electrodynamics and the effect of an electric discharge on cone/cylinder drag at Mach 5", 37th AIAA Aerospace Sciences Meeting and Exhibit, January 11-14, 1999/Reno, NV, AIAA 99-0602.
4. S. Leonov, V. Nebolsin, V. Shilov "Effectiveness of plasma jet Effect on Bodies in an Airflow", Proceedings of Workshop "Perspectives of MHD and Plasma Technologies in Aerospace Applications", Moscow, IVTAN, 1999, pp. 58-65.
5. G.G.Chernyi, The impact of electromagnetic energy addition to air near the flying body on its aerodynamic characteristics. 2-nd WIG Workshop, proceeding, Norfolk, VA, April 24-25, 1998. Levin V. A., Afonina N. E., Gromov V. G., Influence of Energy Input by Electric Discharge Supersonic flows around bodies. 2nd WIG Workshop, Proceedings, Norfolk, VA, April 24-25, 1998.
6. D. Bushnell, C. McGinley Turbulence Control in Wall Flows, Ann. Rev. Fluid Mech., 21, 1-20, 1989.
7. S.Leonov "Experiments on Influence of Plasma Jet on Lift and Drag of Wing", Proceedings of WIG-1, USAF Academy, Colorado, 9-13 June 1997, pp. J1-J24.
8. Kazakov A., Kogan M., Kuriachi A., Influence on the friction of local heat addition to the turbulent boundary layer. Mech. Of Fluids and Gases, N1, 1997. Kurjachi A. P., Boundary layer transition by means of electrodynamics method. Prikl. Math. I Mech., vol.49, issue 1,1985. A.V. Kazakov, A.P. Kuryachii, Electrogasdynamic influence on the development of the small diturbances in a boundary layer in the thin profile Izv. ÀN USSR, Mekhanika zhidkosti i gaza, 1, 1986
9. Yu.V. Shcherbakov, N.S. Ivanov, and others, Drag Reduction by AC Streamer Corona Discharges along a Wing-like profile Plate. AIAA 2000-2670.

10. D. Kyukheman, Aerodynamic Planes Designing. M.: Mashinostroyeniye, 1983, p.555.
11. P. Chang, "Separation flow." Moscow: Mir, 1973 v.3, p.14.
12. A.S.Yuriev, V. Yu. Borzov, I.V.Ryibka, Dependence of high-speed elements on local heat sources in approaching flow, 2nd WIG Workshop, Proceedings, Norfolk, VA, April 24-25, 1998.
13. V.M. Nizovtsev, N.P. Savishyenko, A.S. Yuriev, Method of the definition of the heat emission coefficient on a model surface in a gas flow with use of laser radiation, 10th Vsesoyuznaya teplofizicheskaya shkola "Fizika relaksiruyushikh sistem", Tambov, 1990.(rus.)
14. Goshek, High-speed Aerodynamics, S.: "Inostrannaya literatura", 1954
15. J. M. Floryan, W. S. Saric, Effects of Suction on the Gortler Instability of Boundary Layers, Aerospace Technics, vol. 2, No. 7, July, 1984, p.p.134-139.
16. V.M. Gilev, V.V. Kozlov, Influence of a periodic injection-suction on a process of transition in a boundary layer. Preprint 1-85. Novosibirsk: ITMP SO AN USSR, 1985
17. O.A. Efremov, O.S. Ryzhov, E.D. Teren'tyev, About damping unstable oscillations in a boundary layer, Izv. AN USSR, Mekhanika zhidkosti i gaza, 1987, p.p. 20-26.(rus)
18. NASA, Rep. 1358, 1958.
19. Technical information // News of foreign science and engineering. Air and rocket engineering / INTI TsAGI , 3, 1984, page 1-32.
20. G.V. Yenyutin, Yu.A. Lashkov, N.V. Samoylova, Experimental research of influence longitudinal edging on plane plate friction drag, Izv. AN USSR, Mekhanika zhidkosti i gaza, 2, 1987
21. Walsh M. J., Lindemann A. M., Optimization and application of riblets for turbulent drag reduction | 22nd AIAA Aerospace Sciences Meeting. January 9-12, 1984, Reno, Nevada/
22. P. K. Chang, "Control of Flow Separation." M.: MIR, 1979.
23. G. Schlichting, The theory of a boundary layer, M.: Nauka, 1974
24. A.P. Mel'nikov, I.A. Sychyov, N.F. Fillipov, Gashydrodynamics, L. p. 470, 1968
25. V.N. Nizovtsev, G.N. Moskalets, Influence of the local heat- and mass supply area arrangement on pressure and friction profiles (distribution) on the plate

- surface in supersonic viscous gas flow, In issue "Methods of researches of the aerothermodynamic characteristics of the hypersonic flight vehicles", Thes. Of the reports, shkola-seminar TsAGI "Mekhanika zhidkosti i gaza", Feb. 25 - March 1, 1992 p.p.140-141
26. Larin O., Numerical Investigation of the flow in supersonic laminar boundary layer with external heat addition, Inst. Of Mech. Moscow Univ., Report 4351, 1994.
27. Larin O., The turbulent supersonic flow in boundary layer with external heat addition. Inst. Of Mech. Moscow Univ. Report 4436, 1995.
28. Kazakov A., Kogan M. N., Kuparev V. A., Subsonic boundary layer stability increase due to near leading edge surface heating. Mech. Of fluids and Gases, 3, 1985.
29. A.V. Kazakov, A.P. Kuryachii, Electro-gasdynamics influence on the development of the small disturbances in a boundary layer in the thin profile Izv. AN USSR, Mekhanika zhidkosti i gaza, 1, 1986
30. P. Baronets, A. Kolesnikov, S. Kubarev... Super-equilibrium heating of surface in subsonic jet of dissociated air. Izvestiya RAS, MZhG (rus) 3, 1991, p.144-149.
31. Yu. Rayzer "Physics of gas discharge." Moscow: Science. 1987. pp 479.
32. Creation of Perspective Plasma Generators for Plasma Aerodynamic Experimental Investigation on Supersonic and Hypersonic Flows. Report EOARD No.SPC-97-4004, Moscow, 1998.
33. "Analysis of Plasma Influence on Aerodynamic Characteristics of Body in Airflow." Report on APL/JHU-MTC Contract No785461, Moscow, April, 1998.
34. Workshop on Weakly Ionized Gases. Proceedings. USAF Academy, Colorado, 9-13 June 1997. T. Cain, M. Gilmore, Meeting Report, "The Ministry of Defense's Plasma Drag Reduction Program", Section S.
35. Efimov B.G., Kuznetsov Yu.E., Litvinov V.M., Skvortsov V.V., Klimov A.I., Leonov S.B. "Plasma Aerodynamic Experiments in TsAGI", Proceedings of 2-nd Workshop on MHD and PA Applications..., Moscow, IVTAN, March 2000.
36. Burdakov V.P., Baranovsky S.I., Klimov A.I., Lebedev P.D., Leonov S.B., Pankova M.B., Puhov A.P. "Improvement perspectives of aerodynamic and thrust-energetic parameters of hypersonic aircraft and engines when using algorithmic discharges and

- plasmoid formations.”, Proceeding of the International Conference of Advance. Technology, Moscow, 1995
37. Tretyakov P.K., Garanin A.F., Kraynev V.L., Tupikin A.V., Yakovlev V.I. Investigation of Local Laser Release Influence on Supersonic Flow by Methods of Aerophysical Experiments // International Conference on the Methods of Aerophysical Research. Novosibirsk. ITAM. 1996. Vol.1. pp200-204
 38. Georgievsky P.Yu., Levin V.A. Supersonic Flow over Body in Presence of Heat Supply Before It // Trudy MI AN SSSR. Modern mathematical problems of mechanics and their applications. 1989. Vol.186. pp.197-201 /in Russian/
.Georgievsky P.Yu., Levin V.A. Supersonic Flow over Bodies in Presence of External Heat Supply Sources // Pisma v GTV. 1988. Vol.14. No.8. pp.684-687 /in Russian/
 39. Artemiev V.I., Bergelson V.I., Nemchinov I.V. Modification of the Regime of Supersonic Flow over the Barrier at Appearance of Fine Rarefied Channel Ahead //Izv. AN SSSR, MGG. 1989. No.5.
 40. Bagenova T.V., Lahov V.N., Pankova M.B., Haritonov S.M. Numerical Modeling of Influence of Heat Nonuniformity at Supersonic Flow on the Wave Drag Coefficient of Spherical Bdy // Numerical modeling of unsteady gas dynamics and MYD flows.- Moscow. IVTAN Pub. 1989. pp.53-64 /in Russian/
 41. Borzov V.Yu., Ribka I.V., Yuriev A.S. The Influence of Local Energy Supply at Hypersonic Flow on Wave Drag of Bodies of Different Blunting // Eng.-Phys.Journal. 1994. Vol.67. No.5-6. pp.355-361. /in Russian/
 42. Georgievsky P.Yu., Levin V.A. Modification of Regime of the Flow over a Sphere by Means of Local Energy Supply Upstream // International Conference on the Methods of Aerophysical Research. Novosibirsk. ITAM . 1996. Vol.3. pp.67-73
 43. Arafailov S.I. The Influence of Energy Supply at the Shock Layer on Supersonic Flight of Bodies // Izv.AN SSSR. MGG. 1987. No.4. pp.178-182
 44. Korotaeva T.A., Fomin V.M., Shashkin A.P. Numerical Investigation of the Local Energy Supply Effect on the 3-D Flow around Pointed Bodies. Inst. of theor. and appl. Mech. RAN. Preprint N1-96. Novosibirsk. 36 p. /in Russian/
 45. Levin V.A., Afonina N.E., Georgievsky P.Yu., Gromov V.G., Terentieva L.V. Influence of Energy Input by Electric Discharge on Supersonic Flows around Bodies. Proceedings of 2-th Weakly Ionized Cases Workshop, Norfolk, VA, 1998, pp.201-231

46. Baldwin B.S. and Lomax H., Thin-Layer Approximation and Algebraic Model for Separated Turbulent Flows, AIAA Paper 78-257, 1978.
47. Alferov V.I., Electrical discharge in a gas flow, Thesis, Moscow, Moscow Physical and Technical Institute, 1987.
48. Turbulent Flows and Heat Transfer. Ed.C.C.Lin Princeton. New Jersey, Princeton University Press, 1959.
49. P. Wu, R. Miles, MHz Rate Visualization of Separation Shock Wave Structure, AIAA-2000-0647.
50. A. Yalin, W. Lempert and others, Planar imaging in a Mach 8 flow using sodium laser-induced fluorescence. AIAA-96-2270.
51. J. Naughton, M. Sheplak, "Modern Skin Friction Measurement Techniques: Description, Use, and What to do With the Data." AIAA-2000-2521.

9. Acknowledgment.

This Report is based upon work supported by the European Office of Aerospace Research and Development, Air Force Office of Scientific Research, Air Force Research Laboratory, under Contract No. F61775-99-WE106. The work has been monitored by Dr. S. Walker.

The authors would also like to acknowledge an accurate and well-disposed assistance of Dr. Ch. Raffoul personally.

The authors would like to acknowledge helpful discussions of the present work with Prof. V. Bityurin and Dr. A. Klimov.

10. Applications.

(A) "The Contractor, Dr. Sergey Leonov, hereby declares that, to the best of its knowledge and belief, the technical data delivered herewith under Contract No. F61775-99-WE106 is complete, accurate, and complies with all requirements of the contract."

(B) "I, the Contractor, Dr. Sergey Leonov, certify that there were no subject inventions to declare as defined in FAR 52.227-13, during the performance of this contract."

(C) "Any opinions, findings and conclusions or recommendations expressed in this Report are those of the authors and do not necessarily reflect the views of any other persons and organizations."

DATE: ____ October, 12, 2000 ____

Name and Title of Authorized Official:

Dr. Sergey Leonov, Contractor

